

A New Guidance Method for a DeltaV and Re-entry Constrained Orbit Transfer Problem

by

Craig Joseph Van Beusekom

B.S. Astronautical Engineering, Mathematical Sciences
United States Air Force Academy, 2003

SUBMITTED TO THE DEPARTMENT OF AERONAUTICS AND ASTRONAUTICS
IN PARTIAL FULFILLMENT OF THE REQUIREMENTS FOR THE DEGREE OF

MASTER OF SCIENCE IN AERONAUTICS AND ASTRONAUTICS
AT THE
MASSACHUSETTS INSTITUTE OF TECHNOLOGY

JUNE 2005

© Craig Joseph Van Beusekom, 2005. All rights reserved.

The author hereby grants to MIT permission to reproduce and distribute publicly paper
and electronic copies of this thesis document in whole or in part.

Author:_____

Department of Aeronautics and Astronautics
April 27, 2005

Certified by:_____

Dr. Piero Miotto
Member of the Technical Staff, Charles Stark Draper Laboratory
Thesis Supervisor

Certified by:_____

Dr. Richard H. Battin
Senior Lecturer, Department of Aeronautics and Astronautics
Thesis Supervisor

Accepted by:_____

Jaime Peraire
Professor, Department of Aeronautics and Astronautics
Chair, Committee on Graduate Students

Report Documentation Page			Form Approved OMB No. 0704-0188		
Public reporting burden for the collection of information is estimated to average 1 hour per response, including the time for reviewing instructions, searching existing data sources, gathering and maintaining the data needed, and completing and reviewing the collection of information. Send comments regarding this burden estimate or any other aspect of this collection of information, including suggestions for reducing this burden, to Washington Headquarters Services, Directorate for Information Operations and Reports, 1215 Jefferson Davis Highway, Suite 1204, Arlington VA 22202-4302. Respondents should be aware that notwithstanding any other provision of law, no person shall be subject to a penalty for failing to comply with a collection of information if it does not display a currently valid OMB control number.					
1. REPORT DATE 00 JUN 2005		2. REPORT TYPE N/A		3. DATES COVERED -	
4. TITLE AND SUBTITLE A New Guidance Method for a DeltaV and Re-entry Constrained Orbit Transfer Problem				5a. CONTRACT NUMBER	
				5b. GRANT NUMBER	
				5c. PROGRAM ELEMENT NUMBER	
6. AUTHOR(S)				5d. PROJECT NUMBER	
				5e. TASK NUMBER	
				5f. WORK UNIT NUMBER	
7. PERFORMING ORGANIZATION NAME(S) AND ADDRESS(ES) Massachusetts Institute Of Technology				8. PERFORMING ORGANIZATION REPORT NUMBER	
9. SPONSORING/MONITORING AGENCY NAME(S) AND ADDRESS(ES)				10. SPONSOR/MONITOR'S ACRONYM(S)	
				11. SPONSOR/MONITOR'S REPORT NUMBER(S)	
12. DISTRIBUTION/AVAILABILITY STATEMENT Approved for public release, distribution unlimited					
13. SUPPLEMENTARY NOTES The original document contains color images.					
14. ABSTRACT					
15. SUBJECT TERMS					
16. SECURITY CLASSIFICATION OF:			17. LIMITATION OF ABSTRACT UU	18. NUMBER OF PAGES 156	19a. NAME OF RESPONSIBLE PERSON
a. REPORT unclassified	b. ABSTRACT unclassified	c. THIS PAGE unclassified			

[This page intentionally left blank.]

A New Guidance Method for a DeltaV and Re-entry Constrained Orbit Transfer Problem

by

Craig Joseph Van Beusekom

Submitted to the Department of Aeronautics and Astronautics
on April 27, 2005, in partial fulfillment of the
requirements for the degree of
Master of Science in Aeronautics and Astronautics

Abstract

This thesis proposes a spacecraft guidance system designed for a unique class of orbit transfer problems. It considers a vehicle that undertakes a maneuver with the objective of precisely flying through a point in space at a particular time. The spacecraft must automatically determine a transfer orbit that will take it from a circular, low-earth parking orbit to a velocity-unconstrained rendezvous with a Keplerian trajectory. A constraint exists that both the final transfer orbit and the ultimate paths of any additional stages must lead rapidly to atmospheric reentry, typically within one revolution. Constrained to a fixed ΔV resulting from a two stage thrust profile, the spacecraft must execute a burn maneuver that can effectively dissipate energy to place it on a transfer orbit with previously unknown velocity requirements. Finally, the guidance strategy should be robust to the uncertainties typically encountered in real spacecraft orbit transfer problems.

In order to meet these constraints, this thesis first develops new analytic analysis of the relationship between reentry, perigee, and ΔV . Next, a framework is developed for selecting a favorable transfer orbit while considering the various hard and soft constraints in the problem. Following transfer orbit selection, a plane of maneuver is calculated that maximizes likelihood of first stage reentry. Then traditional guidance strategies are adapted to the problem and hypothetical spacecraft design to produce a closed loop guidance solution. Results are presented that demonstrate the effectiveness of the new method.

Thesis Supervisor: Dr. Piero Miotto

Title: Member of the Technical Staff, Charles Stark Draper Laboratory

Thesis Supervisor: Dr. Richard H. Battin

Title: Senior Lecturer, Department of Aeronautics and Astronautics

[This page intentionally left blank.]

Acknowledgments

First, I would like thank Piero Miotto of Draper Laboratory for his constant involvement in the research that produced this thesis. I will also acknowledge Stan Shepperd of Draper Laboratory who provided critical insight into the problem and important suggestions from his deep background in spacecraft guidance. Laurent Duchesne and Len Wholey provided tremendous help in reviewing the thesis. Many others members of Draper Laboratory provided feedback and technical support along the way, including Jose Lopez, Frank Serna, Ed Bergmann, Mike Johnson, Dave Carter, Greg Andrews, Leena Singh, and Jeff Cipolioni.

I would also like to acknowledge the United States Air Force Academy Department of Astronautics and my previous instructors and mentors including Mike Hatfield, Joe Fulton, Ron Lisowski and others. I feel that the USAFA Astro Department gave me unparalleled preparation for the academic rigors of graduate study in spacecraft engineering and I hope that their effort is reflected in this thesis.

I am appreciative of the United States Air Force for allowing me the opportunity to spend two years studying at MIT as an active duty officer. My thanks also extend to the Charles Stark Draper Laboratory for its commitment to graduate education and for providing the means, both physically and financially, for my studies. To my fellow students at Draper, MIT, and Raymond Street, thanks for the many academic and non-academic discussions and experiences. I wish you all the best.

Publication of this thesis does not constitute approval by Draper or the sponsoring agency of the findings or conclusions contained herein. It is published for the exchange and stimulations of ideas.

As a member of the Air Force, I acknowledge that the views expressed in this thesis

are mine and do not reflect the official policy or position of the United States Air Force, the Department of Defense or the United States Government.

Craig J. Van Beusekom

Assignment

Draper Laboratory Report Number T-1511

In consideration for the research opportunity and permission to prepare my thesis by and at The Charles Stark Draper Laboratory, Inc., I hereby assign my copyright of the thesis to The Charles Stark Draper Laboratory, Inc., Cambridge, Massachusetts.

Craig J. Van Beusekom

Date

[This page intentionally left blank.]

Contents

1	Introduction	21
1.1	The New Problem	22
1.2	General Approach to Solving the Problem	24
1.3	Thesis Overview	26
2	Fundamental Astrodynamics	27
2.1	Orbital Geometry and the Two-Body Problem	27
2.1.1	Orbital Elements	28
2.1.2	Geometry of An Elliptical Orbit	30
2.1.3	Momentum and Energy Relationships	31
2.1.4	Orbit Propagation - Kepler's Problem	33
2.2	Orbit Transfer	34
2.2.1	Geometry of Orbital Boundary Value Problem	34
2.2.2	The Lambert Problem	35
2.3	Atmospheric Drag and Re-entry	37
2.4	Reference Frames	40
2.4.1	Earth-Centered Inertial Frame	40
2.4.2	Radial-Tangential-Normal Frame	41
2.4.3	Spacecraft Body Frame	41
2.5	Representations of Attitude	42
2.5.1	Direction Cosine Matrix	42
2.5.2	Euler Angles	43
2.5.3	Quaternions	43

2.5.4	Unit Vector Directions	44
3	Guidance and Control Techniques	45
3.1	General Energy Management Steering	45
3.1.1	GEM Steering: A Simple Example	46
3.1.2	Application of GEM to the Example Spacecraft	48
3.1.3	Closed-Loop Lambert GEM Guidance	49
3.2	Method of Linear Perturbations upon a Reference Trajectory	52
3.2.1	Estimating the Partial Derivatives of the Control Inputs	53
3.2.2	Solving for the New Control Variables	54
3.2.3	Implementation for Vehicle Guidance	56
4	Delta Velocity and Perigee Analysis	59
4.1	Relationship between Perigee and Velocity Changes	59
4.1.1	Expressing Velocity in the RTN Frame	60
4.1.2	General Result of Large Orbital Velocity Changes	61
4.1.3	Graphical Representation of Perigee and ΔV	63
4.2	Hyperbolic Locus of Constant Perigee	67
4.2.1	Mathematical Derivation of the Hyperbolic Locus of Constant Perigee	67
4.3	Exploring the Relationship between Perigee and ΔV	69
4.3.1	Three Dimensional Surfaces of Constant Perigee	69
4.4	Gradient of Perigee with Respect to Velocity	71
4.4.1	Partial Derivative of Semi-Major Axis with respect to ΔV	73
4.4.2	Partial Derivative of Eccentricity with respect to ΔV	74
4.4.3	Algorithm for Finding Gradient of Perigee	75
4.4.4	Application of Gradient of Perigee to the Mission	76
4.5	Concluding Thoughts on Perigee and ΔV	76
5	Trajectory Boundary Condition Selection	79
5.1	Exploring the Problem	79
5.1.1	Sample Set of Initial Conditions	80

5.1.2	Constraining Ignition Time	82
5.1.3	Constraining Rendezvous Time	83
5.2	Formulation into an Optimization Problem	84
5.2.1	Determining an Example Cost Function	85
5.2.2	TBCS Scenario 1: Coplanar Rendezvous, Opposite Direction of Travel	86
5.2.3	TBCS Scenario 2: Coplanar Rendezvous, Same Direction of Travel .	89
5.2.4	TBCS Scenario 3: Side Approach	91
5.3	General Observations on the TBCS Problem	94
5.3.1	Considerations on Relative Velocity	94
5.3.2	Considerations on Rendezvous Time	95
5.3.3	Reentry Characteristics	95
5.3.4	Summary	95
6	A New Reference Guidance Solution	97
6.1	A New Look at the Orbit Transfer Geometry	98
6.1.1	Position Without Burn	98
6.2	Recasting the Problem in the RPV Frame	99
6.2.1	Using GEM to Solve a Field-Free Problem	100
6.2.2	Using a GEM-CR Table to find $\Delta\theta$	104
6.3	Relating the RPV Frame back to the ECI Frame	107
6.3.1	Minimizing First Stage Perigee	107
6.3.2	Algorithm for the Reference Guidance Solution	108
6.3.3	Implementation using GEM-ARC	109
6.3.4	The Major Assumption	109
6.4	A Modification to d to Improve Performance	111
6.5	Justification for the Reference Guidance Solution	113
7	Application of Linear Perturbation Methods	115
7.1	Introducing Control Variables on the GEM Maneuver	115
7.1.1	Perturbations on Unit Vector Direction	116
7.1.2	Perturbation on the GEM Maneuver Assumptions	117

7.1.3	Updating the K Vector	119
7.1.4	Perturbations on the Time Line	120
7.2	Updating the Reference Guidance Solution	120
7.2.1	Control Input Vector	121
7.2.2	The Reference Update Algorithm	122
7.3	Closed Loop Guidance	123
7.3.1	Control Input Vector	123
7.3.2	Closed Loop Guidance Algorithm	123
8	Results	125
8.1	Performance of the Closed Loop Guidance Algorithm	126
8.1.1	Scenario 1	127
8.1.2	Scenario 3	131
8.2	Recommended Follow-on Analysis	134
9	Conclusion	135
9.1	Key Developments, Observations and Results	136
9.1.1	Analysis of Relationship between Perigee and ΔV	136
9.1.2	Impact of Initial Conditions on Possible Transfers	136
9.1.3	Framework for Selecting an Optimal Transfer	137
9.1.4	A New Reference Guidance Solution Technique	137
9.1.5	Substantial Improvements in Baseline Accuracy	137
9.2	Recommendations for Future Work	138
9.2.1	Examining the Effects of Uncertainties on Accuracy	138
9.2.2	Relating ΔV to Re-entry Time	138
9.2.3	Refining the TBCS Optimization Technique	139
A	Properties of the Example Spacecraft	141
B	Details of the Numerical Examples	143
B.1	TBCS	143
B.1.1	TBCS Initial Conditions	143

B.1.2	TBCS Cost Function	144
B.1.3	Intermediate Numbers for TBCS Scenario 1	146
B.2	Reference Guidance Solution	147
B.2.1	Scenario 1 Intermediate Numbers	148
B.2.2	Scenario 2 Intermediate Numbers	149
B.2.3	Scenario 3 Intermediate Numbers	151

[This page intentionally left blank.]

List of Figures

1-1	Sample Mission Trajectory	23
1-2	GN&C Components of the Problem	24
2-1	Conic Sections [6]	28
2-2	Geometry of Elliptical Orbits [6]	29
2-3	Classical Orbital Elements [6]	31
2-4	Altitudes in Elliptic Orbits [6]	32
2-5	Graphical Depiction of Eccentric Anomaly [2]	33
2-6	Geometry of Orbital Boundary Value Problem [2]	35
2-7	Sample Satellite Lifetimes from a 700 km Circular Orbit [9]	38
2-8	Estimate of Circular Orbit Satellite Lifetimes from Drag [9]	39
2-9	Earth Centered Inertial (ECI) Frame [6]	41
2-10	Radial-Tangential-Normal (RTN) Frame	42
3-1	Basic General Energy Management	46
3-2	GEM Steering along the Arc of a Circle	47
3-3	GEM Steering for Example Spacecraft with Constant Attitude Rates . . .	49
3-4	Comparison of GEM-Arc and GEM-CR for the Example Spacecraft	50
4-1	Graphical Results of Large Changes in Orbital Velocity	62
4-2	Contours of Perigee Altitude For R-T Components of $\Delta \mathbf{v}$	64
4-3	Contours of Perigee Altitude For T-N Components of $\Delta \mathbf{v}$	65
4-4	Perigee and R-T Components of $\Delta \mathbf{v}$, Example Spacecraft	65

4-5	Perigee and R-T Components of $\Delta \mathbf{v}$, Example Spacecraft and GEM Ma- neuver	66
4-6	Hyperbolic Loci of Constant Perigee	70
4-7	Surface of Constant Perigee	71
4-8	Three dimensional Surface of Constant Perigee	72
4-9	Gradient Field of Perigee With Respect to $\Delta \mathbf{v}$	77
5-1	Exploring TBCS, Orbital Side View	80
5-2	Exploring TBCS, ΔV and Perigee Contour Plot	81
5-3	Exploring TBCS, Magnitude of ΔV for Fixed Ignition Time	83
5-4	Exploring TBCS, Magnitude of ΔV for Fixed Rendezvous Time	84
5-5	TBCS Scenario 1, Transfer Orbit Side View	87
5-6	TBCS Scenario 1, Transfer Orbit Global View	87
5-7	TBCS Scenario 1, Optimized Transfer and ΔV and Perigee Contour Plot .	88
5-8	TBCS Scenario 2, Transfer Orbit Side View	89
5-9	TBCS Scenario 2, Transfer Orbit Global View	90
5-10	TBCS Scenario 2, Optimized Transfer and ΔV and Perigee Contour Plot .	91
5-11	TBCS Scenario 3, Transfer Orbit From Behind	92
5-12	TBCS Scenario 3, Transfer Orbit Polar View	92
5-13	TBCS Scenario 3, Transfer Orbit Global View	93
6-1	Depiction of Parking Orbit Relative to Rendezvous Point	98
6-2	Angular Rate and Angles for GEM-CR Maneuver with $\Delta\theta = 90^\circ$	101
6-3	Position and Velocity for GEM-CR Maneuver with $\Delta\theta = 90^\circ$	102
6-4	Position during GEM-CR Maneuver and 120 sec Coast	103
6-5	Position and Velocity, GEM-CR Maneuver and Coast in the RPV Frame .	105
6-6	Accuracy of the Reference Trajectory, Scenario 1	110
7-1	Theta in the GEM-CR Reference Maneuver	117
7-2	Theta in the GEM-ARC Reference Maneuver	118
7-3	Understanding the \mathbf{k} Update Process	119

8-1	Global View of the Closed Loop Simulation Trajectories, Scenario 1	128
8-2	View of the Closed Loop Simulation Trajectories, Scenario 1	129
8-3	Close-In View of the Closed Loop Simulation Transfer, Scenario 1	130
8-4	Alternate Plane of Maneuver, Scenario 1	132
8-5	View of the Closed Loop Simulation Trajectories, Scenario 3	133
8-6	View of the Closed Loop Simulation Trajectories, Scenario 3	133
8-7	View of the Closed Loop Simulation Trajectories, Scenario 3	134
A-1	Mass, Thrust, and Acceleration for Example Spacecraft	142

[This page intentionally left blank.]

List of Tables

4.1	Numerical Results of Large Changes in Orbital Velocity	63
5.1	Exploring TBCS, Bounds of Properties for 3218 Transfer Orbits	82
5.2	TBCS Scenario 1, Optimized Transfer Orbit Properties	87
5.3	TBCS Scenario 2, Optimized Transfer Orbit Properties	90
5.4	TBCS Scenario 3, Optimized Transfer Orbit Properties	93
5.5	Impact of Initial Conditions and TBCS on Selected Transfer Properties . .	96
6.1	Performance Comparison for the Two Definitions of \mathbf{d}	112
8.1	Comparison of Simulation Parameters	126
8.2	Comparison of Accuracy for Various Scenarios	126
8.3	Comparison of Re-entry Times for Various Scenarios	127
A.1	Example Spacecraft Characteristics	141

[This page intentionally left blank.]

Chapter 1

Introduction

Since the earliest launch of artificial satellites into orbit around the earth, engineers of spacefaring nations have encountered a variety of problems relating to the transfer of a space vehicle from one trajectory to another. These problems, most generally referred to as orbit transfer problems, have required Guidance, Navigation, and Control (GN&C) engineers to develop algorithms tailored to each unique space mission and specific set of vehicle hardware. Time and again, engineers have been able to successfully respond to mission requirements and in the process have developed a variety of algorithmic tools to address a variety of specific problems.

One class of orbit transfer problems addressed for nearly every space mission is orbit insertion. In these problems, the spacecraft must efficiently employ its actuators to move from an initial parking orbit to a final orbit where it was designed to execute its mission. These final orbits can be termed *Keplerian trajectories*, since the relationship between the positions, velocity, and time for these paths was first determined by Johannes Kepler in the year 1619. Rendezvous is a similar class of problem. Instead of a final constraint being the path of an imaginary object, the Keplerian trajectory is actually occupied by another spacecraft. Many highly visible rendezvous missions have been successful and include Gemini and Apollo as well as every Space Shuttle and Soyuz mission to service the International Space Station.

These vehicles employ a large variety of sensors and actuators to complete each individual mission. One class of important actuators are the thrusters used to impart changes in

velocity. Most space vehicles, including the Shuttle and most launch vehicle upper stage delivery systems, use liquid propellant engines. These liquid engines offer the GN&C engineers a relatively large degree of control, since the thrust ultimately responsible for changing the trajectory can usually be adjusted and toggled on and off.

A comparatively small number of space vehicles employ solid rocket engines, a consequence of the relative lack of options that solid rocket engines provide to engineers. Once a solid rocket is ignited, the thrust cannot be controlled precisely or stopped. Rather, it will continue to deliver its thrust based on the predetermined thrust profile and any environmental variables that impact this thrust profile. In fact, solid rocket use has typically been limited to apogee kick stage motors used for geostationary orbit insertion or similar planetary insertion missions. The precise value of ΔV that is required can be determined years before launch and the hardware components can be designed to meet that very specific requirement.

1.1 The New Problem

This thesis considers a problem very much related to rendezvous and orbit insertion, but one with enough differences in both trajectory and vehicle constraints to warrant a new approach. In this problem, a spacecraft has been placed in a low-altitude, circular parking orbit around the earth. At some point in the future and at very short notice, it must execute a maneuver that will place it on a trajectory to rendezvous with a point on a simulated Keplerian trajectory. Typically, a rendezvous mission constrains the final boundary value of the transfer to a given set of positions, velocities, and times corresponding to a final orbit. In this problem, the final velocity of the transfer remains unconstrained and the final boundary value is instead constrained to a set of positions and times corresponding to a Keplerian trajectory. In simple language, the vehicle must fly through a position at a certain time, the pair being one of a set of points in space and time.

The second key aspect of this problem is the unusual coupling of a fixed ΔV capability with a previously unknown ΔV requirement. The spacecraft is constrained to hardware consisting of two hypothetical solid rocket stages, the details of which are given in Ap-

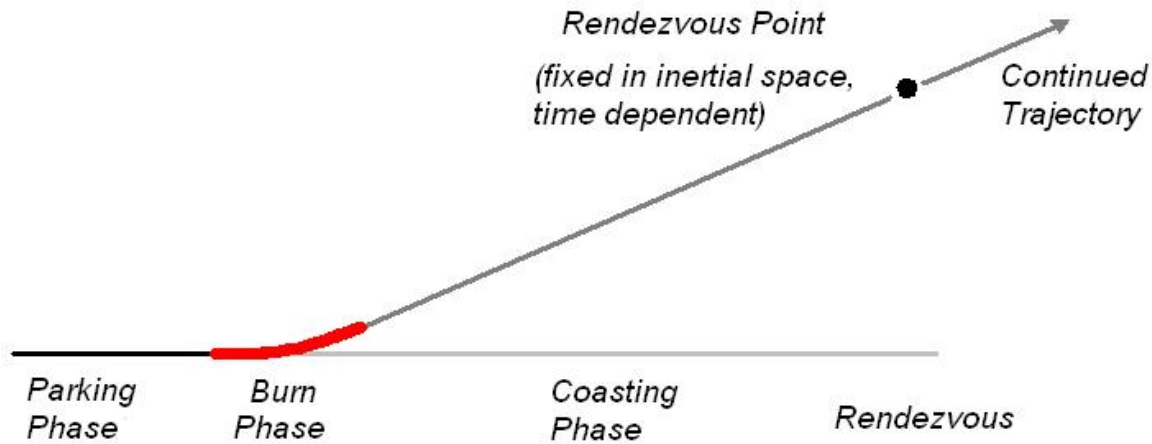


Figure 1-1: Sample Mission Trajectory

pendix A. The solid rocket engines are the cause of the fixed ΔV capability and thrust profile. This makes the problem more complex since the ΔV required remains unknown until after the design and launch of the spacecraft, contrasting with the solid apogee kick stage problem, where the required ΔV is known in the earliest stages of design. Since the required ΔV may be less than the capability, there is a risk of overshooting the intended point of rendezvous unless a method of reducing the effective amount of ΔV is developed and employed.

The third key constraint for this problem is one that is placed on the trajectory. It is presumed that the mission has requirements that all stages of the vehicle must re-enter the atmosphere in a specific amount of time. The large velocity changes available from the hardware can easily result in orbit transfers that will cause the space vehicle to remain in earth orbit for thousands of years before re-entry. Just as easily, orbit transfers can be designed that will cause atmospheric re-entry in a matter of hours at most. Few people would disagree that it is unwise to endanger generations of future human space exploration with space debris. This is particularly the case when it is possible to design the guidance law to cause immediate re-entry with no less effectiveness in completing the orbit transfer mission. The specific guidance solution developed in this thesis uses the

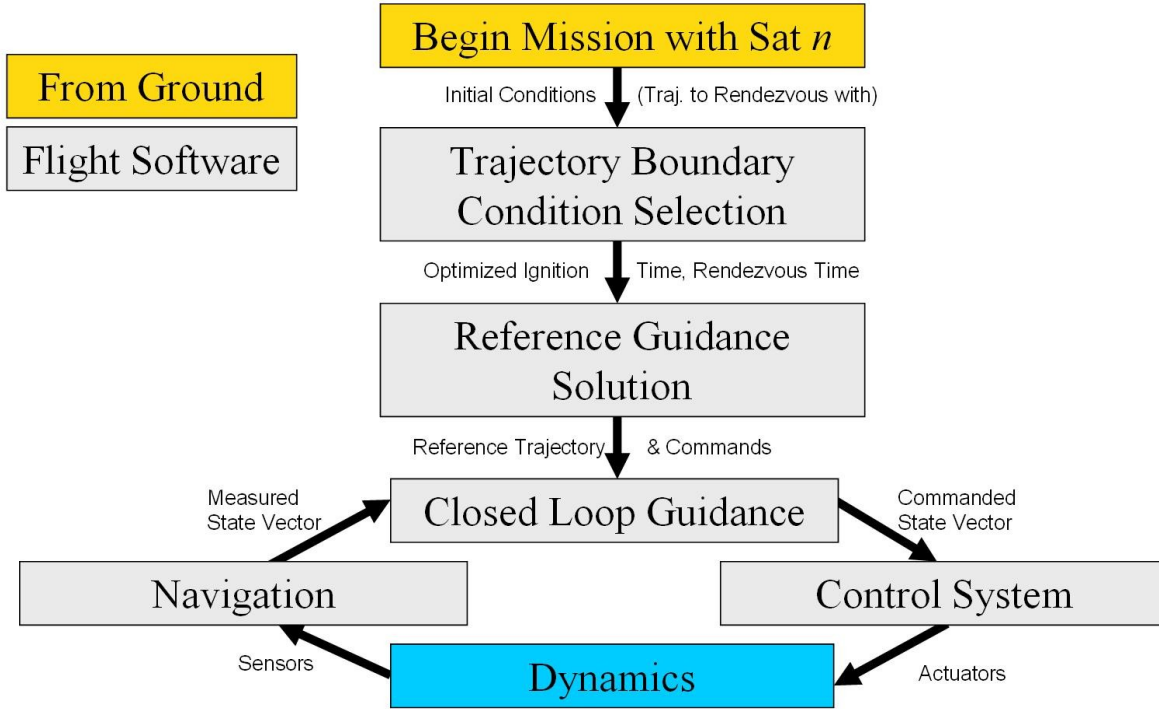


Figure 1-2: GN&C Components of the Problem

constraint of atmospheric re-entry within one revolution and this essentially flows down to a constraint on the perigee of the transfer orbit. In the event that an actual mission has less severe time constraints on re-entry, adjustments to the guidance laws are considered as well.

1.2 General Approach to Solving the Problem

In preparation to solve this overall GN&C problem, it will first be broken into distinct segments that might correspond to distinct algorithmic components of GN&C flight code. Figure 1-2 highlights the flow of information between the various components. First, it is assumed the spacecraft's ground station would issue a command to begin a rendezvous sequence with a given Keplerian trajectory, which would be uploaded to the spacecraft flight computer.

After receiving the command to commence the mission, the spacecraft is responsible for determining a transfer orbit that would take it from its parking orbit to a point

on the Keplerian trajectory. The specific transfer orbit should be selected based on its characteristics, such as one that meets the re-entry constraint and has a high probability of success. The problem of determining an ignition time and rendezvous time is referred to the *Trajectory Boundary Condition Selection* (TBCS) problem.

Once the baseline transfer orbit has been determined by TBCS, the next problem is to determine a reference trajectory and set of reference commands that will deliver the spacecraft to the rendezvous point at the rendezvous time. The final step is the closed loop guidance portion. Continually throughout the maneuver at a specified guidance update rate, the spacecraft will propagate forward its state vector with the reference control inputs in order to determine if it is still on track to reach the rendezvous point. The spacecraft will typically determine that small modifications to the reference control variables will change the trajectory enough to eliminate the expected miss distance, and thus updates the reference commands.

The control system problem is concerned with transforming the desired state vector into signals that can be interpreted by control system actuators. The navigation system uses signals corresponding to physical measurements by sensors to reconstruct the state vector of the vehicle. Design of the control system and navigation system are heavily dependent on the particular hardware. Since this thesis only considers a hypothetical vehicle, the emphasis is on the more abstract guidance system approach which could be adapted to a relatively broad array of vehicle actuators and sensors. Consequently, the specific design of navigation system and control system for a spacecraft are not included in this thesis. However, the development of the guidance system must make reasonable assumptions about the capability of control systems. In this case, it is assumed that the spacecraft is maneuverable and is able to employ agile thrust vector control to change the thrust direction during the course of the burns as well as thrusters that allow for reorientation of the vehicle prior to ignition of the engines.

1.3 Thesis Overview

Chapter 2 reviews several fundamental concepts relating to orbital mechanics, the orbital boundary value problem, atmospheric re-entry, coordinate frames, and representations of attitude. Astrodynamics relationships that are used in derivations are explained.

Chapter 3 introduces guidance techniques that will form the backbone for the solution. The General energy management technique enables a vehicle to impart velocity along a curve such that net ΔV can be less than the ΔV actually used. It is an important technique that can add degrees of freedom to the guidance system. The method of linear perturbations upon a reference trajectory is a proven technique of closed loop guidance for vehicles with dynamics that can be partially modeled.

Chapter 4 explores the interaction between reentry and ΔV that is uniquely important to the problem under consideration. In the process, a few key relationships are derived that will form key components of the future guidance algorithm.

Chapter 5 explores what is called Trajectory Boundary Condition Selection (TBCS). Given the parking orbit and Keplerian trajectories, this chapter transforms the selection of the transfer orbit into an optimization problem while considering the hard and soft constraints in this problem as well as other properties that could be of consideration in similar missions.

Chapter 6 details the development of the guidance algorithm. Lambert GEM Steering is introduced. Then a new method of finding a reference trajectory is outlined. Finally, Chapter 7 outlines the specific application of the method of linear perturbations upon a reference trajectory to this problem.

Chapter 8 presents several graphical and numerical results from algorithms developed in the preceding chapters. Chapter 9 summarizes the general conclusions that can be drawn from the results and suggests potential avenues for future research.

Chapter 2

Fundamental Astrodynamics

A basic grasp of orbital motion is a prerequisite to understanding many of the concepts contained in this thesis. Nonetheless, this chapter reviews several fundamental relationships and ideas and defines quantities which will be used in derivations and explanations in the following chapters.

2.1 Orbital Geometry and the Two-Body Problem

Newton's law of universal gravitation is the primary cause of orbital motion, and is shown in Equation 2.1. If it assumed that Newton's law of gravitation acts between two point masses and the smaller mass is negligible compared to the larger mass, such as a spacecraft in motion around the earth, the resulting equation of motion is given in Equation 2.2. The vector \mathbf{r} is the position of the smaller mass with respect to an inertially-fixed coordinate system centered at the larger mass. This is known as the equation of two-body motion.

$$F_g = \frac{Gm_1m_2}{r^2} \quad (2.1)$$

$$\ddot{\mathbf{r}} + \frac{\mu}{r^3}\mathbf{r} = 0 \quad (2.2)$$

where $\mu = G_{earth}m_{earth} = 398600.5 \text{ km}^3/\text{sec}^2$

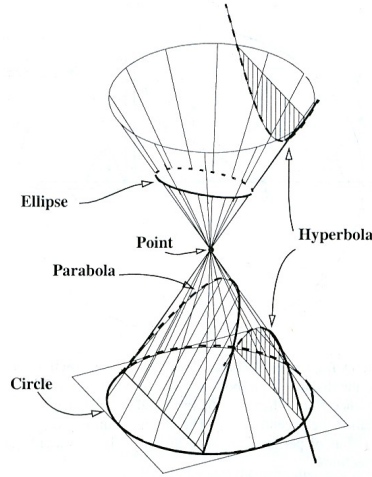


Figure 2-1: Conic Sections [6]

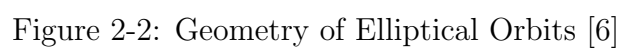
In addition to assuming that the two bodies are point masses, the two body equation of motion disregards disturbing forces such as the the gravitational pull of the sun and moon, atmospheric drag at low altitudes, and higher order gravitational effects such as J_2 . Depending on initial conditions of \mathbf{r} and $\dot{\mathbf{r}}$, Equation 2.2 can lead to four different types of orbits: circular, elliptic, parabolic, and hyperbolic. These four shapes are all known as conic sections. Figure 2-1 shows how different conics result from the intersection of a plane with a cone.

2.1.1 Orbital Elements

Defining the present and future location of an object moving under the influence of another object requires six independent quantities. A position vector $\mathbf{r} \in \mathbb{R}^3$ and velocity vector $\mathbf{v} \in \mathbb{R}^3$ is one such representation. However, these quantities alone tend to defy intuition for the shape of an orbit. For centuries, astronomers have used six classical orbital elements which describe the size, shape, and orientation of orbits, as well as position within those orbits.

Semi-major axis a is a physical distance used to defines the size of the orbit. It is also directly related to the period of the orbit. For an ellipse, a is one-half of the longer axis as illustrated in Figure 2-2.

Eccentricity e is a non-dimensional quantity which measures the particular shape of



the orbit. A circular orbit has an eccentricity of zero. An elliptical orbit has an eccentricity in the range $(0, 1)$. Parabolic orbits have eccentricities of one while hyperbolic orbits have eccentricities in the range $(1, \infty)$. Mathematically, eccentricity is the ratio of the distance between the foci ($2c$) and the major axis of the ellipse ($2a$), as depicted in Figure 2-2 and stated in Equation 2.3.

$$e = \frac{2c}{2a} \quad (2.3)$$

Semi-major axis and eccentricity are often combined in a quantity known as the parameter p of an orbit, which appears often in equations describing orbital motion. The parameter is also depicted in Figure 2-2 as the radius at the points ± 90 degrees from the pericenter, which is the point of minimum radius between the two bodies.

$$p = a(1 - e^2) \quad (2.4)$$

The next three orbital elements measure the orientation of an orbit. Inclination (i) is an angle that describes the tilt of an orbit with respect to the equatorial plane. For a non-zero inclination, the longitude or right ascension of the ascending node (Ω) is the angle measured from the primary (x) axis of the equatorial plane to ascending node. The ascending node \hat{n} is defined as the point where the satellite crosses from the southern hemisphere to the northern hemisphere, as depicted in Figure 2-3. Argument of pericenter (ω) is the angle between the ascending node and pericenter. Circular orbits and those which lie entirely in the equatorial plane require alternate orbital elements in place of Ω and ω .

The final classical orbital element describes where in an orbit a satellite is currently located. True anomaly, ν , is the angular measurement from pericenter to the current position of the satellite. Figure 2-3 depicts the four angular classical orbital elements.

2.1.2 Geometry of An Elliptical Orbit

This work is concerned primarily with elliptical orbits. Two additional quantities will become important. For an earth-centered orbit, perigee and apogee define the point in

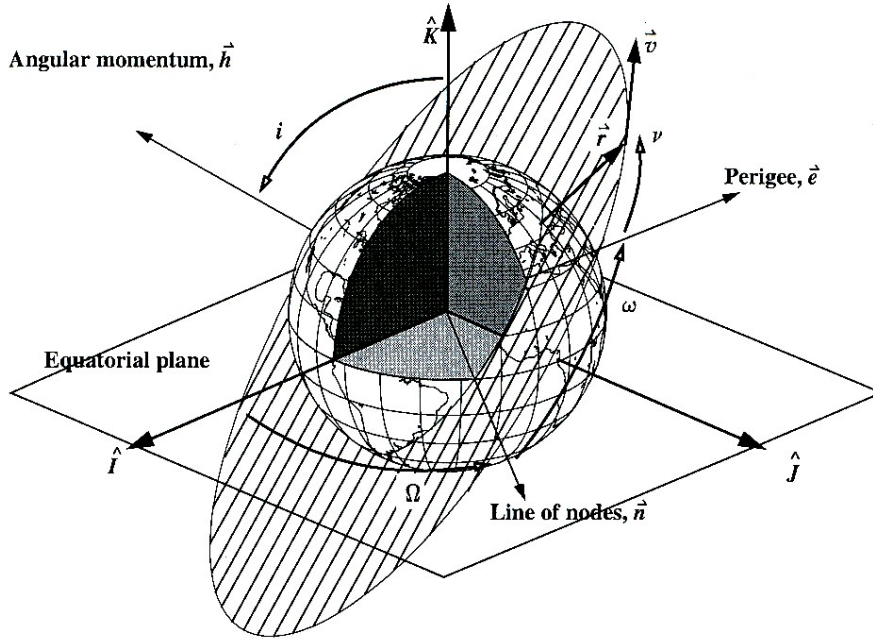


Figure 2-3: Classical Orbital Elements [6]

each orbit where the radius of the satellite is smallest and largest, respectively.

$$r_p = a(1 - e) \quad (2.5)$$

$$r_a = a(1 + e) \quad (2.6)$$

Note that the radius of perigee r_p is different than the perigee altitude h_p by the amount of the earth's radius. Figure 2-4 clarifies these distinctions.

2.1.3 Momentum and Energy Relationships

There are a few additional quantities that are critical in the relationships described in the following chapters. The angular momentum of an orbit \mathbf{h} is an invariant vector quantity normal to the satellite's plane of motion. Its magnitude h establishes a key relationship between μ and p in Equation 2.8.

$$\mathbf{h} = \mathbf{r} \times \mathbf{v} = \text{constant} \quad (2.7)$$

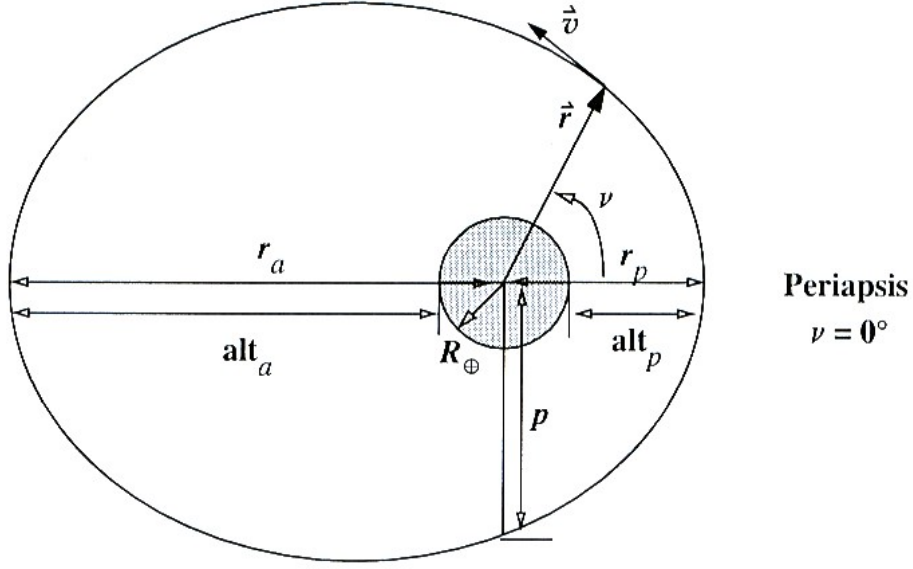


Figure 2-4: Altitudes in Elliptic Orbits [6]

$$p \equiv \frac{h^2}{\mu} \quad (2.8)$$

The eccentricity vector \mathbf{e} is a vector of magnitude e which points in the direction from the focus to the location of perigee. Equation 2.10 is used to determine the eccentricity vector with from vectors \mathbf{r} and \mathbf{v} from any point on the orbit.

$$\mathbf{e} = \|\mathbf{e}\| \quad (2.9)$$

$$\mu \mathbf{e} = \mathbf{v} \times (\mathbf{r} \times \mathbf{v}) - \frac{\mu}{r} \mathbf{r} \quad (2.10)$$

The energy integral is known as the vis-viva integral. At any point in an orbit, it relates the scalar radius from the focus r to the scalar velocity v and semi-major axis a of the orbit, as shown in Equation 2.11.

$$v^2 = \mu \left(\frac{2}{r} - \frac{1}{a} \right) \quad (2.11)$$

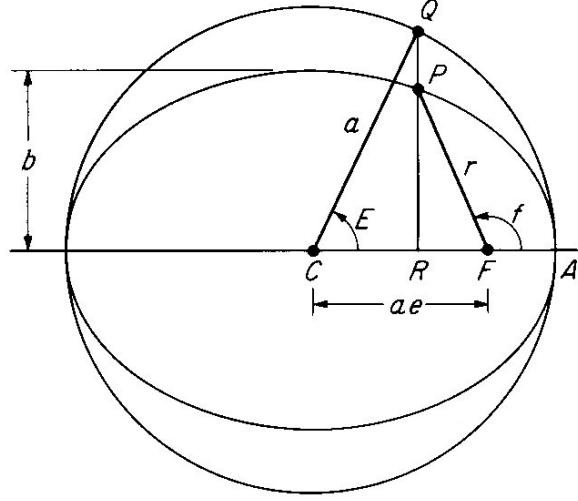


Figure 2-5: Graphical Depiction of Eccentric Anomaly [2]

2.1.4 Orbit Propagation - Kepler's Problem

An important problem in astrodynamics is the propagation of a satellite position and velocity forward in time. In two body motion, all of the classical orbital elements are invariant with the exception of true anomaly ν . Thus, orbit propagation generally involves finding a , e , i , Ω , and ω from the initial position and velocity \mathbf{r} and \mathbf{v} . References [4] and [6] cover this in detail. Then using the propagation time, $\Delta t = (t_2 - t_1)$, the value of ν is found.

This is known as Kepler's problem. There is not a direct equation relating ν and Δt . Rather, for propagating eccentric orbits, two auxiliary angles called eccentric anomaly (E) and mean anomaly (M) are required. Eccentric anomaly has a geometric representation as the angle from pericenter passage to a satellite's position on an auxiliary circle measured from the center of the ellipse. Figure 2-5 depicts the geometric interpretation of E while Equation 2.12 is the mathematical relationship between true and eccentric anomaly.

$$\tan\left(\frac{1}{2}\nu\right) = \sqrt{\frac{1+e}{1-e}} \tan\left(\frac{1}{2}E\right) \quad (2.12)$$

Eccentric anomaly is related to mean anomaly by Equation 2.13, which is widely known as Kepler's equation. Equation 2.13 can be solved directly for M , but when finding E from M , it requires an iterative method for a solution, typically with successive substitutions

[6].

$$M = E - e \sin E \quad (2.13)$$

$$n = \sqrt{\frac{\mu}{a^3}} \quad (2.14)$$

$$M_2 - M_1 = n(t_2 - t_1) \quad (2.15)$$

Mean anomaly has no geometric representation, but is linearly related to the passage of time by a quantity called mean motion, n . Mean motion is constant for a given a , as shown in Equation 2.14. In Equation 2.15, the change in mean anomaly is simply the product of mean motion and time.

2.2 Orbit Transfer

The background presented in this chapter has been mostly concerned with understanding the motion of satellites traveling on the invariant orbit paths of two body motion. Another important class of astrodynamics deals with finding orbits that meet certain position and time constraints.

2.2.1 Geometry of Orbital Boundary Value Problem

Figure 2-6 shows the basic geometry for the problem of finding a transfer orbit connecting points P_1 and P_2 . Position vectors \mathbf{r}_1 and \mathbf{r}_2 describe the respective positions measured from the center of the large body located at focus F . The velocities \mathbf{v}_1 and \mathbf{v}_2 are the respective velocity vectors. Finally, the transfer angle θ is the angle between the points measured from the central body.

The general boundary values for a transfer orbit are \mathbf{r}_1 , \mathbf{r}_2 , \mathbf{v}_1 , \mathbf{v}_2 , and a given transfer time $\Delta t = t_2 - t_1$. A transfer orbit defined by these values would satisfy the boundary conditions if two-body (Kepler) propagation of the state $(\mathbf{r}_1, \mathbf{v}_1)$ for Δt results in a final

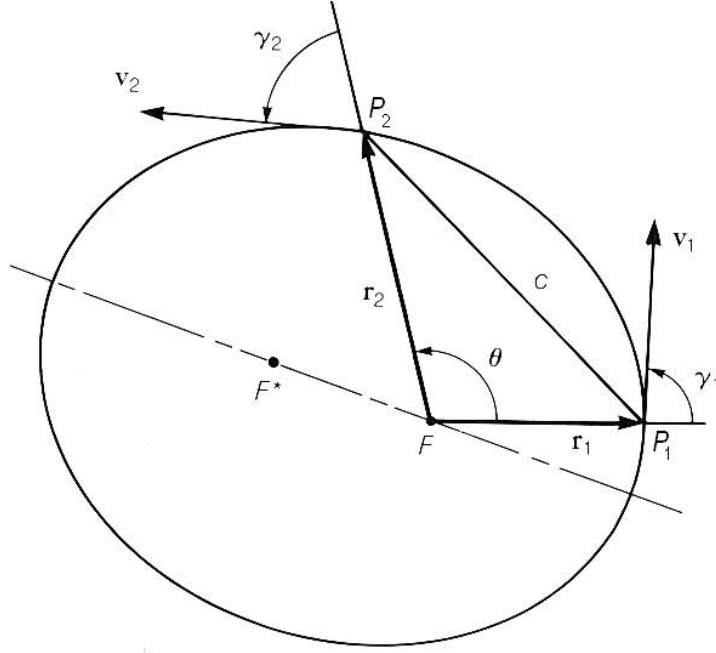


Figure 2-6: Geometry of Orbital Boundary Value Problem [2]

state $(\mathbf{r}_2, \mathbf{v}_2)$. A boundary value problem is generally concerned with fixing a certain number of these boundaries and solving for the others.

$$\mathbf{c} = \mathbf{r}_2 - \mathbf{r}_1 \quad (2.16)$$

The vector \mathbf{c} is known as the chord of the orbit transfer problem as defined in Equation 2.16. The magnitude of the chord, c , is an important quantity used in the solution.

2.2.2 The Lambert Problem

The *Lambert Problem* is a subset of the general orbital boundary value problem where two position vectors and the transfer time are fixed and the boundary velocities must be solved for. It was first characterized by Johannes Lambert in 1761. Lambert discovered a relationship between the geometry of the orbit transfer and the transfer time. The original form is shown in Equation 2.17.

$$\sqrt{\mu} (t_2 - t_1) = F(a, r_1 + r_2, c) \quad (2.17)$$

Gauss discovered in 1809 the full solution that eluded Lambert. In 1987, Richard Battin of MIT published a solution improving upon Gauss's method by removing the singularity at $\theta = 180$ degrees and offering substantial improvements in convergence. The statement of the Lambert problem that is useful here is given in Equation 2.18. The actual algorithm has been omitted from this text but is widely available.

$$(\mathbf{v}_1, \mathbf{v}_2) = F(\mathbf{r}_1, \mathbf{r}_2, \Delta t, t_m) \quad (2.18)$$

For given position vectors \mathbf{r}_1 and \mathbf{r}_2 , and a given time of flight, there are two conjugate orbits connecting P_1 to P_2 . Those conjugate orbits will typically follow opposite paths around the earth. The binary transfer method term t_m is used to choose either the short way or the long way around the earth from P_1 to P_2 . In Figure 2-6, the short method is illustrated by the counterclockwise path from P_1 to P_2 while the long way (for a different transfer time) is illustrated by the clockwise path.

The velocities at the boundaries, \mathbf{v}_1 and \mathbf{v}_2 , define the transfer orbit and are useful in determining any required maneuvers to place the spacecraft on this new transfer orbit trajectory from an existing orbit. While the Lambert problem typically provides two possible paths from P_1 to P_2 , usually only one, if either, are feasible for a real spacecraft. Typically only one of the two possible \mathbf{v}_1 solutions is aligned sufficiently with the spacecraft's original velocity vector to make a velocity changing maneuver feasible. There is also an issue in that a Lambert routine may return a trajectory that intersects the surface of the earth on the way to P_2 .

It is important to note that all solutions of the Lambert problem are dependent on the assumption of two body mechanics. Vallado [6] offers a detailed algorithm for the Gauss, Battin, and universal variable solutions to the Lambert problem. Battin [2] is also an excellent resource for details on the derivation of his method.

The Lambert Problem and Required ΔV

Suppose a spacecraft has a particular position \mathbf{r}_1 and velocity $\mathbf{v}_{current}$ at t_1 and has the objective of reaching the point \mathbf{r}_2 at a future time t_2 . Then the Lambert boundary velocity

\mathbf{v}_1 from Equation 2.18 can be used with Equation 2.19 to find the instantaneous change in velocity $\Delta\mathbf{v}_{instantaneous}$ that will bring the spacecraft to \mathbf{r}_2 at t_2 . This is often referred to as the Lambert ΔV .

$$\Delta\mathbf{v}_{instantaneous} = \mathbf{v}_1 - \mathbf{v}_{current} \quad (2.19)$$

Note that in this document, $\Delta\mathbf{v}$ refers to a specific change in velocity that can be calculated, while ΔV refers to the general idea of velocity change (or integrated acceleration resulting from thrust).

2.3 Atmospheric Drag and Re-entry

Atmospheric drag is a disturbing force that is one of several perturbations that cause the path of satellites to vary slightly from that predicted by Equation 2.2, the two-body equation of motion. Ultimately, drag has a significant impact on re-entry characteristics.

The perturbation acceleration due to atmospheric drag acts in the direction opposite to the velocity vector and is given in Equation 2.20. The variations in atmospheric drag are primarily due to variations in the density of the atmosphere ρ . Atmospheric density varies substantially with the 11-year solar cycle and even varies from the daytime half to the nighttime half of the planet. This variation is particularly large for the altitudes between 500 and 800 km, where it may vary by an order of magnitude between solar minimums and solar maximums [9]. Atmospheric drag also depends on the ballistic coefficient BC of the satellite, shown in Equation 2.21, which depends on the mass m , cross-sectional area A , and coefficient of drag C_D .

$$\mathbf{a}_{drag} = \frac{-\rho C_D A v \mathbf{v}}{2m} = \frac{-1}{2} \frac{\rho v \mathbf{v}}{BC} \quad (2.20)$$

$$BC = \frac{m}{C_D A} \quad (2.21)$$

Because of the higher density atmosphere at lower altitudes, drag has the highest effect near the perigee of a satellite's orbit. Since it acts retro to the velocity vector, its effect is

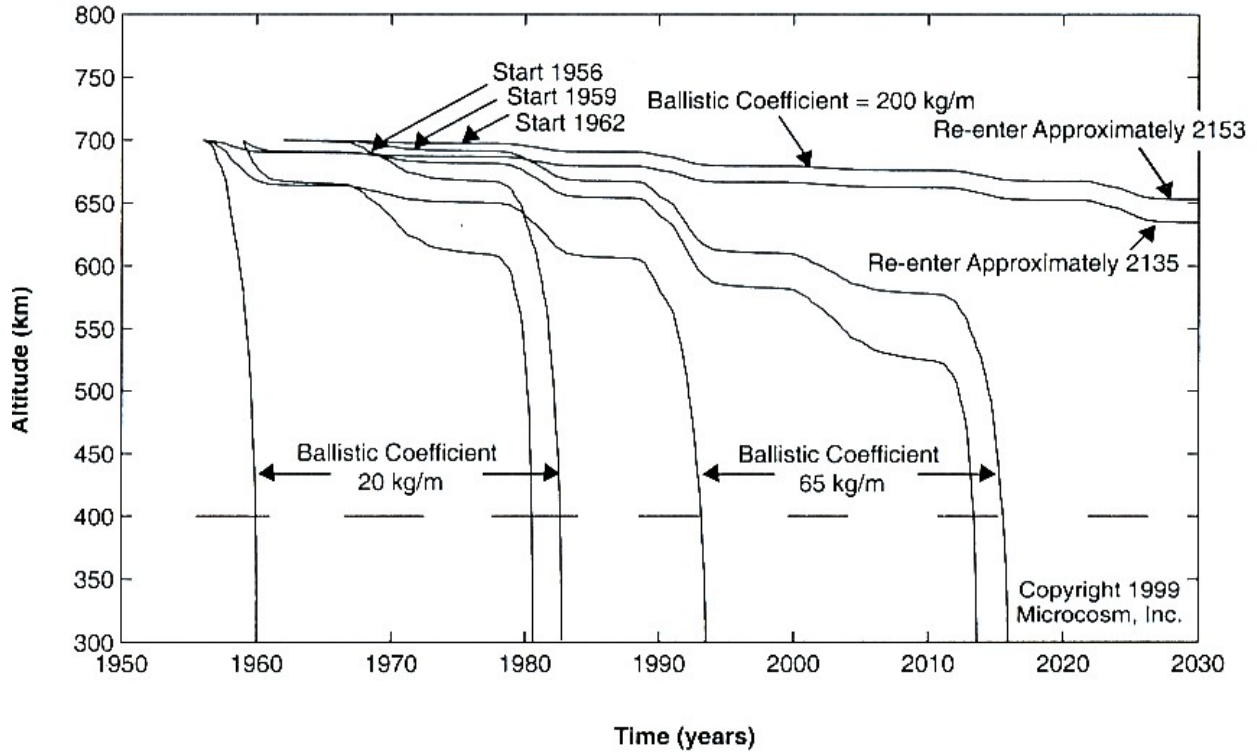


Figure 2-7: Sample Satellite Lifetimes from a 700 km Circular Orbit [9]

to reduce the velocity at perigee. For elliptical orbits, this causes r_p to stay constant while r_a continually decreases until $r_p = r_a$ and the orbit is circular. At that point, semi-major axis a continues to decrease until atmospheric drag reduces the velocity so much that re-entry becomes imminent. At some point, near an altitude of 100 km, the drag is so large that the spacecraft will reenter within one orbit.

Figures 2-7 and 2-8 are well-known illustrations that shed light on the impact of atmospheric drag on satellite lifetime. Figure 2-7 shows the changes in altitude for three different ballistic coefficients starting at three different times (corresponding to the 1956 beginning of the solar maximum, the 1959 end of the solar maximum, and the 1962 beginning of the solar minimum). This illustrates that depending on the ballistic coefficient and time of launch, the satellite could reenter from its 700 km orbit anywhere from five years to 190 years after orbit insetion.

Given a starting altitude and ballistic coefficient, Figure 2-8 shows the range of satellite lifetimes that may result. For instance, if a satellite with a ballistic coefficient of 65 kg/m^2

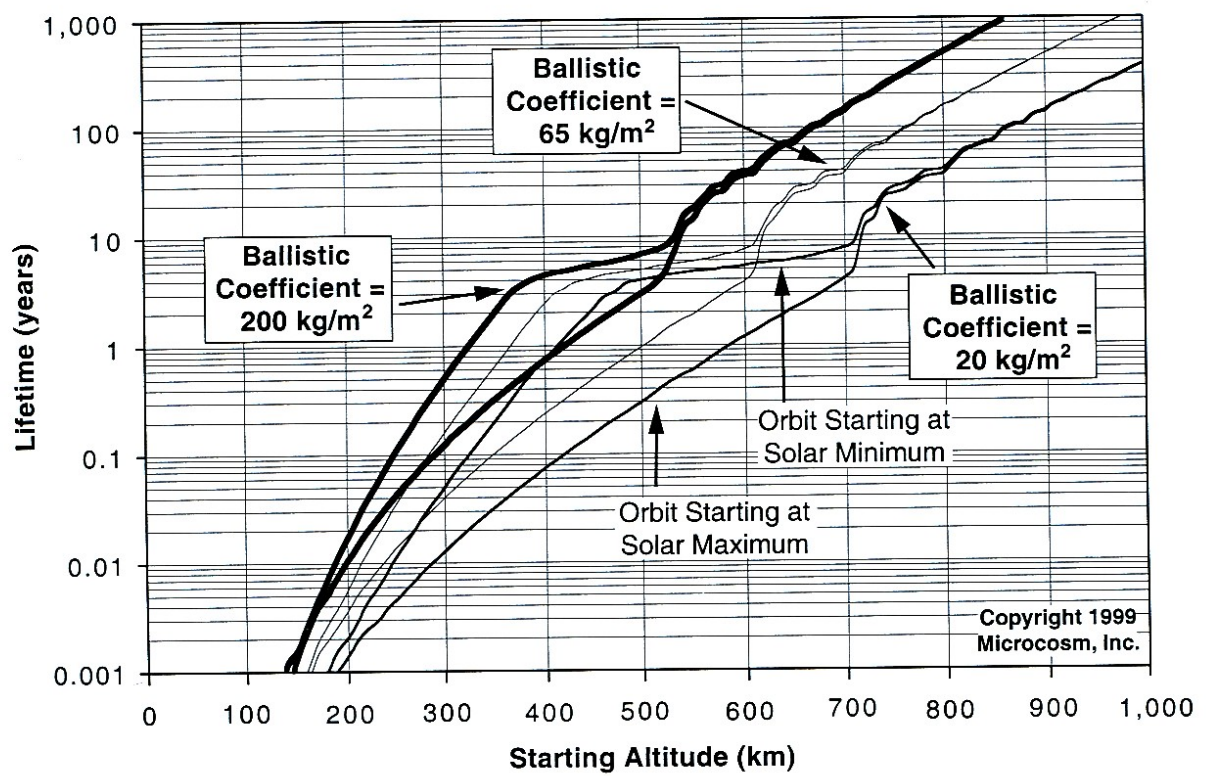


Figure 2-8: Estimate of Circular Orbit Satellite Lifetimes from Drag [9]

was placed at 500 km, it would remain there between one and five years. Reference [9] has more information on atmospheric drag.

2.4 Reference Frames

Until now, vector quantities have been considered without regard to reference frame. This section describes the orientation and purpose of various frames which will be critical to understanding formulations in the following chapters.

2.4.1 Earth-Centered Inertial Frame

Newton's equations are only valid in inertial space. In order to analyze the motion of a spacecraft, it is necessary to use an inertial reference frame, which is a stationary, non-rotating set of orthogonal axis vectors. For earth-orbiting satellites, this typically involves using the Earth-Centered Inertial (ECI) frame. The ECI frame has a first principal (x) axis in the direction of the astronomical first point of Aries (the direction to the sun at the vernal equinox), a fundamental plane defined by the earth's equatorial plane, and third principal axis defined by the earth's rotational axis (the North Pole). This is also often called the IJK frame, from the unit vectors typically used to describe its principal directions. Since the earth's spin axis (and thus equatorial plane) tends to wobble a bit, the ECI frame is typically tied to some epoch, such as January 1, 2000 [4].

Figure 2-9 shows the principal axes of the ECI frame. Note that the frame does not rotate with the earth but would require a rotation by an angle, global sidereal time (GST), into another coordinate system that is fixed to the earth's surface, such as the Earth-Centered Fixed (ECF) frame [6]. Since the origin of the ECI frame is at the center of the earth, and the earth revolves around the sun, the ECI is not truly inertial. However, this approximation is justified for the purpose of analyzing spacecraft motion around the earth.

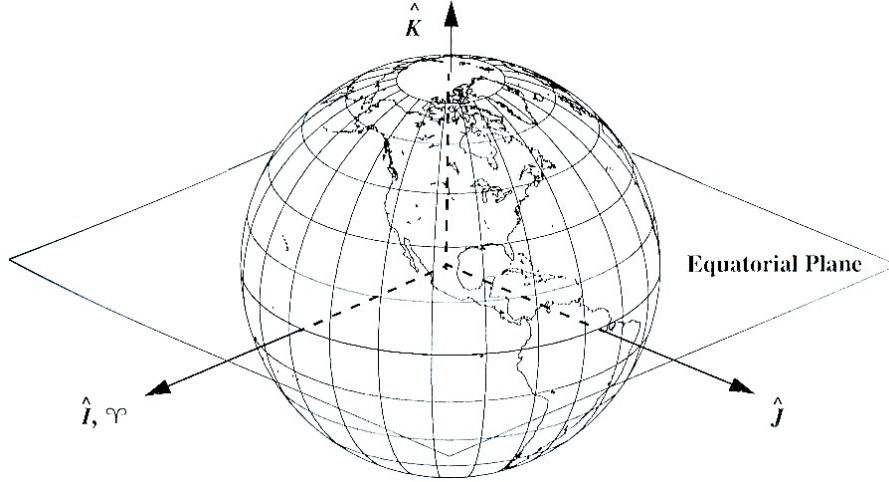


Figure 2-9: Earth Centered Inertial (ECI) Frame [6]

2.4.2 Radial-Tangential-Normal Frame

The Radial-Tangential-Normal frame is a local orbital frame. The origin is located at the spacecraft's center of mass. The origin is not fixed but rotates as the spacecraft travels around the earth. Thus, it is not an inertial frame. The primary axis is along the vector \mathbf{r} from the center of the earth toward the spacecraft. The fundamental plane is the orbit plane. Therefore, the second axis is in the direction of the local horizontal component of the velocity vector (or if the orbit is exactly circular, the velocity vector direction itself) and the third axis is parallel to the satellite's angular momentum vector \mathbf{h} . The transformation matrix from the RTN frame to the ECI frame is found in the next section, Equation 2.22.

2.4.3 Spacecraft Body Frame

The spacecraft body frame is a set of orthogonal vectors that are fixed to the body of the spacecraft. The various sensors and actuators of the spacecraft are typically defined with respect to the body frame.

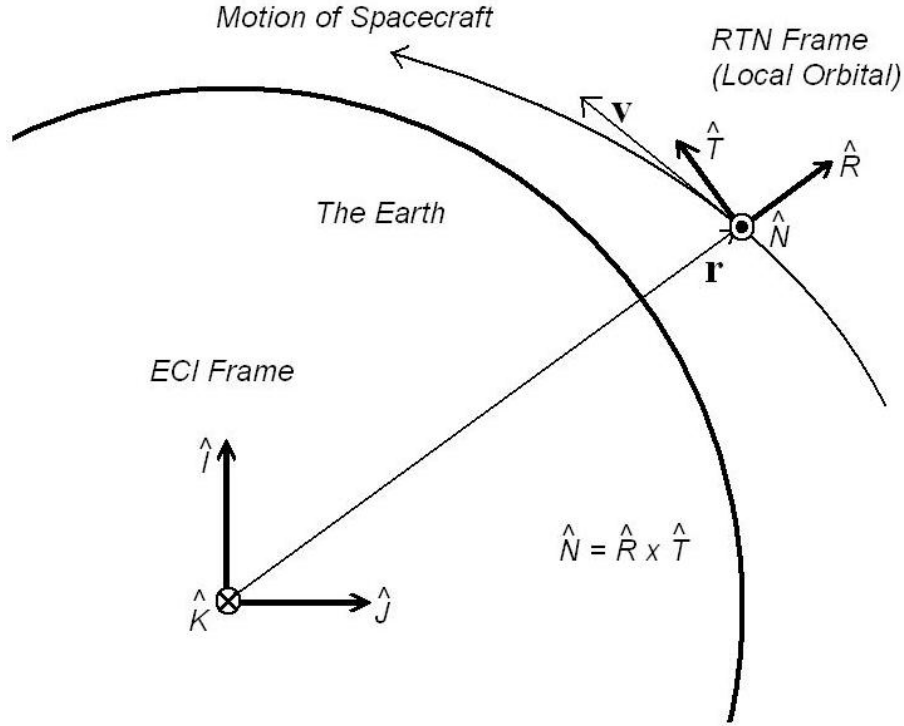


Figure 2-10: Radial-Tangential-Normal (RTN) Frame

2.5 Representations of Attitude

Attitude is a general term for any representation that relates one reference frame to another. Spacecraft attitude, in the form that it is most often referred to, usually means the Euler angles between the body frame and a local orbital reference frame, such as the RTN frame used here. A complete representation of attitude that relates one reference frame to another has three degrees of freedom.

2.5.1 Direction Cosine Matrix

A direction cosine matrix (DCM) is an orthonormal 3×3 matrix that is used to directly translate vectors from one coordinate frame to another. As in any representation of attitude, the DCM also has three degrees of freedom because while there are nine elements in the matrix, each of the three rows and each of the three columns is constrained to have magnitude one. The advantage of a direction cosine matrix (or transformation matrix) is that it can directly be used to transform vectors from one reference frame to another.

The matrix $\mathbf{T}_{ECI2RTN}$ is one such DCM that will transform any vector in the ECI frame into the RTN frame. Equation 2.23 demonstrates how to use $\mathbf{T}_{ECI2RTN}$ to transform a vector. Note that the superscript on a vector describes which frame it is written in.

$$\mathbf{T}_{ECI2RTN} = \left[\begin{array}{c|c|c} \frac{\mathbf{r}}{r} & \frac{(\mathbf{r} \times \mathbf{v}) \times \mathbf{r}}{\|(\mathbf{r} \times \mathbf{v}) \times \mathbf{r}\|} & \frac{\mathbf{r} \times \mathbf{v}}{\|\mathbf{r} \times \mathbf{v}\|} \end{array} \right] \quad (2.22)$$

$$\mathbf{v}^{RTN} = \mathbf{T}_{ECI2RTN} \cdot \mathbf{v}^{ECI} \quad (2.23)$$

2.5.2 Euler Angles

Euler angles are the classic and most intuitive method of attitude information. A set of Euler angles must be accompanied by a description of how they are defined. For example, a 2-1-3 transformation would correspond to a rotation of the original second axis by ϕ , followed by a rotation around the new first axis by θ , followed by a rotation of the new third axis by ψ . The classic orbital elements Ω , i , and ω , depicted in Figure 2-3, are actually a set of 3-1-3 Euler angles.

2.5.3 Quaternions

Quaternions, or Euler symmetric parameters, are a popular method of defining the attitude of a spacecraft. Euler determined that any transformation between two reference frames can be accomplished by a single rotation by an angle Θ around a unit vector $\hat{\mathbf{e}} \in \mathbb{R}^3$. The four components of \mathbf{q} are a representation of this rotation [9]. A quaternion vector has three degrees of freedom since the vector is constrained to have magnitude one.

$$\mathbf{q} = \begin{bmatrix} q_1 & q_2 & q_2 & q_4 \end{bmatrix}^T \in \mathbb{R}^4 \quad (2.24)$$

$$\|\mathbf{q}\| = \sqrt{q_1^2 + q_2^2 + q_3^2 + q_4^2} = 1 \quad (2.25)$$

Of the representations of attitude, quaternions are used most often in spacecraft flight computers because they do not suffer from a singularity when propagated forward in time

and have computational advantages over Euler angles. However, a disadvantage is that quaternions are very non-intuitive to people and are usually translated back into Euler angles for engineering analysis.

2.5.4 Unit Vector Directions

Because of the nature of the example spacecraft, this research often deals with unit vector pointing directions. Often, a rocket engine's thrust may simply need to be pointed in a certain direction. The rotation around that direction is irrelevant. If a vehicle is commanded to point in a unit vector direction, the rotation angle around that vector remains unconstrained. A unit vector direction has only two degrees of freedom.

Chapter 3

Guidance and Control Techniques

This chapter introduces two key techniques for guidance and control that will be used in later chapters to develop a guidance solution for the example spacecraft. The first technique, GEM Steering, is an effective method that allows for a fixed ΔV thruster to meet the mission requirements for a variety of ΔV requirements. The second technique, the method of linear perturbations on a reference trajectory, is used to close the guidance loop around a reference trajectory while allowing a vehicle to respond to uncertainties in its dynamics and still reach its objective.

3.1 General Energy Management Steering

General energy management (GEM) steering is a guidance technique that involves dumping of excess energy in order to put a vehicle on a particular trajectory. This is particularly useful for a vehicle that has a fixed $\Delta V_{capability}$. Essentially, the objective of GEM is to impart the change in velocity along some sort of curve so that the net ΔV imparted is less than the capability of the vehicle. This is particularly useful for solid rocket engines that do not have a capability for engine cut-off and have velocity requirements unknown until immediately prior to the start of the mission.

Figure 3-1 shows the path on which ΔV is acquired in a two-dimensional ΔV plane. The length of the curve $\Delta V_{capability}$ matches the capability of the vehicle while the ΔV_{net} is reduced from the capability of the engine such that it matches the $\Delta V_{required}$. GEM

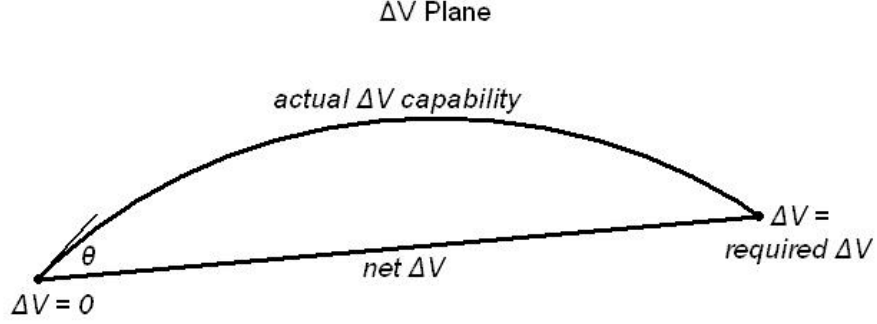


Figure 3-1: Basic General Energy Management

steering can be used to impart the change in velocity along any curve.

3.1.1 GEM Steering: A Simple Example

Consider a GEM maneuver that follows the arc of a circle in a plane, such as the one depicted in Figure 3-2. This will be referred to as a GEM-ARC maneuver. The ΔV_{net} is acquired along the x-axis as in Figure 3-2. Note that angle between the direction of thrust and the ΔV_{net} is known as θ . The total angular change in thrust direction during the maneuver is known as $\Delta\theta$. This corresponds to the difference between $\theta_{initial}$ and θ_{final} . Equation 3.1 defines the $\Delta\theta$, $\theta_{initial}$, and θ_{final} for a GEM-ARC burn. It is assumed that $\Delta\theta$ has a maximum value of 180° .

$$\theta_{initial} = \frac{1}{2}\Delta\theta = -\theta_{final} \quad \text{for GEM steering along an arc} \quad (3.1)$$

Using geometry, it is possible to find relationships between the amount of reduction in ΔV and the required $\theta_{initial}$ for a GEM-ARC burn. First, if the $\Delta V_{capability}$ is imparted along the arc of a circle, then r is the radius of the circle and Equation 3.2 relates the two. The length of the chord connecting the endpoints of the arc, ΔV_{net} , is given in Equation 3.3.

$$\Delta V_{capability} = 2r\theta_{initial} = r\Delta\theta \quad (3.2)$$

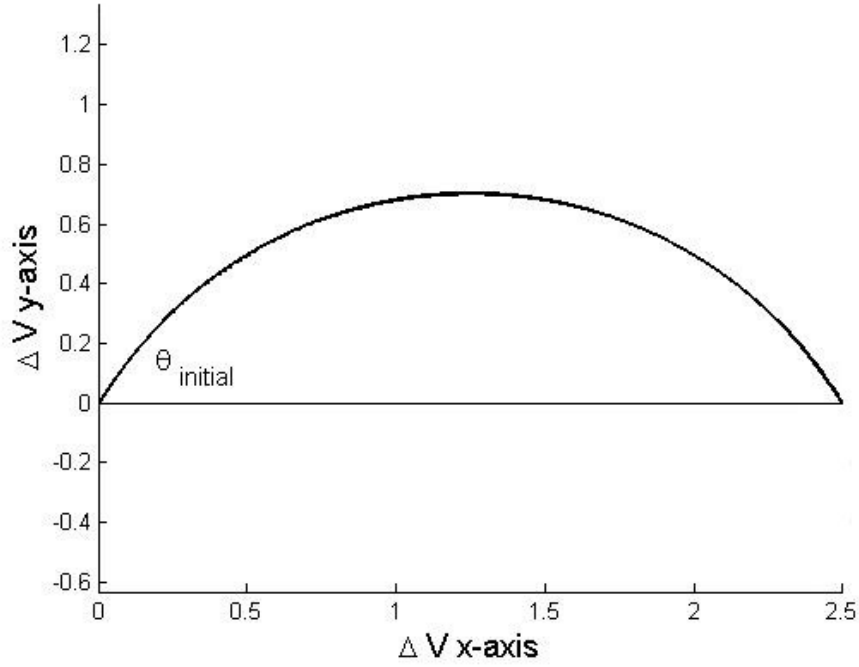


Figure 3-2: GEM Steering along the Arc of a Circle

$$\Delta V_{net} = 2r \sin \theta_{initial} = 2r \sin \left(\frac{\Delta \theta}{2} \right) \quad (3.3)$$

Therefore, by combining Equations 3.2 and 3.3, it is possible to define a relationship relating $\Delta \theta$ to the ratio between ΔV_{net} and $\Delta V_{capability}$, which describes how much the ΔV can be reduced.

$$\frac{\Delta V_{net}}{\Delta V_{capability}} = \frac{\sin \left(\frac{\Delta \theta}{2} \right)}{\left(\frac{\Delta \theta}{2} \right)} \quad (3.4)$$

The ratio on the left hand side of Equation 3.4 not only provides a reduction in the net ΔV delivered, but the inverse is the amount of “spare capacity” in ΔV that the spacecraft has at the beginning of the burn. If the final $\Delta V_{required}$ changes slightly during the course of the burn, there is an inherent robustness available and it may be possible to reach the revised $\Delta V_{required}$. Using the Taylor series expansion for $\sin \theta$, small values of $\Delta \theta$ can be solved for directly, as shown in Equation 3.7.

$$\frac{\Delta V_{net}}{\Delta V_{capability}} = \frac{\left(\frac{\Delta\theta}{2} - \frac{\Delta\theta^3}{48}\right)}{\left(\frac{\Delta\theta}{2}\right)} \quad (3.5)$$

$$= 1 - \frac{\Delta\theta^2}{24} \quad (3.6)$$

$$2\theta_{initial} = \Delta\theta = \sqrt{24 \left(1 - \frac{\Delta V_{net}}{\Delta V_{capability}}\right)} \quad (3.7)$$

Once the required ΔV is known, the angle between the initial and final thrust direction can be found. If there is a 180° change in thrust direction during the course of the burn, the maximum reduction in ΔV is 31.8% or $1/\pi$. If the desired ΔV is less than this value, there are other methods available to make the maneuver feasible, primarily by adding wait time prior to engine ignition. This is discussed more in Chapter 5. Reference [10] provides additional insight into GEM steering.

3.1.2 Application of GEM to the Example Spacecraft

Implemented on a spacecraft, a GEM maneuver that imparts the ΔV along a curve would involve some sort of attitude maneuvers during the burn, most likely with thrust vector control. The example spacecraft detailed in Appendix A has two stages with a 10 second stage separation in between. In order to impart velocity along the arc of the circle, the spacecraft must maintain a linear relationship between the attitude rates and the acceleration. For a two stage spacecraft, this may be difficult since the motion would have to be stopped at the end of the first stage burn, the inertial attitude fixed during the interstage time, and the rotation resumed at the start of the second burn. During the burns, the attitude rates would continually have to be increased in order to maintain the linear relationship between rates and acceleration. There are other types of GEM maneuvers available.

Figure 3-3 considers one type of GEM maneuver which will be referred to as Constant Rate GEM (GEM-CR). During this maneuver, a constant attitude rate is maintained.

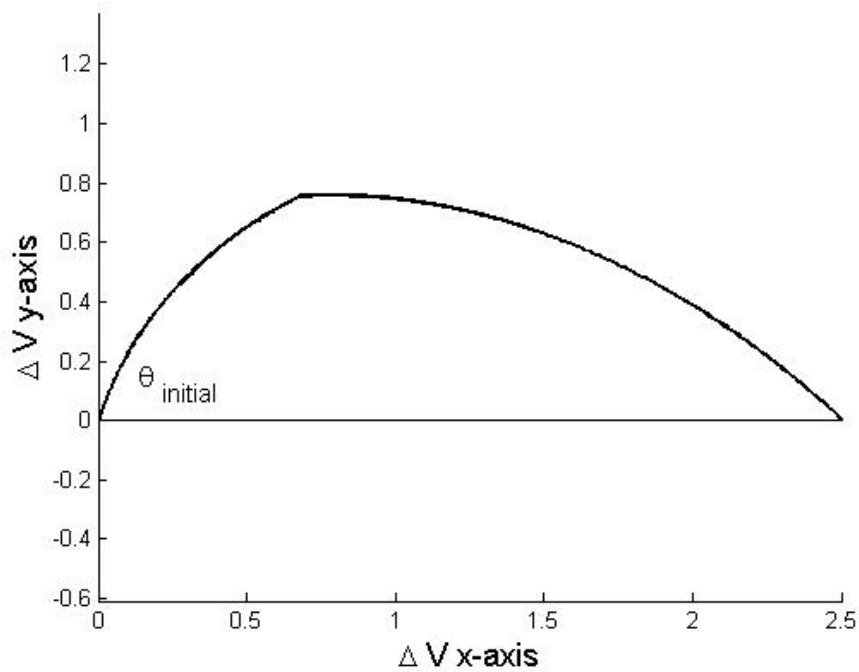


Figure 3-3: GEM Steering for Example Spacecraft with Constant Attitude Rates

Compare Figure 3-3 with Figure 3-2. Note that they both achieve a 1/6th reduction in velocity (from 3.0 km/sec to 2.5 km/sec). The dogleg in the ΔV space apparent in Figure 3-3 is due to the continued rotation during the interstage time.

Figure 3-4 compares GEM-ARC and GEM-CR. The acceleration profiles are identical, but GEM-ARC requires instantaneous changes in attitude rates where otherwise the two maneuvers accomplish the same goal.

Note that there are an infinite number of possible GEM maneuvers. GEM-ARC was shown because it is possible to find a mathematical expression that directly relates the burn to the reduction of ΔV . GEM-CR was introduced because it may be a logical starting point for the vehicle under consideration since a constant rate of attitude change imposes less stress on the attitude control system. Many additional variations of GEM are possible.

3.1.3 Closed-Loop Lambert GEM Guidance

Close-loop Lambert GEM is a method that dynamically determines the thrust direction based on the Lambert ΔV required to arrive at the rendezvous point and the current

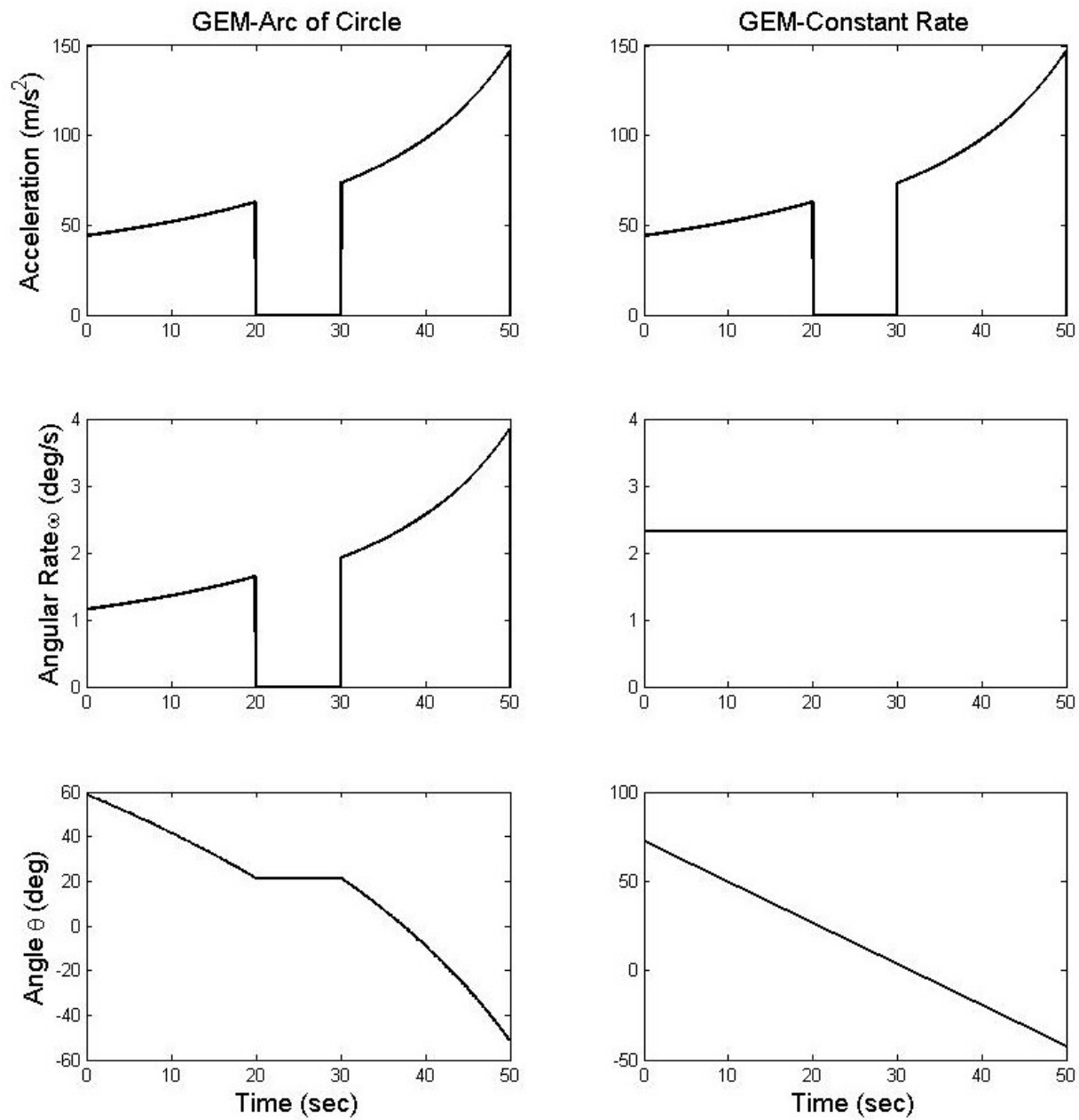


Figure 3-4: Comparison of GEM-Arc and GEM-CR for the Example Spacecraft

available ΔV based on the expected thrust impulse. Historically, variations of Lambert GEM have formed the basic components of closed loop guidance for solid rocket motors.

Consider a scenario where the spacecraft has current position \mathbf{r} and velocity \mathbf{v} at time t . At some time $t_{rendezvous}$ in the future, it must be at $\mathbf{r}_{rendezvous}$. The $\Delta \mathbf{v}_{instant}$ that will place the spacecraft on a transfer orbit taking it through the rendezvous point at the rendezvous time is given by the Lambert problem, discussed in Section 2.2.2. Equation 3.8 results from rearranging Equation 2.18.

$$\Delta \mathbf{v}_{instant}(t) = F_{Lambert}(\mathbf{r}, \mathbf{r}_{rendezvous}, (t_{rendezvous} - t)) \quad (3.8)$$

$$\|\Delta \mathbf{v}_{remaining}\| = \int_t^{t_{burnout}} \|\mathbf{a}_{thrust}(t)\| dt \quad (3.9)$$

Once the $\Delta \mathbf{v}_{instant}$ is solved with the Lambert problem, the next step is to compare that to the remaining acceleration impulse from the engines, or $\|\Delta \mathbf{v}_{available}\|$, given in Equation 3.9. Comparing those two values, it is possible to determine the thrust direction, $\hat{\mathbf{i}}_{thrust}(t)$ which is an angle $\theta(t)$ from the vector $\Delta \mathbf{v}_{instant}$.

$$\theta(t) = F(\Delta \mathbf{v}_{instant}, \|\Delta \mathbf{v}_{remaining}\|) \quad (3.10)$$

When doing this, it is desirable to have some simplifying assumptions about the GEM profile, such as that it follows the arc of a circle. This way, Equation 3.4 can be used to solve for Equation 3.10. Note that $\Delta V_{available}$ is really the remaining acceleration impulse. The algorithm depends only on the amount of remaining ΔV compared to the instantaneous ΔV required.

Equations 3.8, 3.9, and 3.10 form the algorithm for Lambert GEM or “closed-loop” Lambert GEM as it will be referred to here. While it will continuously update the thrust direction to take the vehicle close to the rendezvous point, closed-loop Lambert GEM does not automatically place the first stage on a reentry trajectory. Lambert GEM provides a starting point, but analysis has shown that accuracy can be much improved using a new method. Chapter 8 includes performance results from the closed-loop Lambert GEM algorithm compared to the new algorithm.

3.2 Method of Linear Perturbations upon a Reference Trajectory

The method of linear perturbations upon a reference trajectory is a proven method of closed loop guidance for vehicles with complex dynamics that can be modeled. The method is commonly used on aerospace vehicles to continually update the planned control inputs in order to reach an objective while responding to uncertainties.

Suppose the objective is to reach a given state specified as $\mathbf{r}_{objective}$. This thesis considers the objective of minimizing the error in position at the specified final time t_f . The first thing that is required is a reference or nominal trajectory. It is presumed that based on the dynamics models this reference trajectory is expected to place $\mathbf{r}(t_f)$ near $\mathbf{r}_{objective}$. Since the method of linear perturbations will respond to uncertainties, approximate methods can be used to find an initial reference trajectory.

There are a certain number of control inputs $c_1 \cdots c_n$ that fully define the vehicle's planned set of commands to the control system so that the vehicle will achieve this reference trajectory. The vector of control variables that specify the reference trajectory are denoted as \mathbf{c}_{ref} . According to the dynamics model, this set of reference trajectory control inputs is expected to drive the state to $\mathbf{r}_f(\mathbf{c}_{ref})$ at t_f . Therefore the expected error from this reference trajectory given by \mathbf{c}_{ref} is Equation 3.11.

$$\mathbf{e}(\mathbf{c}_{ref}) = \mathbf{r}_f(\mathbf{c}_{ref}) - \mathbf{r}_{objective} \quad (3.11)$$

Let $\Delta\mathbf{c}$ be a modification to the reference set of control inputs \mathbf{c}_{ref} . The error resulting from $\Delta\mathbf{c}$ is defined in Equation 3.12 as $\mathbf{e}(\mathbf{c}_{ref} + \Delta\mathbf{c})$.

$$\mathbf{e}(\mathbf{c}_{ref} + \Delta\mathbf{c}) = \mathbf{r}_f(\mathbf{c}_{ref} + \Delta\mathbf{c}) - \mathbf{r}_{objective} \quad (3.12)$$

The objective of the guidance algorithm is to find the reference solution \mathbf{c}_{ref} and subsequent modifications $\Delta\mathbf{c}$ that minimize the expected error $\mathbf{e}(\mathbf{c}_{ref} + \Delta\mathbf{c})$. In order to design the algorithm, information is needed about the effect of each control variable on the output. This is done by assuming that small perturbations in the control inputs

result in linear variations in the final position \mathbf{r}_f .

3.2.1 Estimating the Partial Derivatives of the Control Inputs

The next step is to estimate the partial derivatives of the control variables with respect to final state \mathbf{r}_f . The expected final state when using the reference trajectory control variables is $\mathbf{r}_f(\mathbf{c}_{ref})$ and is determined by running a nonlinear simulation of the trajectory using the reference control variables. Each control variable is perturbed by a small amount Δc_n and a nonlinear simulation is run in order to determine the change in final position $\Delta \mathbf{r}_f$ caused by the control input perturbation Δc_n .

$$\Delta \mathbf{r}_f = \mathbf{r}_f(\mathbf{c}_{ref} + \Delta c_n) - \mathbf{r}_f(\mathbf{c}_{ref}) \quad (3.13)$$

If each Δc_n is small, then it can be assumed to have a linear influence on $\mathbf{r}_f(\mathbf{c}_{ref} + \Delta c_n)$. Using this assumption, Equation 3.14 is the estimate of the partial derivative of \mathbf{r}_f with respect to each control variable c_n .

$$\left. \frac{\partial \mathbf{r}}{\partial c_n} \right|_{\mathbf{c}=\mathbf{c}_{ref}} = \frac{\mathbf{r}_f(\mathbf{c}_{ref} + \Delta c_n) - \mathbf{r}_f(\mathbf{c}_{ref})}{\Delta c_n} \quad (3.14)$$

Suppose there are n control variables $c_1 \cdots c_n$ and m dimensions of the state \mathbf{r}_f and error \mathbf{e} . Then the partial derivatives of each control variable with respect to each component of \mathbf{r}_f can be put in an $m \times n$ matrix \mathbf{D} which is a vector derivative of \mathbf{r}_f by \mathbf{c} . If perturbations of the control variables are kept in the linear range, then Equation 3.15 relates the any possible final state $\mathbf{r}_f(\mathbf{c}_{ref} + \Delta \mathbf{c})$ to the reference final state $\mathbf{r}_f(\mathbf{c}_{ref})$.

$$\mathbf{r}_f(\mathbf{c}_{ref} + \Delta \mathbf{c}) = \mathbf{r}_f(\mathbf{c}_{ref}) + \left[\frac{\partial \mathbf{r}}{\partial c_1} \quad \cdots \quad \frac{\partial \mathbf{r}}{\partial c_n} \right]_{\mathbf{c}=\mathbf{c}_{ref}} \begin{bmatrix} \Delta c_1 \\ \vdots \\ \Delta c_n \end{bmatrix} = \mathbf{r}_f(\mathbf{c}_{ref}) + \mathbf{D}(\mathbf{c}_{ref}) \cdot \Delta \mathbf{c} \quad (3.15)$$

3.2.2 Solving for the New Control Variables

The purpose of the method of linear perturbations upon a reference trajectory is to make minor modifications to the set of planned control inputs at every guidance step, continually compensating for dynamics uncertainties, such that the vehicle arrives at $\mathbf{r}_{objective}$. The goal is to find an equation that will, at each time step, solve for the changes in the control inputs in order to either minimize the expected value of \mathbf{e} or drive the expected value of \mathbf{e} to 0 with the most effective combination of control inputs. The exact process depends on the relative number of n control variables compared to the m states in $\mathbf{r}_{objective}$.

First, suppose that $m > n$. That means there are less control variables than states. The objective should be to find the $\Delta\mathbf{c}$ that minimizes the expected error $\mathbf{e}(\mathbf{c}_{ref} + \Delta\mathbf{c})$.

$$\text{minimize } J := \mathbf{e}(\mathbf{c}_{ref} + \Delta\mathbf{c})^T \mathbf{e}(\mathbf{c}_{ref} + \Delta\mathbf{c})$$

By substituting Equation 3.12 and 3.15 into the above optimization problem, the following optimization problem results.

$$\text{minimize } J := (\Delta\mathbf{c})^T \mathbf{D}^T \mathbf{D} (\Delta\mathbf{c}) + 2(\Delta\mathbf{c})^T \mathbf{D}^T \mathbf{e}(\mathbf{c}_{ref}) + \mathbf{e}(\mathbf{c}_{ref})^T \mathbf{e}(\mathbf{c}_{ref})$$

It is possible to form a simple least squares solution to solve for a linear combination of control inputs $\Delta\mathbf{c}$ that will minimize the expected error, \mathbf{e} . For this case, the solution for $\Delta\mathbf{c}$ is given in Equation 3.16 [5].

$$\begin{bmatrix} \Delta c_1 \\ \vdots \\ \Delta c_n \end{bmatrix}_{cmd} = \Delta\mathbf{c}_{cmd} = -(\mathbf{D}^T \mathbf{D})^{-1} \mathbf{D}^T \mathbf{e}(\mathbf{c}_{ref}) \quad (3.16)$$

Next, suppose that $m = n$ and that each of the partial derivatives $\partial\mathbf{r}/\partial c_n$ are linearly independent of one another. In this case, the control inputs that drive the expected error to zero can be solved directly with an inverse of the matrix of partial derivatives,

as shown in Equation 3.17. If there is uncertainty about the linear independence of the control inputs, it may be more advisable to use equation 3.16.

$$\begin{bmatrix} \Delta c_1 \\ \vdots \\ \Delta c_n \end{bmatrix}_{cmd} = \Delta \mathbf{c} = \mathbf{D}^{-1} \mathbf{e}(\mathbf{c}_{ref}) \quad (3.17)$$

Finally, consider the scenario where $m < n$ with at least m independent control variables. For this case, there are enough control variables to drive any expected error to zero at each guidance step even if not every single control is used. One solution would be to leave some control variables unchanged so that $m = n$ and use Equation 3.17 or 3.16. However, it is probably more desirable to include all control variables and create an algorithm that takes into consideration the relative preferences of certain control variables over others. Consider a diagonal weighting matrix \mathbf{W} shown in Equation 3.18. This matrix is specified by the engineer to impose costs associated with certain control variables. For instance, a certain vehicle may have a control variable A that uses fuel of which there is a finite supply while another control variable B is comes at no fuel cost. For this problem, the \mathbf{W} matrix would be used to show a preference of control variable B over control variable A.

$$\mathbf{W} = \begin{bmatrix} w_{c_1} & 0 & 0 \\ 0 & \ddots & 0 \\ 0 & 0 & w_{c_n} \end{bmatrix} \quad (3.18)$$

Each of the positive values $w_{c_1} \cdots w_{c_n}$ in Equation 3.18 is a penalty on changes to that control input. The smaller w_{c_n} is, the more desirable that control input is relative to the others. This is helpful if some of the control inputs come at the cost of limited resources or could increase some sort of risk.

Given the weighting matrix of Equation 3.18, the choice of control variables can then be formulated into a quadratic optimization problem. Equation 3.15 becomes a constraint. The problem is find a $\Delta \mathbf{c}_{cmd}$ with minimum control cost inside the feasible set of of possible $\Delta \mathbf{c}$ that drive the expected error to zero $\mathbf{e}(\mathbf{c}_{ref} + \Delta \mathbf{c})$.

$$\text{minimize } J := (\Delta \mathbf{c})^T \mathbf{W}(\Delta \mathbf{c})$$

$$\text{such that } \mathbf{D}\Delta \mathbf{c} + \mathbf{e}(\mathbf{c}_{ref}) = 0$$

The Karush-Kuhn-Tucker sufficient conditions for optimality for this quadratic program are expressed in equation 3.19 [3]. Note that the vector λ is the Lagrange multiplier.

$$\begin{cases} \mathbf{W}(\Delta \mathbf{c}) + \mathbf{D}^T \lambda = 0 \\ \mathbf{D}(\Delta \mathbf{c}) = \mathbf{e} \end{cases} \quad (3.19)$$

By putting Equation 3.19 into matrix form, the optimal perturbations to the control variables, $\Delta \mathbf{c}_{cmd}$, are easily determined and given in Equation 3.20.

$$\begin{bmatrix} \Delta c_1 \\ \vdots \\ \Delta c_n \end{bmatrix}_{cmd} = \Delta \mathbf{c} = \begin{bmatrix} \mathbf{I}_{n \times n} & \mathbf{0}_{n \times m} \end{bmatrix} \begin{bmatrix} \mathbf{W} & \mathbf{D}^T \\ \mathbf{D} & \mathbf{0}_{m \times m} \end{bmatrix}^{-1} \begin{bmatrix} \mathbf{0}_{n \times 1} \\ \mathbf{e} \end{bmatrix} \quad (3.20)$$

3.2.3 Implementation for Vehicle Guidance

So far, there has been little discussion on how this would be implemented on vehicle or what exactly the “nonlinear simulation” entails. At every guidance step, there is a full computer simulation of the remaining portion of the trajectory. The inputs to this simulation are the current full state vector, given by the vehicle’s navigation system, and the guidance reference trajectory defined by \mathbf{c}_{ref} . Note that \mathbf{c}_{ref} has been updated to include the control input perturbation solutions $\Delta \mathbf{c}_{cmd}$ for all previous steps. The simulation runs and predicts where the vehicle will be at time t_f if there are no modifications to the control inputs. Then for each control input c_n , a nonlinear simulation is run with a small perturbation Δc_n on c_n in order to determine the final position when that control variable is perturbed, or $\mathbf{r}_f(\mathbf{c}_{ref} + \Delta c_n)$. This is used to estimate the partial derivatives with Equation 3.14. Then either Equation 3.16, 3.17, or 3.20 is used to determine the modifications

to the control inputs that define a new reference trajectory. Chapter 6 applies the method of linear perturbations on a reference trajectory to the example spacecraft and mission.

[This page intentionally left blank.]

Chapter 4

Delta Velocity and Perigee Analysis

The spacecraft's fixed ΔV capability and the transfer orbit perigee constraints are two aspects of this problem which differentiate it from a more traditional orbital rendezvous problem. By exploring and manipulating many of the traditional astrodynamic relationships found in Chapter 2, this chapter derives mathematical relationships that are uniquely useful to the guidance problem posed by this thesis. When these relationships are illustrated through plots, they develop intuition for the problem and lead toward its solution. In addition, specific mathematical relationships will ultimately be implemented in guidance algorithms.

The basic idea of this chapter is to establish an understanding of how the net direction of thrust direction relates to the ultimate perigee altitude. In straightforward terms, it would be helpful to know which directions not to “aim” in order to meet the re-entry constraints. This will be accomplished using analytic methods. This chapter considers the two-body problem and a spacecraft with an instantaneous ΔV . The example spacecraft has a non-instantaneous burn, but the assumption of instantaneous burn is justified.

4.1 Relationship between Perigee and Velocity Changes

Initially, the orbiting spacecraft has position \mathbf{r}_0 and velocity \mathbf{v}_0 . Then at that particular instant, a vector change in velocity, $\Delta \mathbf{v}$, changes the trajectory and places it into a new transfer orbit around the earth. The particular characteristics of this new transfer orbit

are of interest. Specifically, it is important to understand how $\Delta \mathbf{v}$ contributes to the radius of perigee r_p . The velocity change is defined in Equation 4.1.

$$\mathbf{v} = \mathbf{v}_0 + \Delta \mathbf{v} \quad (4.1)$$

If the spacecraft was originally in a circular orbit, then r , a , p , r_p , and r_a are all equivalent. However, after the maneuver, the new semi major axis can be derived by rearranging the vis-viva integral of Equation 2.11 to form Equation 4.2. The scalar radius r is unchanged by the velocity impulse, while v is determined from Equation 4.1. Eccentricity e is simply the magnitude of the eccentricity vector \mathbf{e} .

$$a = \frac{\mu r}{2\mu - rv^2} \quad (4.2)$$

$$e = \sqrt{\mathbf{e}^T \mathbf{e}} \quad (4.3)$$

Combining Equation 2.5, 4.2, and 4.3 results in a representation of radius of perigee in terms of the post-impulse velocity vector \mathbf{v} in Equation 4.4. With Equation 4.1 allows the relationship between r_p and $\Delta \mathbf{v}$ can be determined for an arbitrary choice of coordinate frames.

$$r_p = a(1-e) = \frac{\mu r}{2\mu - rv^2} \left(1 - \sqrt{\left(\frac{1}{\mu} \mathbf{v} \times (\mathbf{r} \times \mathbf{v}) - \frac{1}{r} \mathbf{r} \right)^T \left(\frac{1}{\mu} \mathbf{v} \times (\mathbf{r} \times \mathbf{v}) - \frac{1}{r} \mathbf{r} \right)} \right) \quad (4.4)$$

4.1.1 Expressing Velocity in the RTN Frame

Section 2.4.2 introduced the Radial-Tangential-Normal reference frame. While Equation 4.4 was developed without regard to reference frame, using a carefully chosen reference frame can greatly aid the understanding of graphical output. Here, the initial parking orbit position \mathbf{r}_0 and velocity \mathbf{v}_0 are used to define the RTN coordinate system that will be used to analyze the post-impulse total velocity \mathbf{v} . Assuming that the parking orbit is circular, the following relationships will hold.

$$\mathbf{v} = \mathbf{v}_0 + \Delta\mathbf{v} = \begin{bmatrix} 0 \\ v_0 \\ 0 \end{bmatrix} + \begin{bmatrix} \Delta v_R \\ \Delta v_T \\ \Delta v_N \end{bmatrix} \quad (4.5)$$

$$v_0^2 = \frac{\mu}{r_0} \text{ for a circular orbit} \quad (4.6)$$

$$\mathbf{r} = \begin{bmatrix} r_0 \\ 0 \\ 0 \end{bmatrix} \quad (4.7)$$

4.1.2 General Result of Large Orbital Velocity Changes

The two body equation of motion dictates that all objects in orbit will remain in an invariant orbit. Given a particular spacecraft's position and velocity, or alternatively, its classical orbital elements, its current position as well as all past and future positions can be determined. If the orbit is circular or elliptic, the spacecraft will repeat itself around the same track again and again. The important question is understanding what these changes in velocity mean for the resulting orbit.

A non-zero $\Delta\mathbf{v}$ will simply place the spacecraft in a new orbit. If the velocities involved are not large enough to place the spacecraft in a parabolic or hyperbolic orbit, it will return the same place where the initial $\Delta\mathbf{v}$ was imparted. Thus, \mathbf{r}_0 will be a point in the new transfer orbit.

An illustration of this is included in Figure 4-1. In this case, the satellite is initially following a circular orbit. If, while the spacecraft is located at position \mathbf{r}_0 , an impulse $\Delta\mathbf{v}_1$ is applied in the direction of the current velocity such that $\Delta v_{1T} = 1km/sec$, it will enter a new transfer orbit. The perigee altitude of the new orbit is 500 km, identical to the original altitude of the spacecraft. In the second scenario, when the spacecraft is located at \mathbf{r}_0 , a $\Delta\mathbf{v}_2$ is applied in the direction opposite (retro) to the velocity vector such that $\Delta v_{2T} = -1km/sec$. In this case, the apogee is now located at \mathbf{r}_0 and the apogee altitude is the altitude of the original circular orbit, 500 km. Notice that the perigee altitude of this

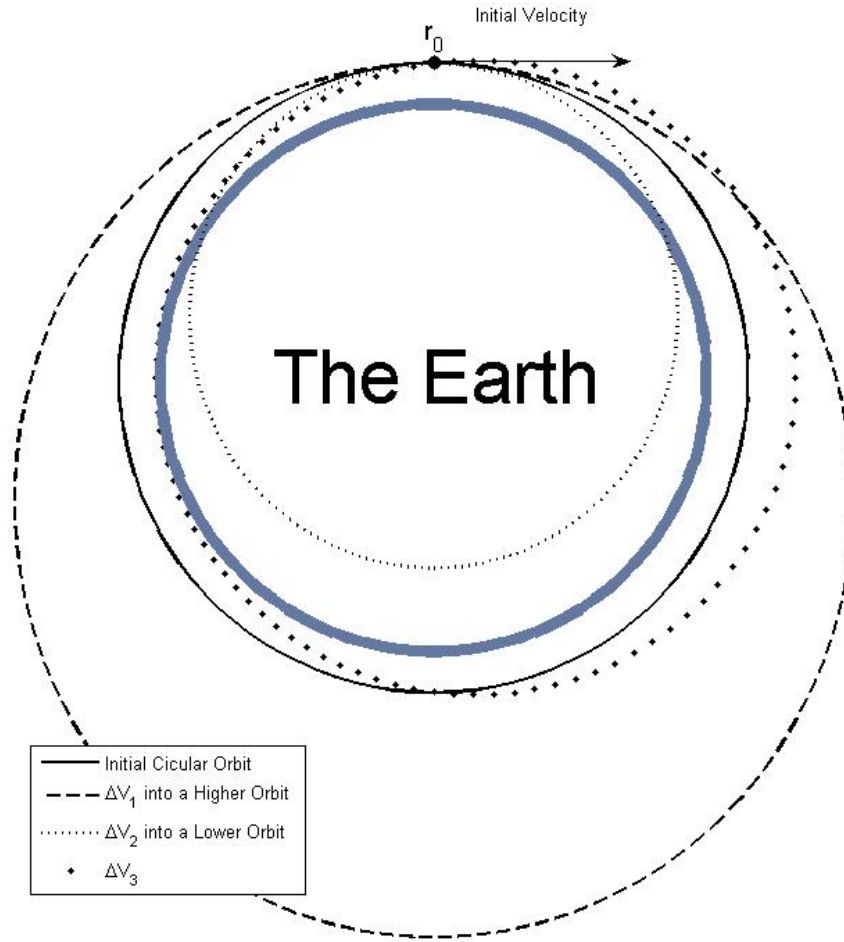


Figure 4-1: Graphical Results of Large Changes in Orbital Velocity

new elliptical orbit is negative, meaning below the earth's surface. For the third example, $\Delta \mathbf{v}_3$, the burn is in the local vertical (radial) direction such that $\Delta v_{3R} = 1km/sec$ and results in changing both the perigee and apogee.

The critical observation is that no matter what change in velocity is imparted, two body motion dictates that the new orbit will include the point at which the $\Delta \mathbf{v}$ was imparted (or, if the $\Delta \mathbf{v}$ is non-instantaneous, the point where engine burnout occurs). Therefore, the perigee of the new orbit must be at or lower than the original orbit radius and the apogee of the new orbit must be at or higher than the original orbit radius.

In real low-earth orbit scenarios, there are disturbing forces which break the two

Orbit	a	e	h_p	h_a
Initial Circular	6878 km	0	500 km	500 km
After $\Delta \mathbf{v}_1$	9553 km	0.280	500 km	5849 km
After $\Delta \mathbf{v}_2$	5523 km	0.245	-2211 km	500 km
After $\Delta \mathbf{v}_3$	6999 km	0.131	-298 km	1540 km

Table 4.1: Numerical Results of Large Changes in Orbital Velocity

body approximation and result in the spacecraft not returning to \mathbf{r}_0 . Depending on the orbital inclination, the J2 affect applies a twisting motion to the orbit plane, and thus the spacecraft will not reach \mathbf{r}_0 after one revolution, but rather another point at the same altitude and latitude, but a different longitude. Another effect ignored by the two body approximation is the firmness of the earth. Certainly, after $\Delta \mathbf{v}_2$, the spacecraft would fail to return to \mathbf{r}_0 because its trajectory would have taken it to a high speed impact with the earth's surface.

It turns out, that the examples of $\Delta \mathbf{v}_1$ and $\Delta \mathbf{v}_2$ are actually the two examples which maximize apogee and minimize perigee, respectively. For all $\|\Delta \mathbf{v}\| = 1$, the perigee and apogee values will be between those two extremes, including those that result from $\Delta \mathbf{v}_3$, which is verified in Table 4.1.

4.1.3 Graphical Representation of Perigee and $\Delta \mathbf{V}$

The previous section discussed the impact of a few specific $\Delta \mathbf{v}$'s on the new transfer orbit. The next step is to use Equation 4.4 to create a plot showing the general impact of changes in velocity upon perigee altitude.

Figure 4-2 shows contours of different perigee altitudes that result from $\Delta \mathbf{v}$'s imparted in the Tangential-Radial Plane, which is also the orbital plane of the initial parking orbit. The three sample transfers of Figure 4-1 and Table 4.1 all occur in this plane. It is evident that a $\Delta \mathbf{v}$ in the positive tangential (or velocity vector) direction cannot move the perigee altitude higher than the original orbit. However, a $\Delta \mathbf{v}$ in the negative tangential direction reduces the perigee altitude very quickly. This aligns with the astrodynamist's intuition, because in general planned spacecraft maneuvers leading to reentry involve a burn in the opposite direction of the velocity vector. Figure 4-2 also illustrates that burns with radial

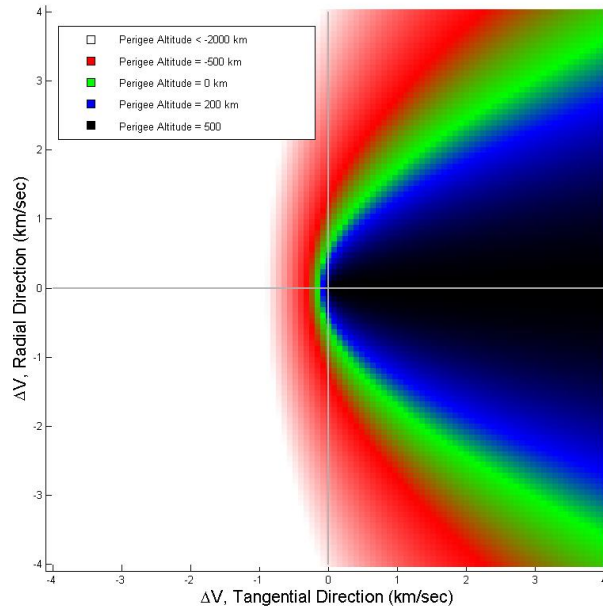


Figure 4-2: Contours of Perigee Altitude For R-T Components of $\Delta \mathbf{v}$

direction components tend to reduce the perigee altitude.

Figure 4-3 shows a similar plot in the Tangential-Normal plane. The characteristics along the tangential axis match up with Figure 4-2. However, burns with normal components will always change the orbit plane of the satellite, and may change neither the perigee or apogee, depending on the relative tangential component.

Figure 4-4 addresses how this affects the example spacecraft. The spacecraft can impart a maximum ΔV of 3.0 km/sec and this results in a sphere of maximum reach (or circle if it is a two-dimensional cross section). Next, since there is a re-entry constraint, there is really no distinction between a perigee just below the earth's surface and one that it is a few thousand kilometers below the earth's surface. All would meet the constraint. Thus, all perigee altitudes under the earth's surface are colored in green. There is a band of perigee altitudes above this that would inevitably lead to re-entry because of the cumulative impact of atmospheric drag. This area, assumed to be up to 100 km, is shaded in yellow because of the very high probability that re-entry would result. Perigee altitudes above this are shaded red because they generally would not meet the re-entry constraint for this mission. Figure 4-4 proves to be very useful if it is depicted how it might be used

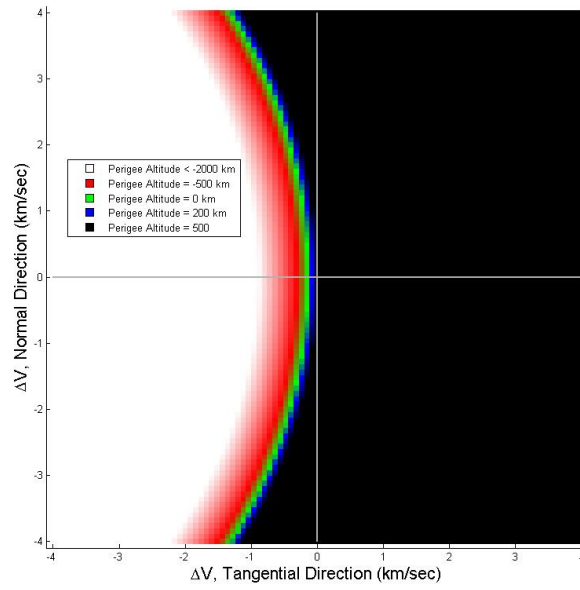


Figure 4-3: Contours of Perigee Altitude For T-N Components of $\Delta \mathbf{v}$

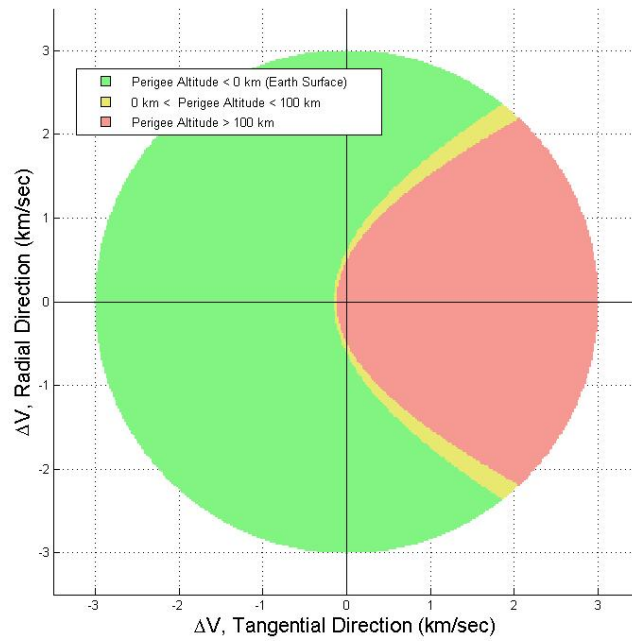


Figure 4-4: Perigee and R-T Components of $\Delta \mathbf{v}$, Example Spacecraft

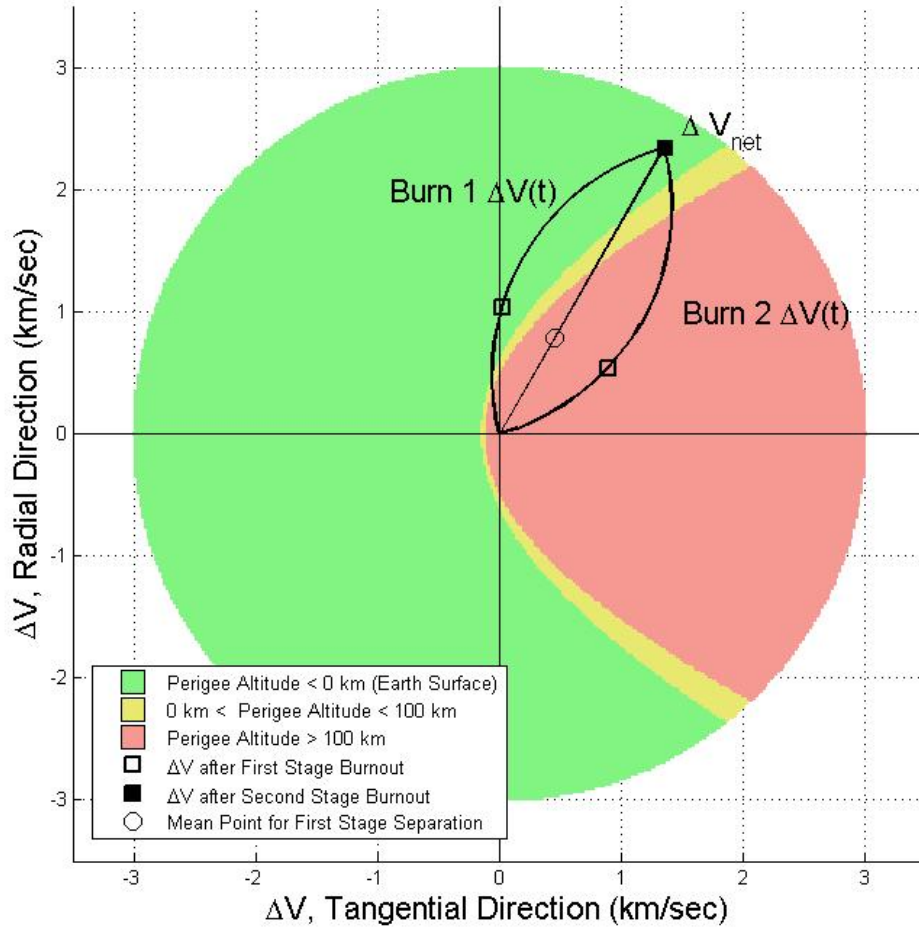


Figure 4-5: Perigee and R-T Components of $\Delta \mathbf{v}$, Example Spacecraft and GEM Maneuver

to choose particular general energy management paths.

Figure 4-5 demonstrates how the plot of $\Delta \mathbf{v}$ and perigee can be used to help solve this problem. A sample GEM-ARC maneuver has been overlaid upon Figure 4-4. In order to reach the desired $\Delta \mathbf{v}_{net}$ with the fixed $\Delta \mathbf{v}_{capability}$ of 3.0 km/sec, there are two possible routes in the T-R $\Delta \mathbf{v}$ plane that can accomplish the mission. If the desired $\Delta \mathbf{v}_{net}$ is already determined, the approximate reentry characteristics of the second stage and payload are predetermined. However, since the spacecraft is a two stage vehicle and the first stage has a reentry constraint as well, it is of importance where along the GEM arc the first stage separation occurs. For our example spacecraft, it is shown as the unfilled square in Figure 4-5. There are two possible GEM burns shown here as well as many more

that occur outside the T-R plane. As is evident here, one of the GEM maneuvers results in a perigee that would meet the constraint to be on a reentry trajectory, while the other clearly does not.

The objective would be to find out which of these many GEM maneuvers would allow the spacecraft to reach $\Delta \mathbf{v}_{net}$ with a perigee that will lead to reentry. While the magnitude of the $\Delta \mathbf{v}_{net}$ already dictates the $\Delta \theta$ of that GEM maneuver, the plane of that GEM maneuver can be chosen at will. A later section will develop a method to be used with the *mean point of first stage separation*, shown in Figure 4-5, to automatically minimize perigee. But first, the relationship between perigee and $\Delta \mathbf{v}$ will continue to be explored.

4.2 Hyperbolic Locus of Constant Perigee

Beginning with Figure 4-2, many of the figures in this chapter show resulting perigees for $\Delta \mathbf{v}$ components in the Tangential-Radial plane. Those curves of empirically determined constant perigee look strikingly close to hyperbolic curves. Thus, in this section, the mathematical relationships are explored in order to determine if the T-R plane produces hyperbolic curves of constant perigee. If they do, it may be possible to easily establish the three dimensional surfaces of constant perigee.

4.2.1 Mathematical Derivation of the Hyperbolic Locus of Constant Perigee

In this section, the preceding equations will be manipulated in order to arrive at a closed-form equation that define curves of constant perigee. The objective is to rearrange the equations relating $\Delta \mathbf{v}$ and perigee in order to arrive at the general equation for a hyperbola. Suppose that $\Delta \mathbf{v}$ is constrained to the T-R plane (it has no normal component). Then by combining Equations 2.7, 4.5, and 4.7, the angular momentum h of the the resulting orbit is given in Equation 4.8.

$$h = r_0(v_0 + \Delta v_T) \quad (4.8)$$

With Equation 2.8 and Equation 4.8 the parameter p of the transfer orbit is found to be Equation 4.9.

$$p = \frac{r_0^2(v_0 + \Delta v_T)^2}{\mu} \quad (4.9)$$

Equation 4.10 for the inverse of semi-major axis a of the transfer orbit results from the vis-viva relationship, Equation 2.11.

$$\frac{1}{a} = \frac{2}{r_0} - \frac{(v_0 + \Delta v_T)^2 + (\Delta v_R)^2}{\mu} \quad (4.10)$$

By combining the relationships between a , e , p , and r_p , stated in Equations 2.5 and 2.4, the following relations are developed.

$$\frac{r_p}{a} - 1 = e \quad (4.11)$$

$$\left(\frac{r_p}{a} - 1\right)^2 = e^2 \quad (4.12)$$

$$\frac{r_p^2}{a^2} - \frac{2r_p}{a} + 1 = 1 - \frac{p}{a} \quad (4.13)$$

$$\frac{r_p^2}{a} + p - 2r_p = 0 \quad (4.14)$$

The next step is combine Equations 4.9, 4.10, 4.14 and simplify.

$$\begin{aligned} r_p^2 \left(\frac{2}{r_0} - \frac{(v_0 + \Delta v_T)^2 + (\Delta v_R)^2}{\mu} \right) + \frac{r_0^2(v_0 + \Delta v_T)^2}{\mu} &= 2r_p \\ \left(\frac{r_0^2}{\mu} - \frac{r_p^2}{\mu} \right) (v_0 + \Delta v_T)^2 - \frac{r_p^2}{\mu} (\Delta v_R)^2 &= 2r_p - \frac{2r_p^2}{r_0} \\ \left(\frac{r_0^2 - r_p^2}{\mu} \right) (v_0 + \Delta v_T)^2 + \frac{r_p^2}{\mu} (\Delta v_R)^2 &= \frac{2(r_0 - r_p)r_p}{r_0} \end{aligned} \quad (4.15)$$

The purpose of the last several steps was to rearrange the equations relating r_p and

$\Delta \mathbf{v}$ into a form recognizable as the equation for a hyperbola.

Basic Equation for a Hyperbola

Equation 4.16 is the basic form of a hyperbola in cartesian coordinates that opens to the left and right with origin at $(x, y) = (h_{hyp}, k_{hyp})$.

$$\frac{(x - h_{hyp})^2}{a_{hyp}^2} - \frac{(y - k_{hyp})^2}{b_{hyp}^2} = 1 \quad (4.16)$$

Equation 4.15 can then be rearranged to the conventional form for a hyperbola in 4.16. The result is 4.17.

$$\frac{(\Delta v_T - v_0)^2}{2\mu \left(\frac{1}{r_0} - \frac{1}{r_0 + r_p} \right)} - \frac{(\Delta v_R)^2}{2\mu \left(\frac{1}{r_p} - \frac{1}{r_0} \right)} = 1 \quad (4.17)$$

The next step would be to plot various curves of constant perigee against the empirically determined shaded areas of Figure 4-4. The result is Figure 4-6. It is evident that the lines of constant perigee determined by putting various values for r_p into Equation 4.17 match up precisely with the shaded areas that were colored according to 4.4.

4.3 Exploring the Relationship between Perigee and $\Delta \mathbf{V}$

Until this point, only two-dimensional slices of three-dimensional $\Delta \mathbf{v}$ space have been considered when trying to understand the impact of $\Delta \mathbf{v}$ upon perigee altitude. At this point, the three dimensional surfaces of constant perigee will be plotted to give the reader a fundamental understanding of the impact of the perigee constraint and intuition for its three-dimensional impact.

4.3.1 Three Dimensional Surfaces of Constant Perigee

Figures 4-7 and 4-8 show the three dimensional surface corresponding to a perigee altitude of 0 km (the earth's surface). The partially transparent sphere corresponds to the sphere

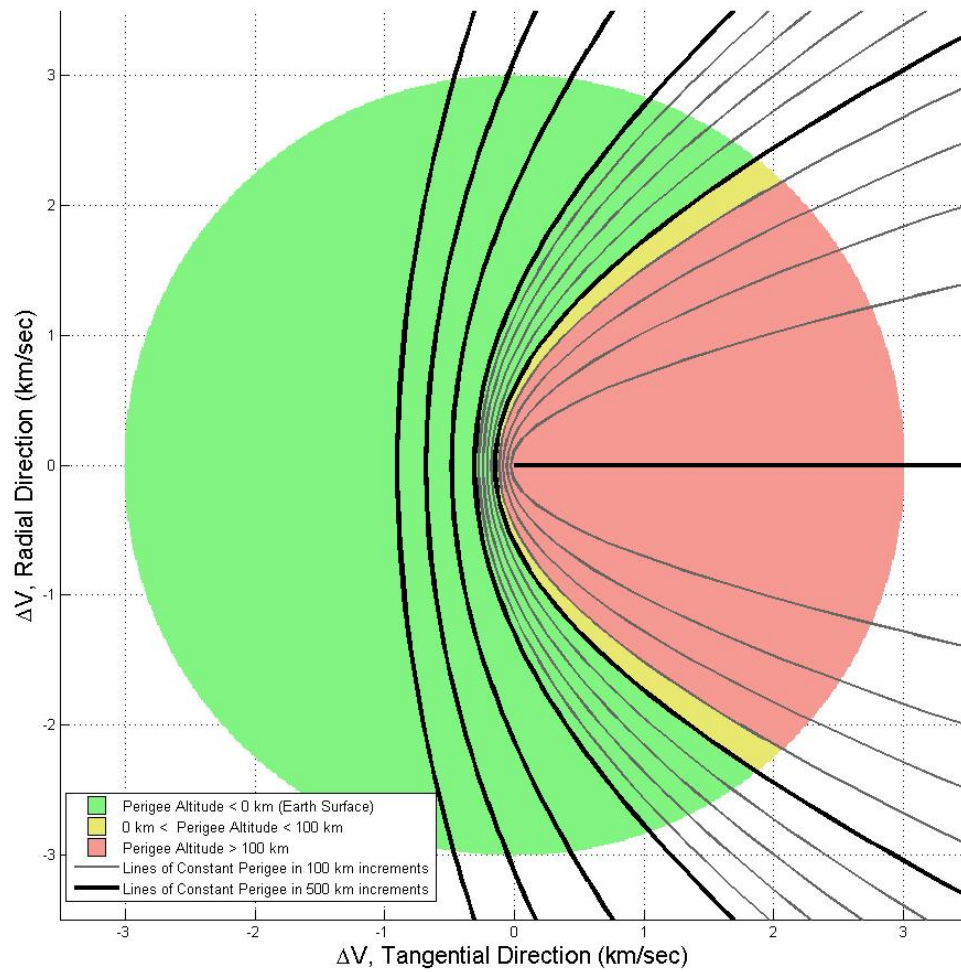


Figure 4-6: Hyperbolic Loci of Constant Perigee

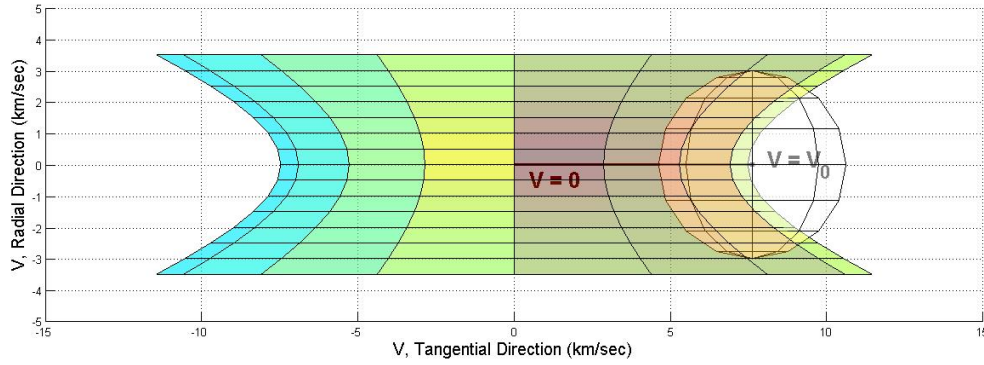


Figure 4-7: Surface of Constant Perigee

of possible post-burn velocity vectors emanating out from \mathbf{v}_0 with $\|\Delta\mathbf{v}\| = 3.0$. This 3D sphere corresponds to the 2D circle that has been shown in previous plots in this chapter. Note that the origin of the coordinate system in Figures 4-7 and 4-8 is at $\mathbf{v} = 0$ and not at $\Delta\mathbf{v} = 0$ like previous plots.

Figure 4-7 is a side view of the surfaces of zero perigee and maximum reach of $\Delta\mathbf{v}$. Since it only displays the Tangential and Radial components, its similarity to Figure 4-4 verifies that it was correctly created.

Figure 4-8 shows the same plot but from an angle that shows the characteristics of the Normal component of $\Delta\mathbf{v}$. This figure makes it apparent that perigee altitude depends most heavily on the tangential component of $\Delta\mathbf{v}$, with $\Delta\mathbf{v}$'s that are generally retro to the velocity vector significantly reducing perigee and $\Delta\mathbf{v}$'s generally aligned with the velocity vector failing to reduce perigee below the earth's surface. It is also visible that with a very large instantaneous $\Delta\mathbf{v}$, specifically $\Delta v_T = -2v_0$, it would be possible to completely reverse the direction while remaining in the same orbital path.

4.4 Gradient of Perigee with Respect to Velocity

The previous sections show the graphical relationship between perigee and the components of $\Delta\mathbf{v}$ in the radial-tangential plane. Figure 4-5 also suggests that the gradient of perigee

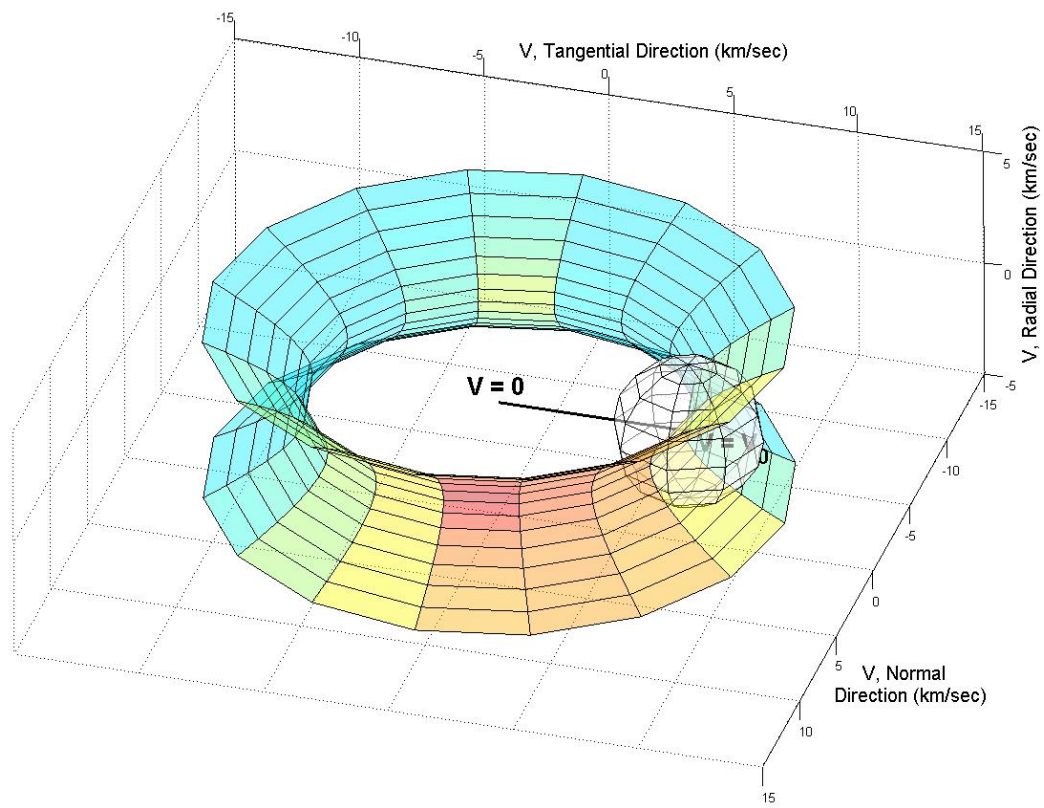


Figure 4-8: Three dimensional Surface of Constant Perigee

with respect to $\Delta \mathbf{v}$ could be used to minimize the perigee of the first stage. Here, a closed-form equation for the gradient of radius of perigee ∇r_p with respect to the vector quantity of $\Delta \mathbf{v}$ is developed. In future chapters, this will provide a valuable tool to automatically minimize the first stage perigee.

$$\nabla r_p = \frac{\partial r_p}{\partial \Delta \mathbf{v}} = \frac{\partial a}{\partial \Delta \mathbf{v}} (1 - e) - a \frac{\partial e}{\partial \Delta \mathbf{v}} \quad (4.18)$$

The gradient operator is simply a partial derivative. Equation 4.18 results from taking the partial derivative of Equation 2.5. A closed form solution requires an expression for a and e , which is available in Equations 4.2, and 4.3. It also requires the partial derivatives of those quantities with respect to $\Delta \mathbf{v}$ be expressed in a closed form solution.

4.4.1 Partial Derivative of Semi-Major Axis with respect to $\Delta \mathbf{V}$

Equation 4.18 contains two partial derivatives that so far have not been derived, including the partial of semi-major axis with respect to $\Delta \mathbf{v}$. In this section, this partial is derived. The derivation is started by using the chain rule to get 4.19, which shows three distinct partial derivatives that must be determined.

$$\frac{\partial a}{\partial \Delta \mathbf{v}} = \left(\frac{\partial a}{\partial v} \right) \left(\frac{\partial v}{\partial \mathbf{v}} \right) \left(\frac{\partial \mathbf{v}}{\partial \Delta \mathbf{v}} \right) \quad (4.19)$$

Next, Equation 4.2 is differentiated with respect to v to find Equation 4.20

$$\frac{\partial a}{\partial v} = \frac{2\mu r^2 v}{(2\mu - rv^2)^2} \quad (4.20)$$

Equation 4.21 is a simple result of vector calculus. The partial derivative of the magnitude of any vector with respect to the vector is the transposed unit direction along the vector.

$$\frac{\partial v}{\partial \mathbf{v}} = \frac{\mathbf{v}^T}{\sqrt{\mathbf{v}^T \mathbf{v}}} = \frac{\mathbf{v}^T}{v} \quad (4.21)$$

Differentiating Equation 4.1 results in Equation 4.22. This is also a simple result of vector calculus.

$$\frac{\partial \mathbf{v}}{\partial \Delta \mathbf{v}} = \mathbf{I}_{3 \times 3} \quad (4.22)$$

In this section, the partial derivative of a with respect to $\Delta \mathbf{v}$ was derived. Before calculating ∇r_p with Equation 4.18, $\partial a / \partial \Delta \mathbf{v}$ is determined by using Equations 4.19, 4.20, 4.21, and 4.22.

4.4.2 Partial Derivative of Eccentricity with respect to $\Delta \mathbf{V}$

Now that the first unknown quantity from Equation 4.18 has been determined, the second partial derivative will be found. The derivation once again begins by using the chain rule, this time on $\partial e / \partial \Delta \mathbf{v}$. The resulting relation is Equation 4.24. There are now three partial derivatives that must be solved for.

$$\frac{\partial e}{\partial \Delta \mathbf{v}} = \left(\frac{\partial e}{\partial \mathbf{e}} \right) \left(\frac{\partial \mathbf{e}}{\partial \mathbf{v}} \right) \left(\frac{\partial \mathbf{v}}{\partial \Delta \mathbf{v}} \right) \quad (4.23)$$

$$\frac{\partial e}{\partial \mathbf{e}} = \frac{\mathbf{e}^T}{\sqrt{\mathbf{e}^T \mathbf{e}}} = \frac{\mathbf{e}^T}{e} \quad (4.24)$$

Equation 4.24 results from differentiating Equation 4.3. Note that Equation 4.24 has a singularity when calculated at $e = 0$, which happens at $\Delta \mathbf{v} = 0$ starting from a circular orbit. The singularity exists because there is no gradient (or direction of increasing perigee) at where perigee is already at its maximum value. Using the expansion of the triple vector product [1], Equation 2.10 becomes Equation 4.25. Differentiation produces Equation 4.26, which can be rearranged into Equation 4.27 when the RTN frame is being used to represent velocity.

$$\mathbf{e} = \left(\frac{1}{\mu}\right) \left(\mathbf{r} (\mathbf{v}^T \mathbf{v}) - \mathbf{v} (\mathbf{v}^T \mathbf{r}) - \frac{1}{r} \mathbf{r} \right) \quad (4.25)$$

$$\begin{aligned} \frac{\partial \mathbf{e}}{\partial \mathbf{v}} &= \left(\frac{1}{\mu}\right) \frac{\partial}{\partial \mathbf{v}} \left(\mathbf{r} (\mathbf{v}^T \mathbf{v}) - \mathbf{v} (\mathbf{v}^T \mathbf{r}) - \frac{1}{r} \mathbf{r} \right) \\ &= \left(\frac{1}{\mu}\right) (2\mathbf{r}\mathbf{v}^T - \mathbf{I}_{3 \times 3} \mathbf{v}^T \mathbf{r} - \mathbf{v}\mathbf{r}^T) \end{aligned} \quad (4.26)$$

$$= \frac{1}{\mu} \begin{bmatrix} 0 & 2r_0(v_0 + \Delta v_T) & 2r_0\Delta v_N \\ -r_0(v_0 + \Delta v_T) & -r_0\Delta v_R & 0 \\ -r_0\Delta v_N & 0 & -r_0\Delta v_R \end{bmatrix} \quad (4.27)$$

Equation 4.27 illustrates that by choosing the correct frame and assuming that the spacecraft begins from a circular orbit, $\partial \mathbf{e} / \partial \mathbf{v}$ readily simplifies. The last partial derivative in Equation 4.23, $\partial \mathbf{v} / \partial \Delta \mathbf{v}$, was already given in Equation 4.22.

This section determined the second of the two partial derivatives contained in Equation 4.18. Now all quantities required to calculate $\nabla r_p(\Delta \mathbf{v})$ have been determined. The next section collects these different relationships into an algorithm to calculate $\nabla r_p(\Delta \mathbf{v})$.

4.4.3 Algorithm for Finding Gradient of Perigee

The applicable equations derived in this section have been gathered in Equation 4.28 as a quick reference for calculating $\nabla r_p(\Delta \mathbf{v})$. Note that there is a constraint upon the components of Δv that reflects that there is no direction of increasing perigee at points where perigee is already 500 km.

$$\left\{ \begin{array}{ll} \mathbf{v} &= \mathbf{v}_0 + \Delta \mathbf{v} \\ a &= \frac{\mu r}{2\mu - rv^2} \\ \mathbf{e} &= \left(\frac{1}{\mu}\right) \left(\mathbf{r} (\mathbf{v}^T \mathbf{v}) - \mathbf{v} (\mathbf{v}^T \mathbf{r}) - \frac{1}{r} \mathbf{r} \right) \\ \frac{\partial a}{\partial \Delta \mathbf{v}} &= \frac{2\mu r^2}{(2\mu - rv^2)^2} \mathbf{v}^T \\ \frac{\partial \mathbf{e}}{\partial \Delta \mathbf{v}} &= \left(\frac{\mathbf{e}^T}{e}\right) \left(\frac{1}{\mu}\right) (2\mathbf{r}\mathbf{v}^T - \mathbf{I}_{3 \times 3} \mathbf{v}^T \mathbf{r} - \mathbf{v}\mathbf{r}^T) \\ \nabla r_p &= \frac{\partial a}{\partial \Delta \mathbf{v}} (1 - e) - a \frac{\partial e}{\partial \Delta \mathbf{v}} \end{array} \right. \quad (4.28)$$

constrained by $e \neq 0 \Rightarrow \Delta \mathbf{v} \neq \mathbf{0}$

Figure 4-9 is a graphical depiction of the direction of the gradient of perigee with respect to $\Delta \mathbf{v}$. The gradient is orthogonal to the contours of constant perigee, which is consistent with expectations. Equation 4.28 has also been empirically verified by estimating the partial derivative of r_p with respect to $\Delta \mathbf{v}$ using perturbation methods. This confirms that there were no errors in the series of derivations that led to Equation 4.28. It is also evident that the contours of constant perigee of Figure 4-6 are perpendicular to the gradients of perigee shown in figure 4-9. This verifies one of the fundamental concepts of multi-variable calculus for this particular example.

4.4.4 Application of Gradient of Perigee to the Mission

It turns out that an approximation of the GEM maneuver plane and direction that minimizes first stage separation, as discussed in Section 4.1.3, can be found with the closed form solution of the the gradient of perigee with respect to the components of $\Delta \mathbf{v}$. Figure 4-5 shows an example of the *mean point for first stage separation*, or $\Delta \mathbf{v}_{MPFSS}$. This point is along the vector $\Delta \mathbf{v}_{net}$ at the point corresponding to the fraction of ΔV imparted by the first stage compared to the total vehicle ΔV .

When this gradient of perigee is calculated at $\Delta \mathbf{v}_{MPFSS}$, it returns the vector direction of fastest increasing perigee (opposite the direction fastest decreasing perigee). Chapter 6 explains how this can be used to define a plane of maneuver. If $\Delta \mathbf{v}_{net}$ defines one axis of the plane of maneuver, then $\nabla r_p(\Delta \mathbf{v}_{MPFSS})$ can be used to define the axis in such a way that the perigee of the first stage is minimum for all possible planes of maneuver that include $\Delta \mathbf{v}_{net}$. Chapter 6 covers this in greater detail.

4.5 Concluding Thoughts on Perigee and ΔV

The purpose of this chapter was to find the impact that different $\Delta \mathbf{v}$'s have on the reentry constraint. The figures shown help to illustrate what three-dimensional magnitude and

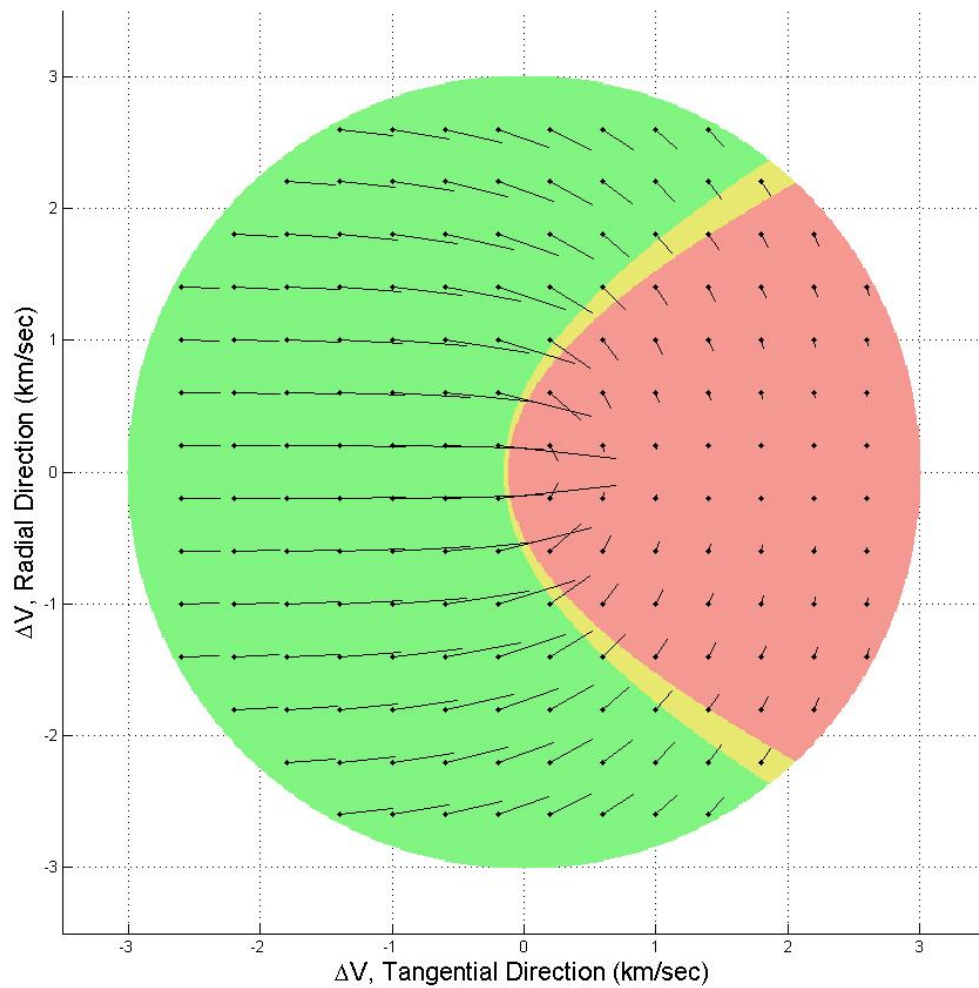


Figure 4-9: Gradient Field of Perigee With Respect to $\Delta \mathbf{v}$

direction combinations of $\Delta \mathbf{v}_{net}$ generally cause the spacecraft to fail to meet the re-entry requirement while also showing the directions of $\Delta \mathbf{v}_{net}$ that do meet the requirement. In Chapter 5, this is put to use to determine which of many transfer orbit paths should be followed in order to reach the objective under the mission constraints.

The last section developed a mathematical representation for the gradient of perigee. By using the direction of gradient of perigee in $\Delta \mathbf{v}$ -space, the plane and direction of the GEM burn can be determined in order to minimize perigee. Chapter 6 takes this equation for ∇r_p and puts it to use in an method to determine the most favorable plane of maneuver for a spacecraft's burn.

Chapter 5

Trajectory Boundary Condition Selection

This section addresses an important part of the overall problem posed by this thesis, which is referred to here as Trajectory Boundary Condition Selection (TBCS). The purpose is to determine the ignition time (t_{ignition}) and the rendezvous time ($t_{\text{rendezvous}}$). The ignition point and rendezvous point originally lie on two different trajectories. After fixing t_{ignition} and $t_{\text{rendezvous}}$, the boundary condition positions and the time of flight of the transfer is given, and the resulting transfer orbit is determined by the Lambert problem.

A similar astrodynamics problem given much attention in the literature is the targeting problem, which is typically concerned with minimizing ΔV for a particular maneuver. As a result of the example spacecraft and the mission considered here, minimizing ΔV is of no use. Instead, a cost function would consider other properties of a particular transfer orbit when seeking out the “best” trajectory. This Chapter also explores those relationships and draws general conclusions useful in understanding the problem.

5.1 Exploring the Problem

The first step in solving the TBCS optimization problem over two variables is to develop an understanding of the trade space. This is done by calculating a representative subset of the set of feasible transfer orbits, each one corresponding to a distinct t_{ignition} and

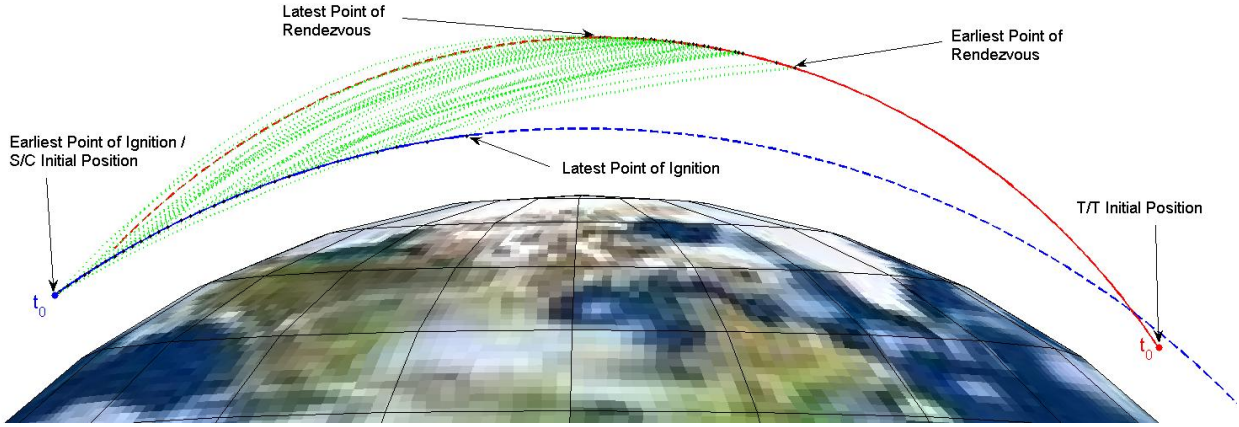


Figure 5-1: Exploring TBCS, Orbital Side View

$t_{rendezvous}$. The range of possible options can then be illustrated.

5.1.1 Sample Set of Initial Conditions

Consider a set of initial conditions that correspond to the example spacecraft at a 500 km circular orbit and a Keplerian trajectory in a coplanar elliptical orbit traveling in the opposite direction. Such a trajectory is shown in Figure 5-1, with the satellite in blue and the Keplerian trajectory in red. This Keplerian trajectory has a perigee altitude of approximately -2800 km and an apogee altitude of 1200 km. The relative geometry dictates that the rendezvous point occurs in the region near the apogee of this Keplerian trajectory. The initial position of each object is indicated in Figure 5-1 by t_0 , which is the earliest possible time that the spacecraft can ignite its engine and begin the rendezvous maneuver. These initial conditions and additional numerical details are given in Appendix B.

For these two trajectories, there are any number of possible transfer orbits connecting them. Suppose that these transfer orbits are constrained such they originate on the blue trajectory and terminate on the point on the red trajectory corresponding to the transfer time. Determining the transfer orbit trajectory simply requires solving the Lambert problem. Considering only transfer orbits that have an instantaneous ΔV less than the 3.0 km/sec available to the example spacecraft and that originate or terminate at 5 second intervals along the two trajectories. For these initial conditions, there are 3218 possible

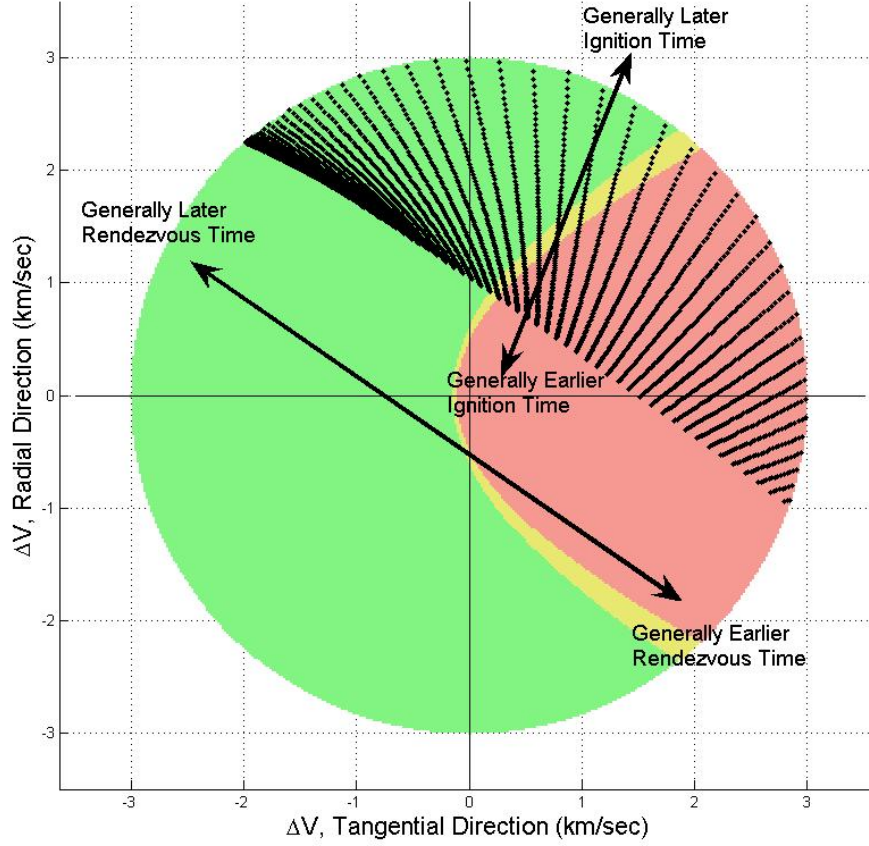


Figure 5-2: Exploring TBCS, ΔV and Perigee Contour Plot

transfer orbits. The path of every 100th transfer orbit has been plotted in Figure 5-1 as a green trajectory, with the position at ignition and rendezvous shown as black dots. The earliest and latest possible ignition and rendezvous points are also indicated in the figure.

Since the original satellite and target orbits are coplanar, the transfer orbits also lie in that plane. Since the $\Delta \mathbf{v}$'s lie in the original orbit plane and all the Δv_N components are zero, the radial and tangential components of all 3218 transfers can be plotted on the $\Delta \mathbf{v}$ and perigee contour plots described in depth in Chapter 4. These are depicted in Figure 5-2.

For the particular initial conditions under consideration, it is evident that there is a wide variety of possible $\Delta \mathbf{v}$ directions for transfer orbits. Some would lead to rapid reentry while some clearly do not lower the perigee significantly and have poor reentry

Property	Minimum Value	Maximum Value
Perigee Altitude (km)	-3876	500
Apogee Altitude (km)	1187	217976
Ignition Time (sec)	0	455
Rendezvous Time (sec)	565	850
Magnitude of ΔV (km/sec)	0.86	3.00
Relative Velocity (km/sec)	10.92	15.73
Effective Plane Change (deg)	0.00	0.00

Table 5.1: Exploring TBCS, Bounds of Properties for 3218 Transfer Orbits

characteristics. Similarly, the magnitude $\|\Delta \mathbf{v}\|$ also varies substantially. Note that a discrete subset of all possible transfer orbits are shown in Figure 5-2 and that the space between the existing $\Delta \mathbf{v}$'s in the $\Delta \mathbf{v}$ T-R plane would also lead to transfer orbits with slightly different ignition and rendezvous times than the points in the neighborhood.

Each of the 3218 possible transfer orbits have different characteristics including those mentioned so far such as perigee altitude or rendezvous time and others that may be of interest such as angle of effective orbital plane change and apogee altitude. Table 5.1.1 summarizes the minimum and maximum values for various properties that result from the family of transfer orbits. Note that one transfer would raise the apogee to 35 earth radii.

5.1.2 Constraining Ignition Time

So far, it is clear that there are a great deal of transfer orbits with a wide variety of characteristics to pick from. There are a few key generalizations that can be made about the problem to develop intuition. Figure 5-3 illustrates how fixing the ignition time changes the problem. In this instance, the ignition time t_{ignition} has been fixed to time t_0 , which is the time for which the initial conditions \mathbf{r}_0 and \mathbf{v}_0 are defined.

The horizontal axis is the transfer time as well as the rendezvous time since $t_{\text{ignition}} = 0$. Understandably, as the transfer times goes to zero, the $\|\Delta \mathbf{v}_{\text{required}}\|$ goes toward infinity. As transfer time increases, the $\|\Delta \mathbf{v}_{\text{required}}\|$ gradually decreases until it reaches a minimum and then begins to increase again. It must dip below the level of $\|\Delta \mathbf{v}_{\text{available}}\|$ in order for a transfer to be theoretically possible at that particular t_{ignition} . The earliest possible

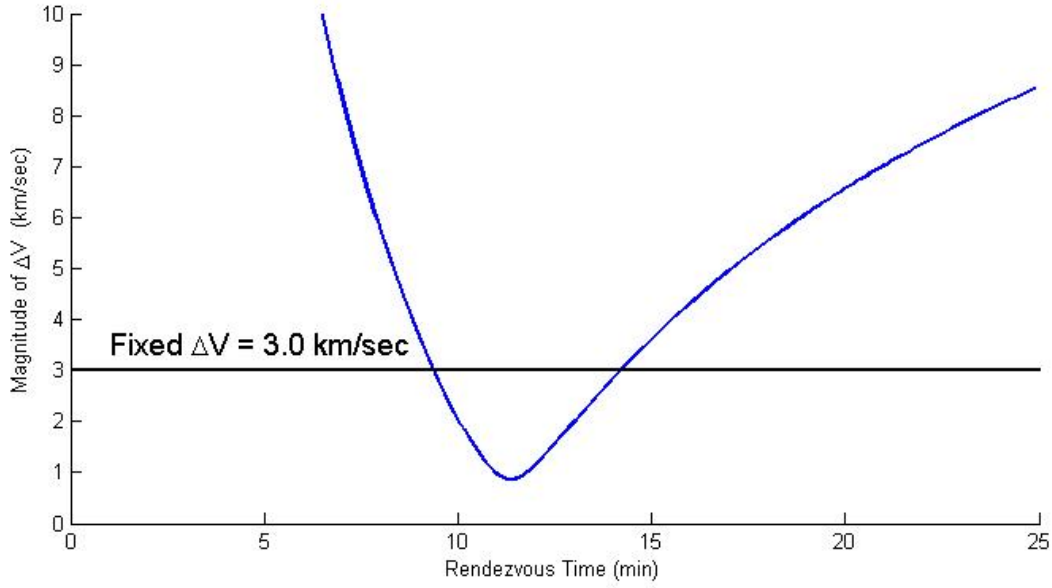


Figure 5-3: Exploring TBCS, Magnitude of ΔV for Fixed Ignition Time

ignition time ($t_{\text{ignition}} = t_0$) will lead to the earliest and latest possible rendezvous times for the given set of initial conditions.

In general, fixing ignition times will result in $\|\Delta \mathbf{v}_{\text{required}}\|$ curve similar to the one shown in Figure 5-3 where there is a minimum value at some $t_{\text{rendezvous}}$ in the future. If t_{ignition} is increased, the blue $\|\Delta \mathbf{v}_{\text{required}}\|$ curve tends to move up and to the left, until the point when $\|\Delta \mathbf{v}_{\text{required}}\|$ is equal to the line of $\|\Delta \mathbf{v}_{\text{available}}\|$. This is true under all possible initial conditions, except in cases where the earth or atmosphere would prevent transfers that are theoretically possible given the two body equation of motion. That point is the latest possible ignition time. Depending on the initial conditions, care should be used to assure that the transfer orbits do not follow a path that intersects the earth or atmosphere before reaching the rendezvous point.

5.1.3 Constraining Rendezvous Time

Another important observation comes from when the point of rendezvous is fixed. In this case, the initial conditions from Figure 5-1 are used and a fixed $t_{\text{rendezvous}} = 685$ sec fixes one of the boundary conditions.

Figure 5-4 illustrates how delaying the ignition time while fixing rendezvous time will

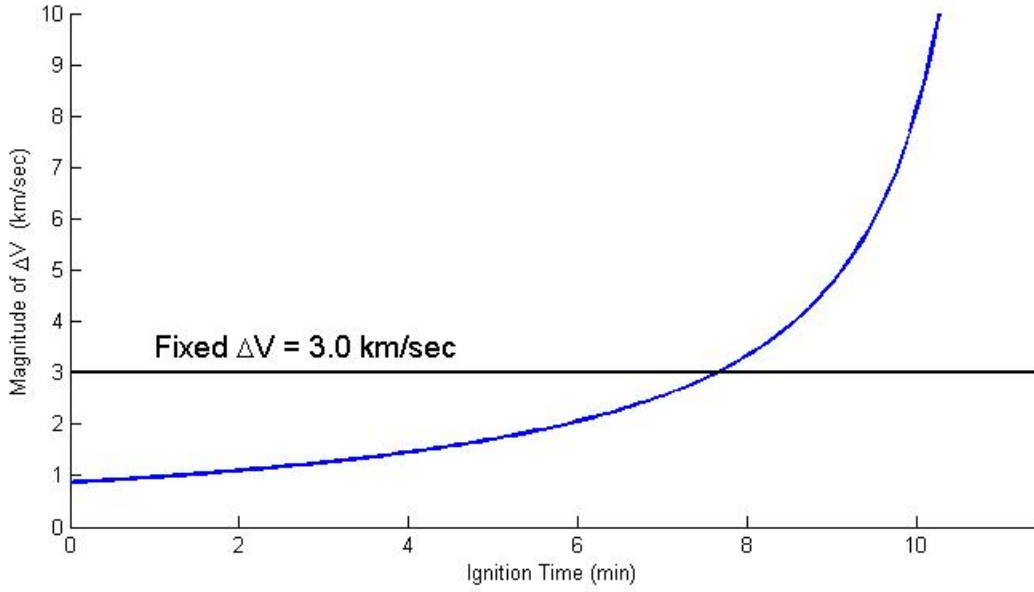


Figure 5-4: Exploring TBCS, Magnitude of ΔV for Fixed Rendezvous Time

always increase the $\Delta \mathbf{v}_{required}$. This is an important observation. For instance, for one particular scenario, it might be possible that the $\Delta \mathbf{v}_{required}$ is much smaller than the smallest $\Delta \mathbf{v}_{net}$ achievable with GEM. Recall that Section 3.1 explains that the largest reduction of ΔV achievable with $\Delta \theta = 180$ degrees along the arc of a circle is 31.8%. When an greater reduction of ΔV is desired, increasing the wait time will lead to an achievable ΔV .

5.2 Formulation into an Optimization Problem

With a few assumptions, TBCS essentially becomes an optimization problem over two variables, $t_{ignition}$ and $t_{rendezvous}$. A substantial number of spacecraft trajectory optimization and targeting problems are concerned with minimizing the single variable ΔV , in order to conserve fuel for later stages of a mission. As a result of the assumed example spacecraft having fixed ΔV engines, there is no reward or even ability to reduce ΔV . Therefore, instead of optimizing over ΔV expended, it is possible to look at other characteristics. Some properties of the transfer orbit that engineers may be interested in include:

- The perigee altitude, h_p , which significantly impacts the reentry characteristics.
- The apogee altitude, h_a , which partially impacts the reentry characteristics.
- The rendezvous time, $t_{rendezvous}$. Perhaps the mission calls for an earlier or later rendezvous time.
- The expected $\Delta\theta$ of the GEM maneuver to achieve the reduction in velocity. This is essentially a comparison of the $\|\Delta\mathbf{v}_{available}\|$ compared to the $\|\Delta\mathbf{v}_{net}\|$. Too small a value for $\Delta\theta$ may negatively impact the ability respond to changes in $\Delta\mathbf{v}_{net}$. Too large a value for $\Delta\theta$ may not be realistically achievable with the hardware. For instance, imparting the ΔV with a change in thrust direction of more than 180 degrees may be unrealistic for the short burn duration or selection of hardware.
- The magnitude or direction of any relative motion at rendezvous time.
- Re-entry flight path angle.
- Any other measure reflecting particular aspects of the transfer orbit and/or the spacecraft's ability to reach the rendezvous point.

One mission may dictate an interest in simple minimization or maximization of one of these variables. A different mission may place roughly equal importance on two or more of the variables. Still another might place hard constraints on some of these properties, effectively removing possible transfer orbits from consideration, while calculating the comparative cost between the remaining choices. Ultimately, the goal is for TBCS to algorithmically pick the most desirable transfer orbit. Thus, the purpose of the cost function is to mathematically capture the subjective preferences, priorities, and concerns of the human mission managers while maximizing likelihood of mission success.

5.2.1 Determining an Example Cost Function

To demonstrate how a simple TBCS cost function might work, a cost function has been created to capture hypothetical preferences for a mission. For this scenario, the particular transfer orbit has been selected based on three criteria: (1) The perigee shall be

constrained to transfer orbits that lead immediately to reentry, including a margin for error. A small quadratic cost is also applied to transfers which technically meet the constraint but are on the border area. (2) If possible, the $\Delta \mathbf{v}_{net}$ shall have a magnitude between 2.3 and 2.7 km/sec, with a quadratic penalty added to those that are further away. This provides a $\Delta \theta$ that leaves a little $\Delta \mathbf{v}_{net}$ wiggle room in the final $\Delta \mathbf{v}_{net}$ imparted but at the same time leads to angular rates that are realizable for the spacecraft control system. (3) A linear cost penalty is applied so that earlier rendezvous times are more desirable than later rendezvous times. The actual cost function equation used in this research is detailed in Appendix B.

The cost function here is not precise. In theory an optimum value could be reached, but it is more important to have a “ballpark” good answer. In this scenario, the Lambert routine was called approximately 10^4 times which in most cases should be realizable for a spacecraft flight computer. For most cases, that provides enough points that a good transfer orbit solution will emerge when the cost is evaluated for each point.

With just a simple comparison of costs, this method is not the most elegant spacecraft targeting routine ever implemented, but it gets the job done. The next step is to apply this quick optimization routine to the example set of initial conditions discussed in Section 5.1 to see if the algorithm returns the transfer orbit that is expected based on the preferences built into the cost function.

5.2.2 TBCS Scenario 1: Coplanar Rendezvous, Opposite Direction of Travel

The first scenario used to explore the TBCS optimization method started with initial conditions corresponding to two coplanar trajectories approaching head on toward each other. The transfer orbits are calculated and the optimized transfer is simply the one with lowest cost. Table 5.2 shows how the various properties for the optimized transfer compare to the upper and lower bounds of those properties for the set of possible transfer orbits. This provides an idea of how well the optimization routine was able to balance the competing properties included in the cost function.

Property	Minimum	Maximum	Optimized Transfer
Perigee Altitude (km)	-3876	500	-214
Apogee Altitude (km)	1187	217976	10534
Ignition Time (sec)	0	455	405
Rendezvous Time (sec)	565	850	665
Magnitude of ΔV (km/sec)	0.86	3.00	2.54
Relative Velocity (km/sec)	10.92	15.73	13.99
Effective Plane Change ($^{\circ}$)	0.00	0.00	0.00

Table 5.2: TBCS Scenario 1, Optimized Transfer Orbit Properties

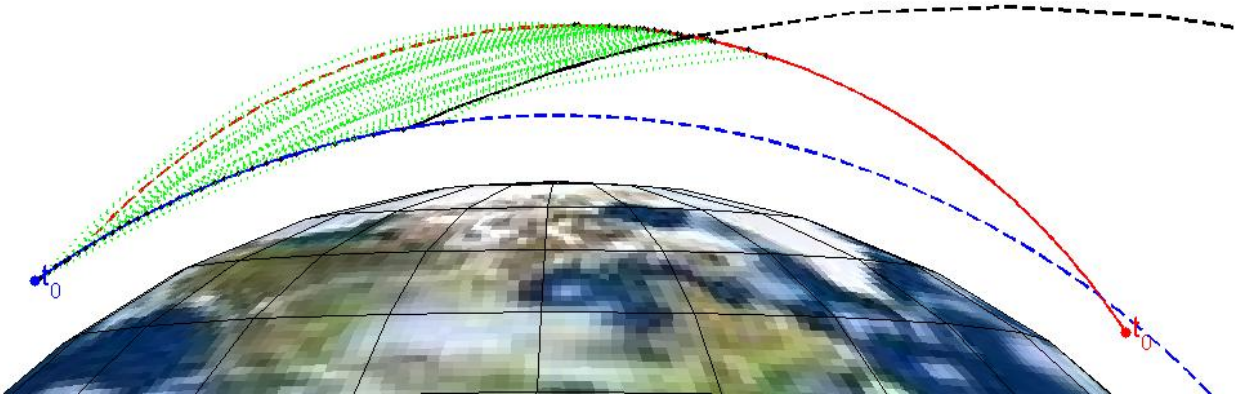


Figure 5-5: TBCS Scenario 1, Transfer Orbit Side View

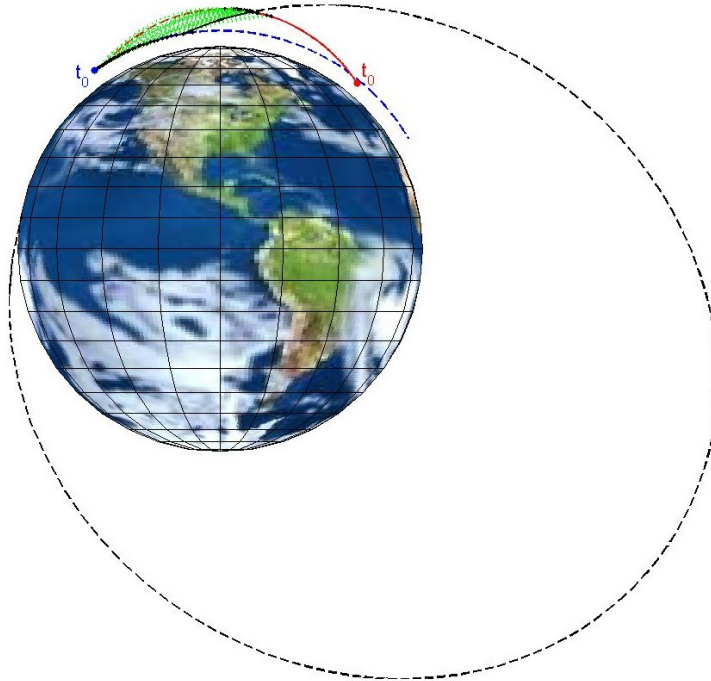


Figure 5-6: TBCS Scenario 1, Transfer Orbit Global View

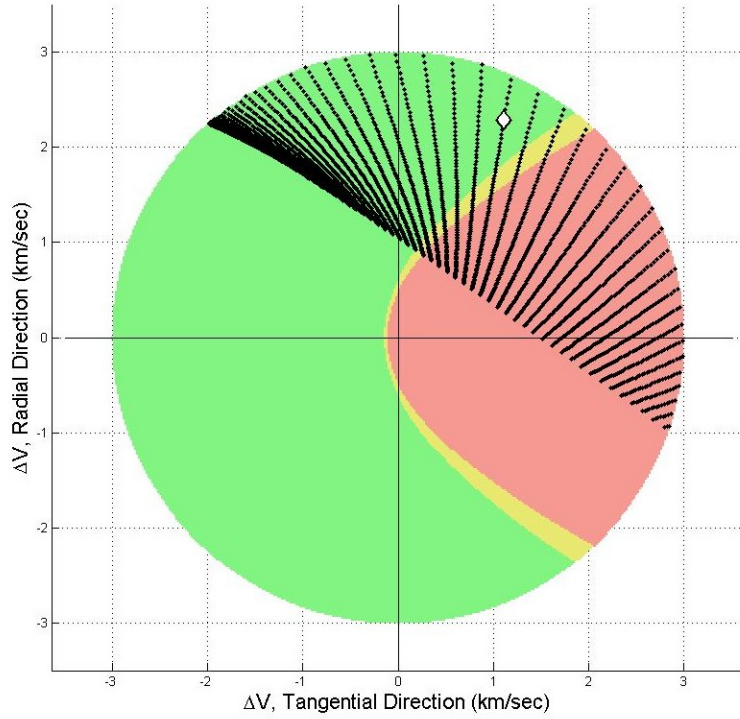


Figure 5-7: TBCS Scenario 1, Optimized Transfer and ΔV and Perigee Contour Plot

Figure 5-5 illustrates where the transfer orbit lies relative to the spacecraft and Keplerian trajectories. The actual transfer is shown as a solid black line while the dashed black line shows the continued path after passing $t_{rendezvous}$. Figure 5-5 shows the same image from a global perspective and makes the ultimate orbit that the spacecraft follows intuitively clear, including the height of apogee and how the transfer orbit ultimately intersects the earth as a result of a negative perigee altitude.

The location of the optimized $\Delta \mathbf{v}_{net}$ with respect to the ΔV and perigee contour plot is shown in Figure 5-7 as a white diamond. It is readily apparent that the chosen transfer orbit matches the prerogatives of the cost function. The $\Delta \mathbf{v}_{net}$ is just inside the green area and thus has a negative perigee altitude. As shown in both Table 5.2 and Figure 5-7, the $\|\Delta \mathbf{v}_{net}\|$ has been reduced to approximately 2.5 km/sec, effectively. Finally, Table 5.2 and Figure 5-5 indicate that $t_{rendezvous}$ for the optimized transfer is relatively early, only 100 seconds after the earliest possible $t_{rendezvous}$.

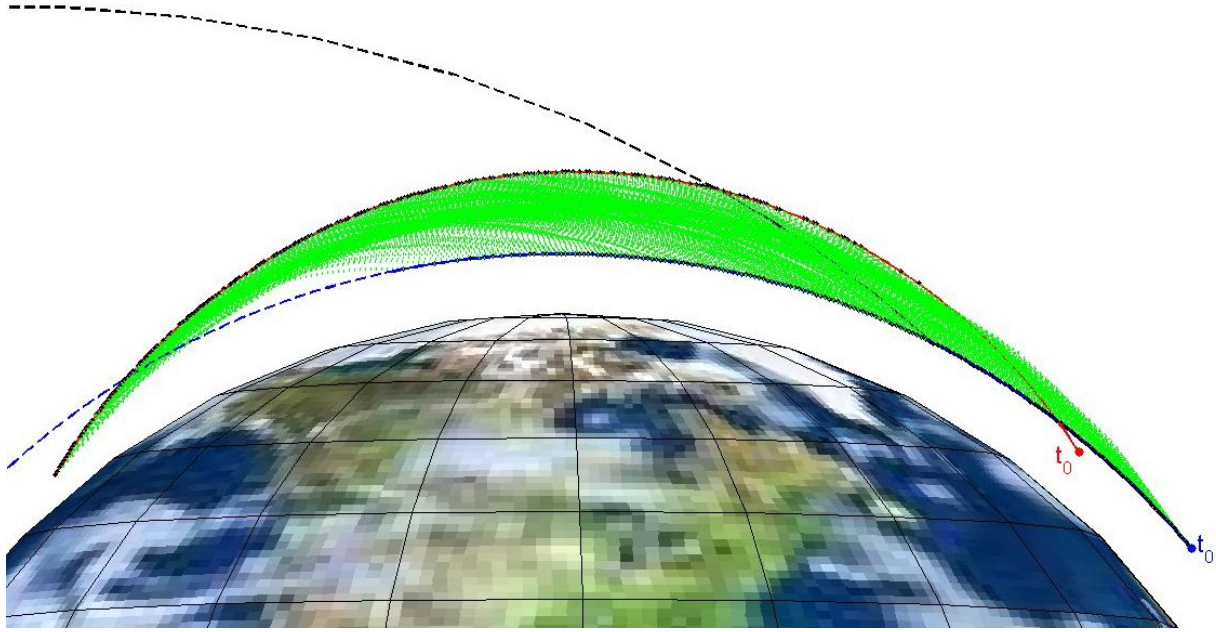


Figure 5-8: TBCS Scenario 2, Transfer Orbit Side View

5.2.3 TBCS Scenario 2: Coplanar Rendezvous, Same Direction of Travel

The next scenario explores what might be called a tail chase approach. This simply means that both the spacecraft as well as the Keplerian trajectory of possible rendezvous points lie in the same orbital plane and travel is in the same direction. Thus, at the initial conditions, the spacecraft is behind and traveling in the same direction as a vehicle would in the Keplerian trajectory. The initial positions and velocities of the two is illustrated in Figure 5-8. The same cost function as Scenario 1 was used to select the optimized black transfer orbit from a great number of possible transfer orbits.

Figure 5-9 illustrates the ultimate path of the vehicle on the global scale. Just as in Scenario 1, the spacecraft reenters the atmosphere less than one revolution later. Table 5.3 summarizes the applicable properties of the optimized transfer, comparing them to the range of values for family of transfer orbits given by the initial conditions.

Since the initial trajectories of Scenario 2 are coplanar and lead to coplanar transfer orbits it is possible to show the range of possible transfer orbits $\Delta \mathbf{v}$'s on a two-dimensional perigee contour plot. Figure 5-10 shows the radial and tangential components of $\Delta \mathbf{v}$ for

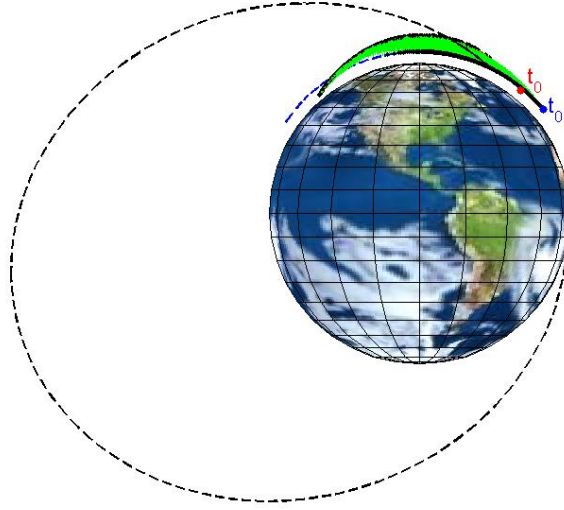


Figure 5-9: TBCS Scenario 2, Transfer Orbit Global View

Property	Minimum	Maximum	Optimized Transfer
Perigee Altitude (km)	-4603	498	-200
Apogee Altitude (km)	657	219768	11289
Ignition Time (sec)	0	985	365
Rendezvous Time (sec)	305	1675	615
Magnitude of ΔV (km/sec)	0.77	3.00	2.59
Relative Velocity (km/sec)	0.39	4.17	3.26
Effective Plane Change ($^{\circ}$)	0.00	0.00	0.00

Table 5.3: TBCS Scenario 2, Optimized Transfer Orbit Properties

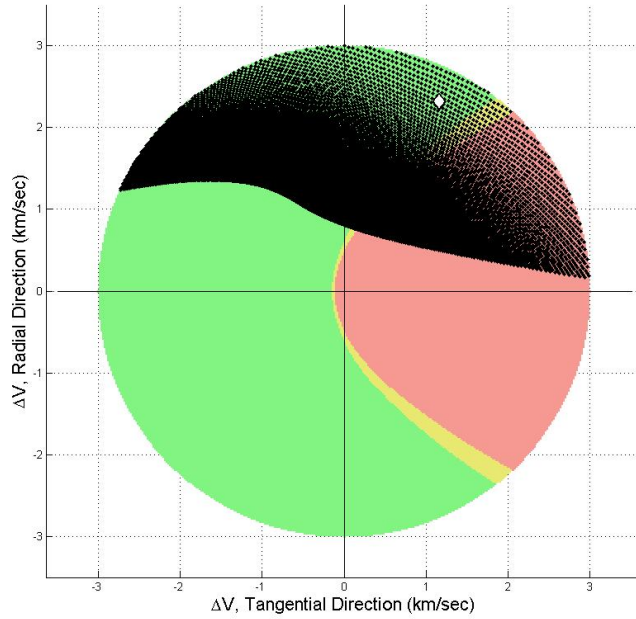


Figure 5-10: TBCS Scenario 2, Optimized Transfer and ΔV and Perigee Contour Plot

all possible transfer orbits. Note that in R-T coordinates, the $\Delta \mathbf{v}$ for the optimized transfer is very similar to the return for Scenario 1.

5.2.4 TBCS Scenario 3: Side Approach

The previous two scenarios had coplanar initial conditions. Here, a third scenario will be explored where the initial orbit planes are 90° out of plane. Therefore, all of the transfers happen in three dimensions. Fully illustrating the family of possible transfer orbits requires views from multiple angles. Figure 5-11 is a view from "behind" the spacecraft at the start and normal to the Keplerian trajectory that effectively shows the relative altitudes of the various transfer orbits. Figure 5-12 shows the identical scenario from above the north pole, illustrating the relative orbit plane geometry for this particular set of initial conditions and transfer orbits.

Figure 5-13 depicts the global picture of the ultimate path taken by the optimized transfer orbit. Note that the earth is fixed in all three figures, so the continents can be used for orientation.

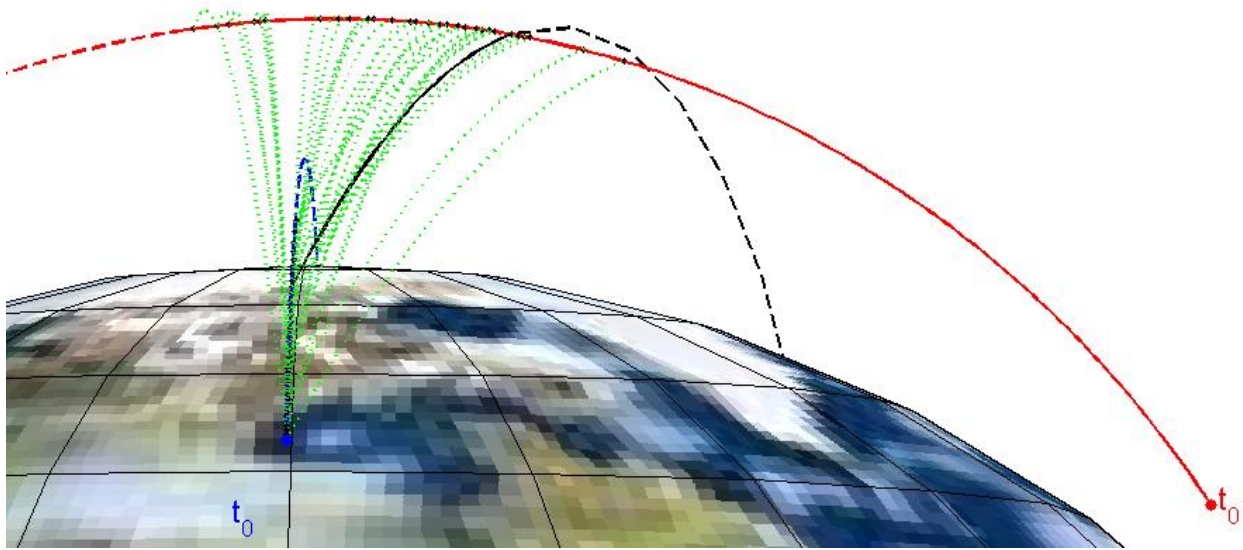


Figure 5-11: TBCS Scenario 3, Transfer Orbit From Behind

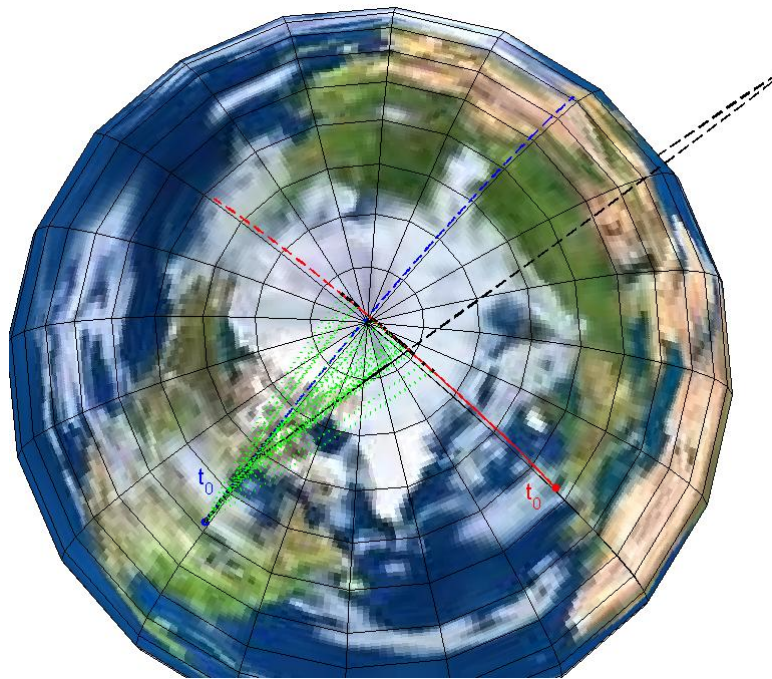


Figure 5-12: TBCS Scenario 3, Transfer Orbit Polar View

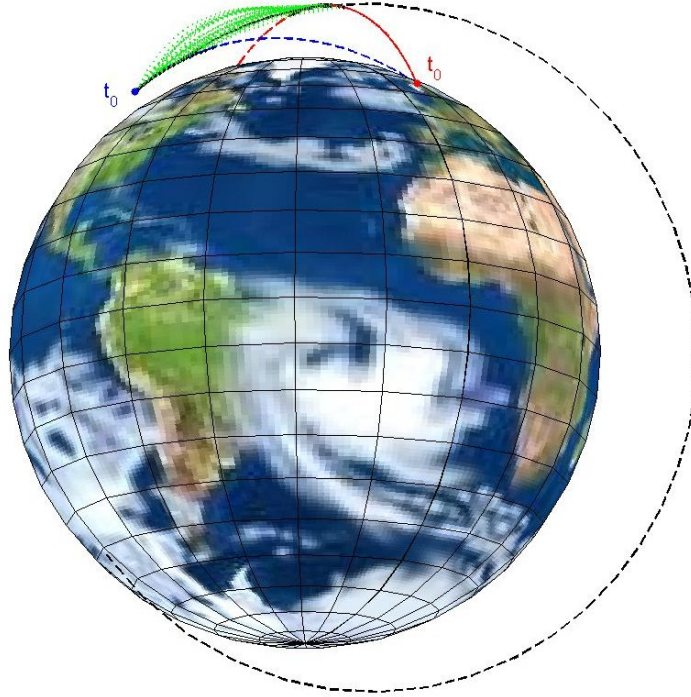


Figure 5-13: TBCS Scenario 3, Transfer Orbit Global View

Property	Minimum	Maximum	Optimized Transfer
Perigee Altitude (km)	-3879	498	-246
Apogee Altitude (km)	1182	11220	2628
Ignition Time (sec)	0	325	190
Rendezvous Time (sec)	580	960	675
Magnitude of ΔV (km/sec)	1.61	3.00	2.50
Relative Velocity (km/sec)	7.49	11.35	10.29
Effective Plane Change ($^{\circ}$)	0.06	18.96	15.65

Table 5.4: TBCS Scenario 3, Optimized Transfer Orbit Properties

In Scenario 3, the normal component Δv_N of the each $\Delta \mathbf{v}$ is typically non-zero for all possible transfer orbits, including that for the optimized transfer orbit. Therefore, plotting the $\Delta \mathbf{v}$ against the contours of perigee leads to a non-intuitive three dimensional plot and thus has been omitted. Table 5.4 does include perigee and $\|\Delta \mathbf{v}_{required}\|$ information. Note that both the range and optimized value for apogee and perigee are similar to the values in Scenario 1 and Scenario 2.

5.3 General Observations on the TBCS Problem

The Trajectory Boundary Condition Selection process described here is a straightforward, brute-force method of finding a transfer orbit that will meet the requirements of the mission. Essentially, it is an optimization problem over the range of possible $t_{ignition}$ and $t_{rendezvous}$ that assumes instantaneous burns and two body motion. Using a hypothetical but plausible cost function, the results of three specific scenarios have been shown. While these are certainly not comprehensive, they demonstrate the process of selecting boundary conditions for a particular problem and create an understanding of how the selection can impact various properties of the transfer orbit.

5.3.1 Considerations on Relative Velocity

Tables 5.2, 5.3, and 5.4 give the range of relative velocities for the three scenarios. It is important to note the large difference in the range of possible relative velocities. In the coplanar head-on scenario, v_{rel} is between 10.9 and 15.7 km/sec. In the coplanar tail-chase scenario, v_{rel} is between 0.3 and 4.2 km/sec. In the 90° out of plane scenario, the range is between 7.5 and 11.4 km/sec.

Clearly, the ultimate value for relative velocity is strongly dictated by the initial conditions. This indicates that no matter what importance v_{rel} is given in a cost function, it is likely that the optimization routine will be unable to exhibit substantial control over the variable in the selected transfer orbit. Thus, placing large constraints on relative velocity is likely to over-constrain the problem.

5.3.2 Considerations on Rendezvous Time

Similar to the impact on rendezvous relative velocity, the actual time of rendezvous may largely be dictated by the initial conditions. For Scenario 1, the earliest possible $t_{rendezvous}$ is 565 seconds after the epoch and there is a range of 285 seconds where rendezvous is possible. For Scenario 2, the earliest possible $t_{rendezvous}$ is 505 seconds and there is a range of 1370 seconds where rendezvous is possible. For Scenario 3, the earliest possible $t_{rendezvous}$ is 580 seconds and there is a range of 380 seconds where rendezvous is possible. The earliest possible $t_{rendezvous}$ is dependent largely on the relative geometry of the initial positions. The range of possible $t_{rendezvous}$ is largely dependent on the relative direction of motion in the spacecraft and Keplerian trajectory orbit planes.

5.3.3 Reentry Characteristics

Perigee is the most important characteristic for determining the reentry characteristics of possible transfer orbits. Apogee also plays an important role for long term reentry characteristics. Tables 5.2, 5.3, and 5.4 indicate that considering all possible transfer orbits, there is a large possible range of perigee and apogee altitudes for each scenario. Contrary to the other two properties discussed above, it may make sense to include reentry dependent characteristics such as apogee and perigee in the cost function.

5.3.4 Summary

The exploration of the trajectory boundary condition selection problem and the author's experience with other initial conditions have led to a few broad conclusions about the ability of various of an optimization to control various properties. Table 5.5 is a subjective summary of ability of an optimization routine to return transfer orbits trajectories that meet certain requirements. Some of the properties are heavily dependent on initial conditions. Other properties are more dependent on which particular transfer is chosen from the family of possible transfer orbits.

The methods and strategies of picking a transfer orbit here are basically modified methods of more traditional spacecraft targeting procedures. Reference [6] offers signif-

Property	Initial Conditions	Transfer Orbit Selected
Perigee Altitude (km)	Low Dependency	High Dependency
Apogee Altitude (km)	Low Dependency	High Dependency
Rendezvous Time (sec)	High Dependency	Medium Dependency
Relative Velocity (km/sec)	High Dependency	Low Dependency

Table 5.5: Impact of Initial Conditions and TBCS on Selected Transfer Properties

icant treatment of targeting and maneuver optimization for the minimum ΔV problem. Compared with this analysis of TBCS, typically much more sophisticated optimization techniques are used to find optimum values. Applying advanced optimization techniques to the TBCS problem may be an avenue of future research. However, simply running Lambert many times and finding a “good” transfer orbit instead of the “global optimum” transfer orbit may be all that the mission calls for. Ultimately the challenging part of the TBCS problem is choosing a cost function that accurately represents the preferences and priorities of a mission’s human decision makers over a wide range of possible initial conditions.

Chapter 6

A New Reference Guidance Solution

The purpose of this chapter is to develop a method of generating a reference trajectory that will place the vehicle near the rendezvous point at the rendezvous time. Using a mix of orbit geometry and new mathematical relationships developed in Chapter 4, a plane of maneuver is calculated that defines the vehicle's attitude profile during the burn and thus the $\Delta \mathbf{v}_{net}$ that is imparted. A baseline GEM Steering maneuver occurring in this plane will be determined using a lookup table on the $\Delta \theta$ for the GEM maneuver. There is a discussion on the major assumption for this method and its potential impact on the error. A slight modification to the algorithm is proposed which achieves a significant increase in accuracy. Lastly, the assumptions made in developing this method are justified.

Section 3.1 described two alternate methods for which baseline GEM maneuvers can be defined. A GEM-CR maneuver was one which assumed a constant angular rate in the plane of maneuver. The GEM-ARC method assumed that the ΔV would be imparted along an arc of a circle, which meant that angular rate in the plane of maneuver was proportional to the acceleration from the engine. The two approaches are different, because in the first, commanded thrust direction is based on time whereas in the second, commanded thrust direction depends on what fraction of the ΔV has been expended. This chapter develops the reference guidance solution based on the GEM-CR method, but a brief discussion of the different considerations for GEM-ARC follows at the end of the chapter.

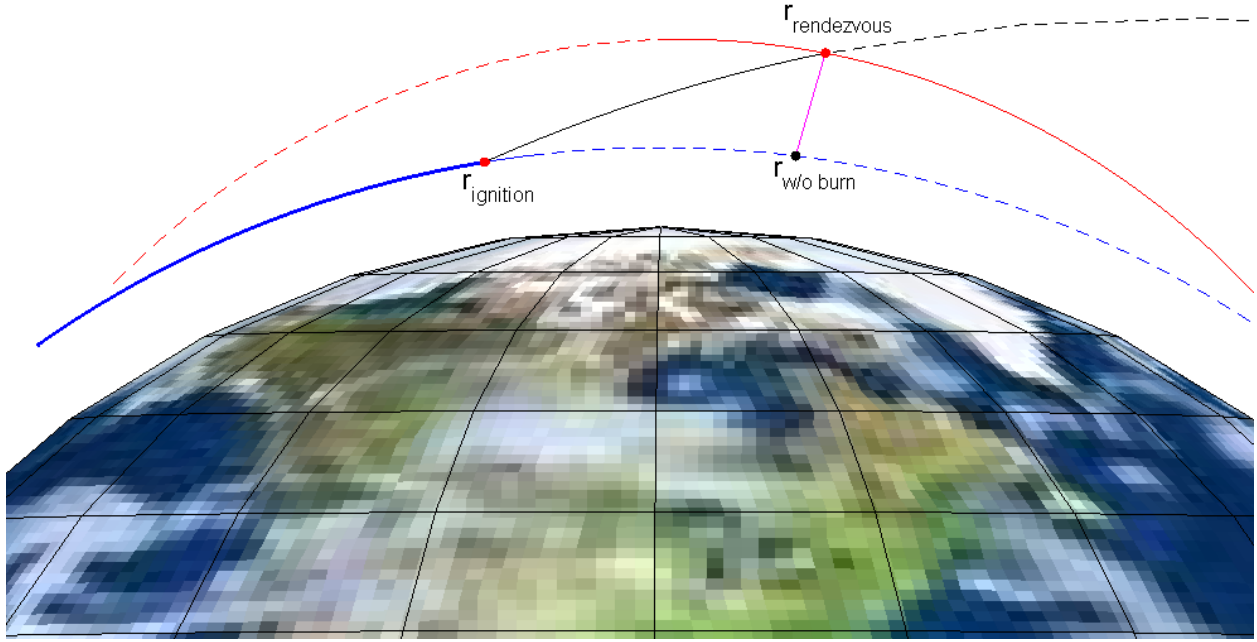


Figure 6-1: Depiction of Parking Orbit Relative to Rendezvous Point

6.1 A New Look at the Orbit Transfer Geometry

Figure 6-1 shows the relative orbit geometry for TBCS Scenario 1. The boundaries of the planned transfer orbit, $\mathbf{r}_{\text{ignition}}$ and $\mathbf{r}_{\text{rendezvous}}$, are clearly shown. In addition, there is another point that is of interest, $\mathbf{r}_{\text{without burn}}$. This point corresponds to the point further along in the spacecraft's parking orbit that the spacecraft would be at the time of rendezvous if no burn were to happen. The blue line is the spacecraft parking orbit and the the black line is the planned transfer orbit that was returned by the TBCS optimization routine.

6.1.1 Position Without Burn

Based on an intuitive understanding of astrodynamics, consider the relative velocities at $\mathbf{r}_{\text{ignition}}$, $\mathbf{r}_{\text{rendezvous}}$, and $\mathbf{r}_{\text{without burn}}$. Since the spacecraft is already at orbital velocity prior to the burn, a substantial amount of the velocity the spacecraft has after the burn

is it already has at the beginning of the burn. As a result, the distance from $\mathbf{r}_{ignition}$ to either $\mathbf{r}_{rendezvous}$ or $\mathbf{r}_{without\ burn}$ is much larger than the distance between $\mathbf{r}_{rendezvous}$ and $\mathbf{r}_{without\ burn}$. This is true for any burn possible with the example spacecraft's ΔV .

It turns out that it is helpful to think of the problem of reaching $\mathbf{r}_{rendezvous}$ at $t_{rendezvous}$ instead as a problem of reaching $\mathbf{r}_{rendezvous}$ from $\mathbf{r}_{without\ burn}$ in the amount of time allowed for the transfer, under no gravitational acceleration, and with no initial velocity. Consider a new vector \mathbf{d} defined below and shown in Figure 6-1 as a magenta line. The magnitude of \mathbf{d} is d .

$$\mathbf{d} = \mathbf{r}_{rendezvous} - \mathbf{r}_{without\ burn} \quad (6.1)$$

$$t_{rendezvous} = t_{ignition} + \Delta t_{transfer} \quad (6.2)$$

$$= t_{ignition} + \Delta t_{total\ burn} + \Delta t_{coast} \quad (6.3)$$

$$= t_{burnout} + \Delta t_{coast} \quad (6.4)$$

$$t_{S2I} = t_{ignition} + \Delta t_{stage\ 1\ burn} + \Delta t_{interstage} \quad (6.5)$$

Equations 6.2 through 6.5 show the relationship between different measures of times in the problem. Note that t_{S2I} refers the time of second stage ignition. Since $\Delta t_{interstage}$ is set to a constant 10 sec for the example spacecraft's reference maneuver and the burn time for each stage is 20 sec, t_{S2I} in the reference maneuver is set to 30 sec after $t_{ignition}$.

6.2 Recasting the Problem in the RPV Frame

In order to solve the problem of closing the distance from $\mathbf{r}_{without\ burn}$ to $\mathbf{r}_{rendezvous}$ in the amount of time $\Delta t_{transfer}$, an easier problem will be addressed. For now, consider a “gravity field-free” rendezvous problem where there is no effect on the vehicle by gravity or

any force other than the vehicle's own propulsion system. In this problem, the rendezvous point is set on the x-axis at distance d from the origin. The vehicle begins at rest and all acceleration is in the x-y plane (so velocity and position remain in this plane as well). The vehicle in this "gravity field-free" example has the same ΔV and thrust profile as the example spacecraft.

6.2.1 Using GEM to Solve a Field-Free Problem

Suppose that if the thrust vector throughout the burn was held constant along the x-axis (pointed at the rendezvous point) and the resulting ΔV caused the vehicle to overshoot rendezvous point. Some kind of energy dissipation maneuver would therefore be required. For this example, suppose that the path that the velocity is imparted in is constrained to a GEM-CR maneuver where the vehicle maintains a constant angular rate in the xy-plane (plane of maneuver) for the length of the burn.

Suppose that $\theta(t)$ is defined as the angle off of the initial thrust vector. Figure 6-2 shows the angle θ and angular rate $\dot{\theta} = \omega$ as a function of time. The angular rate is such that the vehicle will have a $\Delta\theta = 90^\circ$ change of thrust direction during the burn. *This value for $\Delta\theta$ is simply for use as an example in understanding the method.*

Figure 6-3 depicts how the velocity and position change during the course of the burn. Given the constant angular rate ω and the vehicle's thrust profile from Appendix A, the velocity follows those curves. Let δv and δr denote the change in velocity and position during the course of the 50 sec burn.

As an example, suppose that Δt_{coast} is 120 sec. Figure 6-4 shows the position during the 50 sec burn and the following 120 coast period. After the 170 sec maneuver, the vehicle has reached $\mathbf{r}(t_{rendezvous})$. Suppose the desired final position for this maneuver is on the x-axis. Then by rotating initial and final thrust vectors by a carefully selected angle γ , it is possible to have the final position $\mathbf{r}(t_{rendezvous})$ fall on the x-axis. Equation 6.6 gives the angle γ that can rotate the entire maneuver that is shown in Figure 6-3 to one that results in a final position on the x-axis.

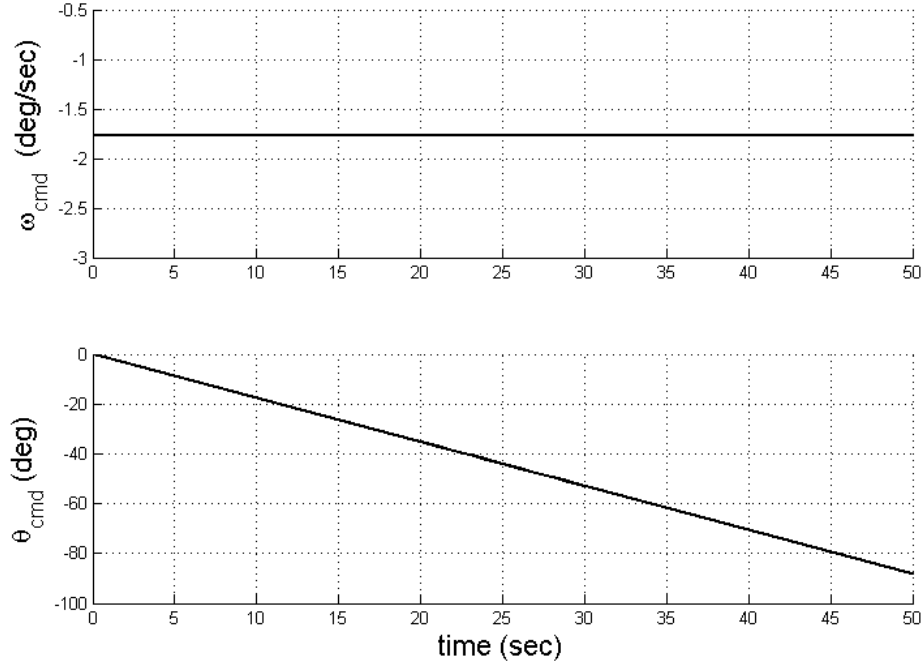


Figure 6-2: Angular Rate and Angles for GEM-CR Maneuver with $\Delta\theta = 90^\circ$

$$\gamma = \arctan \left(\frac{r_y(t_{rendezvous})}{r_x(t_{rendezvous})} \right) \quad (6.6)$$

Given the GEM-CR $\Delta\theta$, the Δt_{coast} , and γ , Equations 6.7 and 6.8 can be used to find the initial and final unit vector thrusting directions for the burn. At first stage ignition, the vehicle should be thrusting (or pointing) in the direction of $\hat{\mathbf{i}}_{initial}^{RPV}$ while at burnout of the second stage the vehicle should be thrusting along the vector $\hat{\mathbf{i}}_{final}^{RPV}$. The angular rate of change during the burn, equal to ω , is constant for this reference condition.

$$\hat{\mathbf{i}}_{initial}^{RPV} = \begin{bmatrix} \cos \gamma & \sin \gamma & 0 \\ -\sin \gamma & \cos \gamma & 0 \\ 0 & 0 & 1 \end{bmatrix} \cdot \begin{bmatrix} 1 \\ 0 \\ 0 \end{bmatrix} = \begin{bmatrix} \cos \gamma \\ -\sin \gamma \\ 0 \end{bmatrix} \quad (6.7)$$

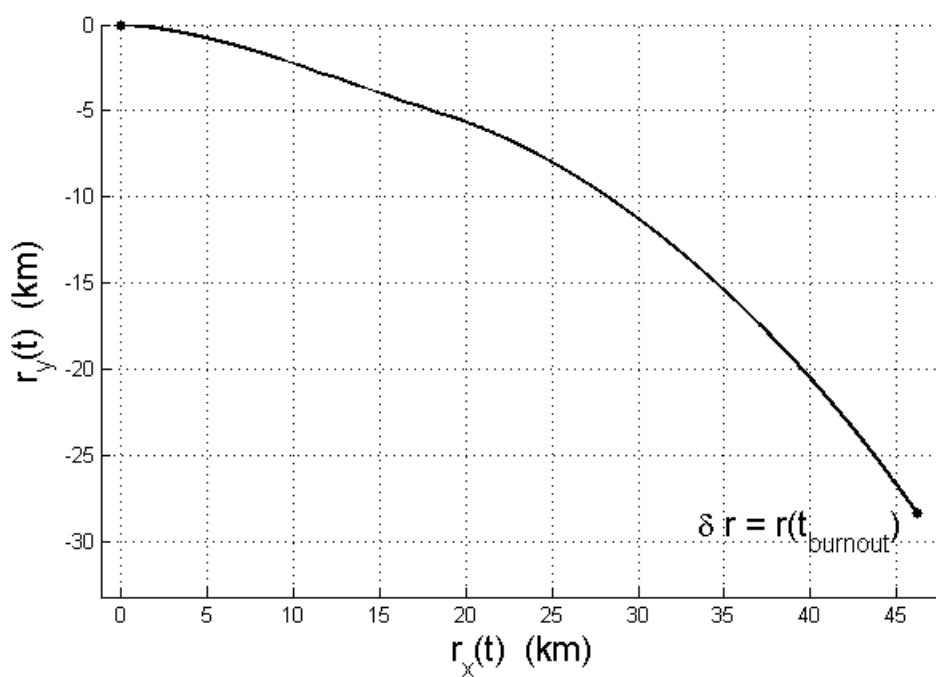
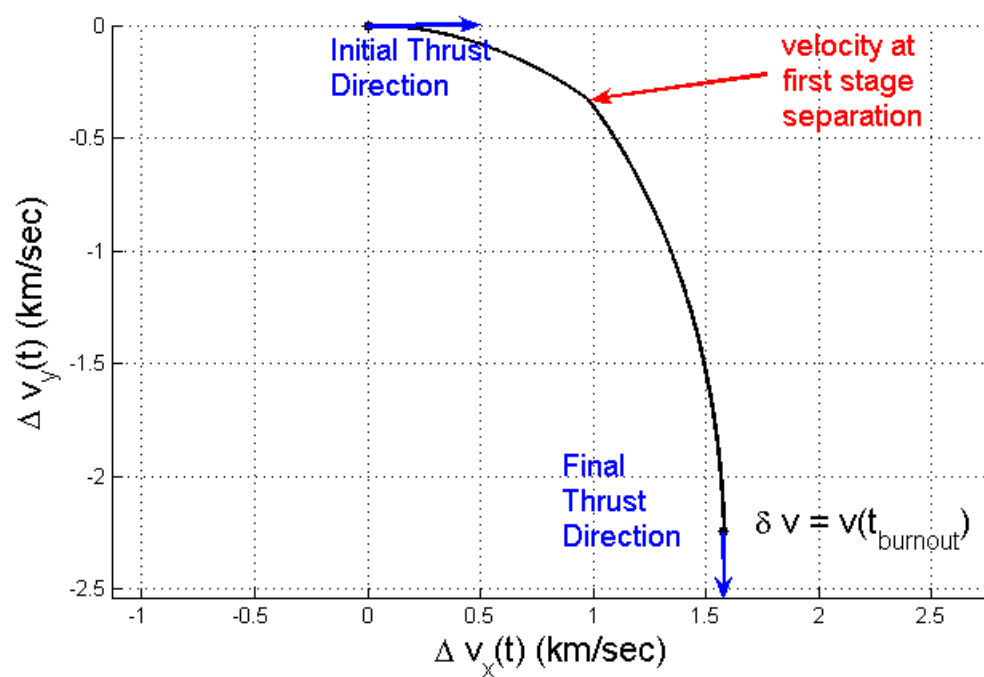


Figure 6-3: Position and Velocity for GEM-CR Maneuver with $\Delta\theta = 90^\circ$

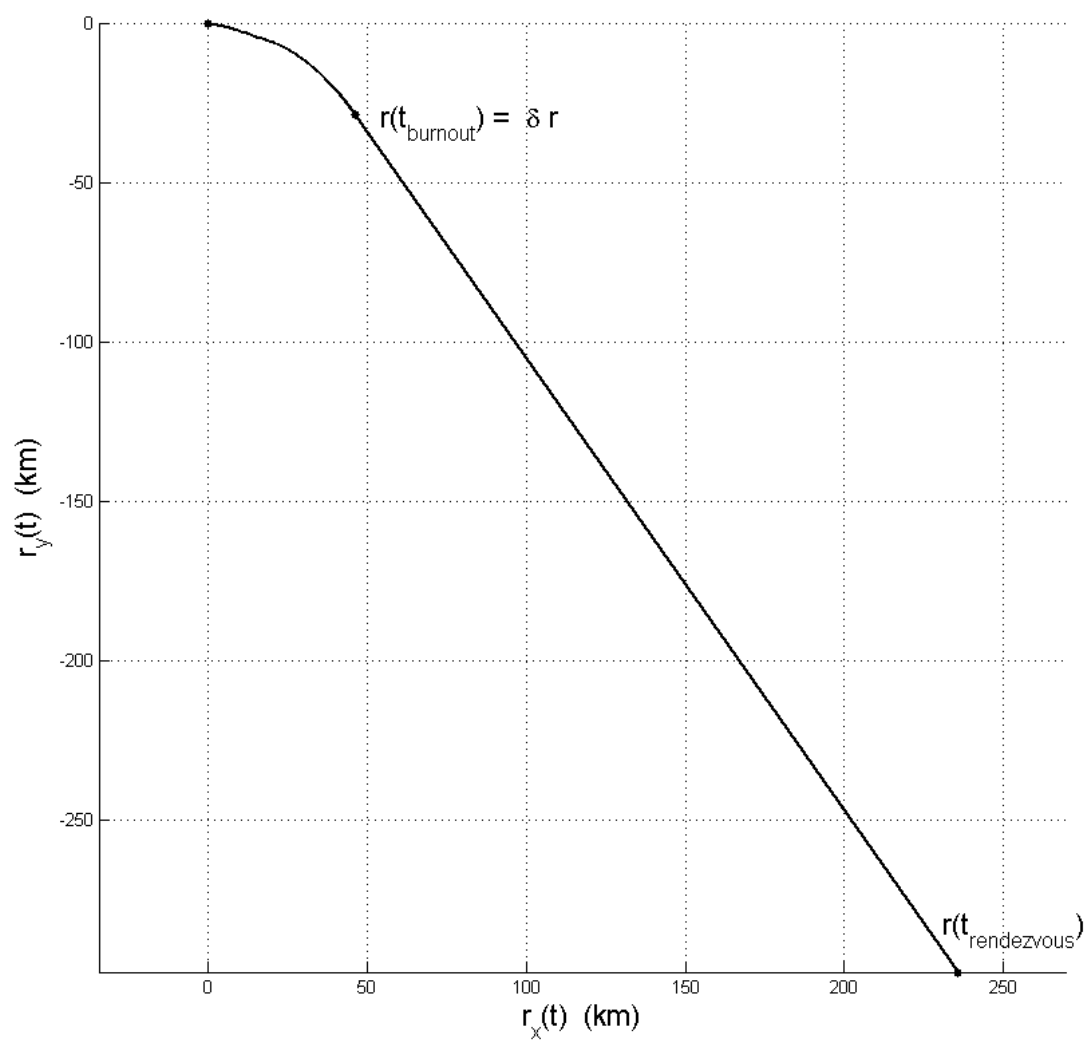


Figure 6-4: Position during GEM-CR Maneuver and 120 sec Coast

$$\begin{aligned}
\hat{\mathbf{i}}_{final}^{RPV} &= \begin{bmatrix} \cos \gamma & \sin \gamma & 0 \\ -\sin \gamma & \cos \gamma & 0 \\ 0 & 0 & 1 \end{bmatrix} \cdot \begin{bmatrix} \cos \Delta\theta \\ -\sin \Delta\theta \\ 0 \end{bmatrix} \\
&= \begin{bmatrix} \cos \gamma \cos \Delta\theta - \sin \gamma \sin \Delta\theta \\ -\sin \gamma \cos \Delta\theta - \cos \gamma \sin \Delta\theta \\ 0 \end{bmatrix} \tag{6.8}
\end{aligned}$$

Figure 6-5 shows a maneuver with the thrusting directions given by $\hat{\mathbf{i}}_{initial}^{RPV}$ and $\hat{\mathbf{i}}_{final}^{RPV}$. For the simple gravity field-free problem, if the desired point of rendezvous was equal to $\mathbf{r}^{RPV}(t_{rendezvous})$, then the assumed $\Delta\theta$ would solve the problem. A maneuver that reaches a rendezvous point on the x-axis at length d from the origin depends only on the following things:

- A given $\Delta\theta$ (or ω where $\Delta\theta = \omega \cdot \Delta t_{total \ burn}$).
- The assumption of $\Delta t_{interstage} = 10sec$
- The assumed acceleration profile

6.2.2 Using a GEM-CR Table to find $\Delta\theta$

For the sample problem above, a $\Delta\theta$ was assumed and d was determined. Suppose instead that d is given and $\Delta\theta$ must be found. To solve the problem, two lookup tables will be used. The independent variable in the lookup tables is $\Delta\theta$. The dependent variables in the lookup tables are the vector quantities $\delta\mathbf{r}$ and $\delta\mathbf{v}$. Once Δt_{coast} is known, then the d_{table} corresponding to each $\Delta\theta$ can be calculated using 6.9. The purpose of the lookup table method is to find $\Delta\theta$ such that $d_{table}(\Delta\theta) = d$.

$$d_{table}(\Delta\theta) = \|\delta\mathbf{r} + \delta\mathbf{v} \cdot \Delta t_{coast}\| \tag{6.9}$$

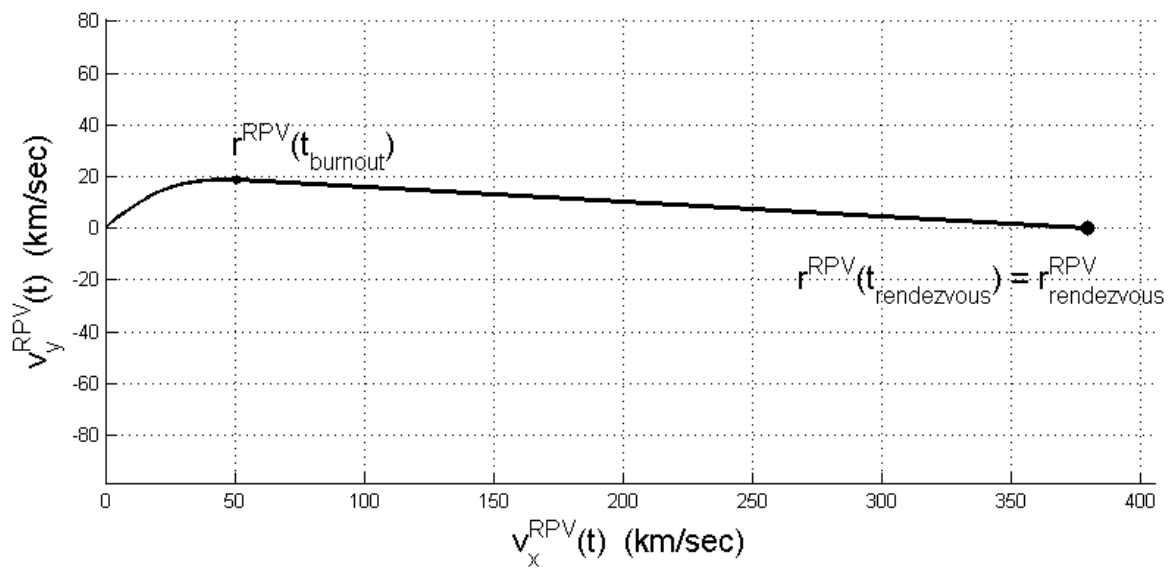
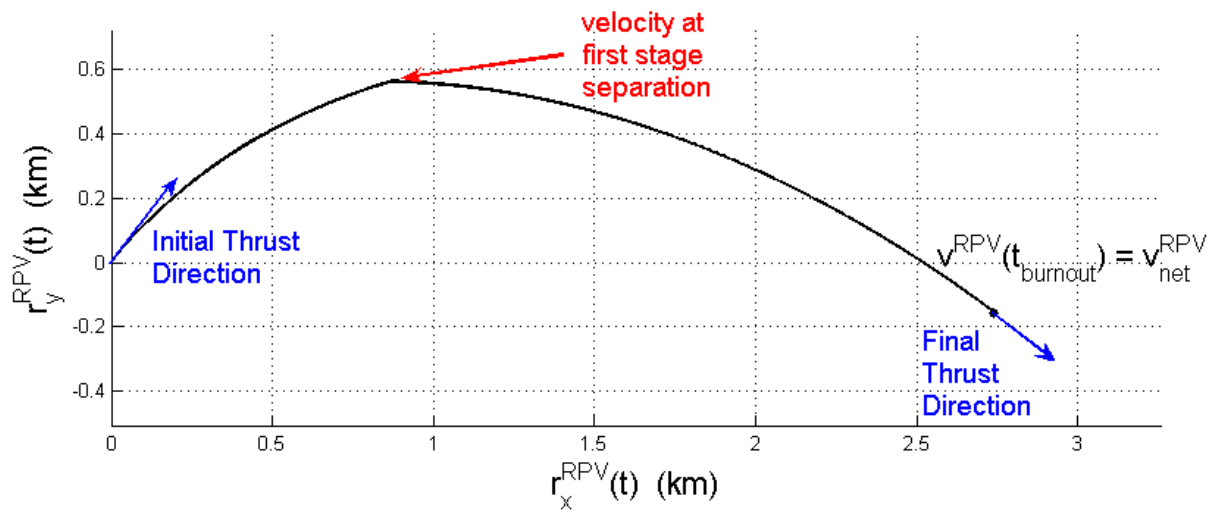


Figure 6-5: Position and Velocity, GEM-CR Maneuver and Coast in the RPV Frame

Once $\Delta\theta$ is known, then γ can be found using Equation 6.6. Finally, $\hat{\mathbf{i}}_{initial}^{RPV}$ and $\hat{\mathbf{i}}_{final}^{RPV}$ can be determined using Equations 6.7 and 6.8.

Setting up the GEM-CR Lookup Table

The GEM table can be created by running many simple nonlinear simulations. Given each independent variable $\Delta\theta$, the corresponding dependant variables $\delta\mathbf{r}$ and $\delta\mathbf{v}$ can be found by running the nonlinear simulation defined by Equation 6.10.

$$\left\{ \begin{array}{lcl} \omega & = & \frac{-\Delta\theta}{t_{total \ burn}} \\ \theta(t) & = & \omega t \\ \hat{\mathbf{i}}(t) & = & \begin{bmatrix} \cos \theta(t) \\ -\sin \theta(t) \\ 0 \end{bmatrix} \\ \mathbf{a}_{thrust}(t) & = & \frac{F_{thrust}(t)}{m(t)} \cdot \hat{\mathbf{i}}(t) \\ \delta\mathbf{v} & = & \int_{t_{ignition}}^{t_{burnout}} \mathbf{a}_{thrust}(t) dt \\ \delta\mathbf{r} & = & \int \int_{t_{ignition}}^{t_{burnout}} \mathbf{a}_{thrust}(t) dt \ dt \end{array} \right. \quad (6.10)$$

Since this creates two simple one-dimensional lookup tables (for both $\delta\mathbf{r}$ and $\delta\mathbf{v}$), it may be possible to run the calculations on board without use of the lookup table. The lookup table has been included because it may be desirable to add independent variables in an actual implementation. Another variation could involve defining additional GEM maneuver parameters to create a lookup table with two or three independent variables.

6.3 Relating the RPV Frame back to the ECI Frame

A relatively simple rendezvous problem has been set up and solved in the RPV frame. The solution defines the planned attitude profile during the course of the burn defined by $\hat{\mathbf{i}}_{initial}^{RPV}$, $\hat{\mathbf{i}}_{final}^{RPV}$, and the assumption that the angular rate in the plane of maneuver is constant. The solution found in the RPV plane can now be transformed into the ECI frame.

First, consider the problem of getting a spacecraft from $\mathbf{r}_{without\ burn}$ to $\mathbf{r}_{rendezvous}$. The direction of travel would be along the vector \mathbf{d} . Therefore, the x-axis of RPV should be lined up with the vector \mathbf{d}^{ECI} .

$$\hat{\mathbf{i}}_{x_{RPV}}^{ECI} = \frac{\mathbf{d}}{d} = \frac{\mathbf{r}_{rendezvous} - \mathbf{r}_{without\ burn}}{\|\mathbf{r}_{rendezvous} - \mathbf{r}_{without\ burn}\|} \quad (6.11)$$

6.3.1 Minimizing First Stage Perigee

Now comes the question of where the y-axis and z-axis of RPV frame are aligned in the ECI frame. It turns out that Chapter 4 holds the answer. Notice in the velocity profile shown Figure 6-5 that the acquired velocity in the y-axis at first stage burnout (and separation) $\mathbf{v}_y(t_{first\ stage\ burnout}) > 0$. If the lookup table is created according to Equation 6.10, then this is always true unless $\mathbf{v}_y(t_{first\ stage\ burnout}) = \Delta\theta = 0$ and the burn is inertially fixed.

Now consider the velocity profile of Figure 6-5 overlaid on Figure 4-5, where the x-axis of the RPV frame is aligned with the $\Delta\mathbf{v}_{net}$. It is clear that the rotation around $\hat{\mathbf{i}}_{x_{RPV}}^{ECI}$ is important because that has direct impact on the resulting first stage perigee and thus its reentry characteristics. By using the gradient of perigee from Chapter 4, $\hat{\mathbf{i}}_{y_{RPV}}^{ECI}$ can be placed in the direction perpendicular to $\hat{\mathbf{i}}_{x_{RPV}}^{ECI}$ with the most rapidly decreasing perigee. In order to calculate the gradient, it is necessary to determine approximately where first stage separation will occur in the ΔV plane. The $\Delta\mathbf{v}_{MPFSS}$ is an “average” value for all possible maneuvers resulting in a given $\Delta\mathbf{v}_{net}$ based on the proportion of $\Delta\mathbf{v}_{net}$ that is imparted by the first stage and is given in Equation 6.12.

$$\Delta \mathbf{v}_{MPFSS} = \left(\frac{\Delta V_{first\ stage}}{\Delta V_{first\ stage} + \Delta V_{second\ stage}} \right) \Delta \mathbf{v}_{net} \quad (6.12)$$

$$\approx \left(\frac{1}{3} \right) \Delta \mathbf{v}_{net} \text{ for the example spacecraft} \quad (6.13)$$

A precise value for $\Delta \mathbf{v}_{net}$ is not necessary. In this case, the value $\Delta \mathbf{v}_{net}^{ECI}$ that was calculated during TBCS optimization is sufficient. The next step is to find the gradient of perigee of $\Delta \mathbf{v}_{MPFSS}$ using Equation 4.28. In order to minimize first stage perigee, $\hat{\mathbf{i}}_{yRPV}^{ECI}$ should be the component of $\nabla r_p(\Delta \mathbf{v}_{MPFSS})^{ECI}$ which is perpendicular to $\hat{\mathbf{i}}_{xRPV}^{ECI}$. This can be used to find $\mathbf{T}_{ECI2RPV}$ using Equations 6.14, 6.15, 6.16, and 6.17.

$$\Delta \mathbf{v}_{MPFSS}^{RTN} = \mathbf{T}_{ECI2RTN} \cdot \Delta \mathbf{v}_{MPFSS}^{ECI} \quad (6.14)$$

$$\nabla r_p^{RTN} = \nabla r_p(\Delta \mathbf{v}_{MPFSS}^{RTN}) \text{ using Equation 4.28} \quad (6.15)$$

$$\nabla r_p^{ECI} = \mathbf{T}_{ECI2RTN}^T \cdot \nabla r_p^{RTN} \quad (6.16)$$

$$\mathbf{T}_{RPV2ECI} = \begin{bmatrix} \frac{\mathbf{d}}{d} & \frac{(\mathbf{d} \times \nabla r_p) \times \mathbf{d}}{\|(\mathbf{d} \times \nabla r_p) \times \mathbf{d}\|} & \frac{\mathbf{d} \times \nabla r_p}{\|\mathbf{d} \times \nabla r_p\|} \end{bmatrix} \quad (6.17)$$

6.3.2 Algorithm for the Reference Guidance Solution

All of the steps involved in calculating the reference guidance solution has been collected and listed in numerical order below.

1. Inputs: $\mathbf{r}^{ECI}(t_{ignition})$, $\mathbf{v}^{ECI}(t_{ignition})$, $\mathbf{r}_{rendezvous}$, $t_{rendezvous}$.
2. Find Transition Matrix $\mathbf{T}_{ECI2RTN}$.
3. Propagate the spacecraft forward by $\Delta t_{transfer}$ to determine $\mathbf{r}_{without\ burn}$.

4. Find d with either the vector from $\mathbf{r}_{without\ burn}$ to $\mathbf{r}_{rendezvous}$ or that defined by Equation 6.18.
5. Use d to find the solution GEM maneuver in the RPV frame defined by $\Delta\theta$.
6. Find γ , $\hat{\mathbf{i}}_{initial}^{RPV}$, and $\hat{\mathbf{i}}_{final}^{RPV}$
7. Determine the velocity for the mean point of first stage separation $\Delta\mathbf{v}_{MPFSS}^{ECI} = 0.33\Delta\mathbf{v}_{net}^{ECI}$
8. Transform the $\Delta\mathbf{v}_{MPFSS}^{ECI}$ into the RTN frame.
9. Find the Gradient of Perigee $\nabla r_p(\Delta\mathbf{v}_{MPFSS}^{RTN})$
10. Transform the gradient of perigee into the ECI frame.
11. Using the gradient of perigee, determine $\mathbf{T}_{RPV2ECI}$
12. Transform $\hat{\mathbf{i}}_{initial}$ and $\hat{\mathbf{i}}_{final}$ into the ECI frame.
13. Outputs: reference guidance solution defined by $\hat{\mathbf{i}}_{initial}$ and $\hat{\mathbf{i}}_{final}$.

6.3.3 Implementation using GEM-ARC

Implementing GEM-ARC is very similar to the GEM-CR solution that has been just described. There is one crucial difference. Using a GEM-ARC method means that $\hat{\mathbf{i}}_{final}$ is the pointing direction defined at the expected value of $t_{burnout}$ and $\hat{\mathbf{i}}_{thrust}(t)$ depends on time. Rather, the pointing direction $\hat{\mathbf{i}}_{thrust}(t)$ depends on the fraction of the total ΔV that has been delivered. Therefore, $\hat{\mathbf{i}}_{final}$ is defined as the pointing direction when the expected value of ΔV has been delivered.

6.3.4 The Major Assumption

In developing this new modified method using the RPV frame, the “gravity field-free” analysis, and $\mathbf{r}_{without\ burn}$, one key assumption has been made. That is that the net effect

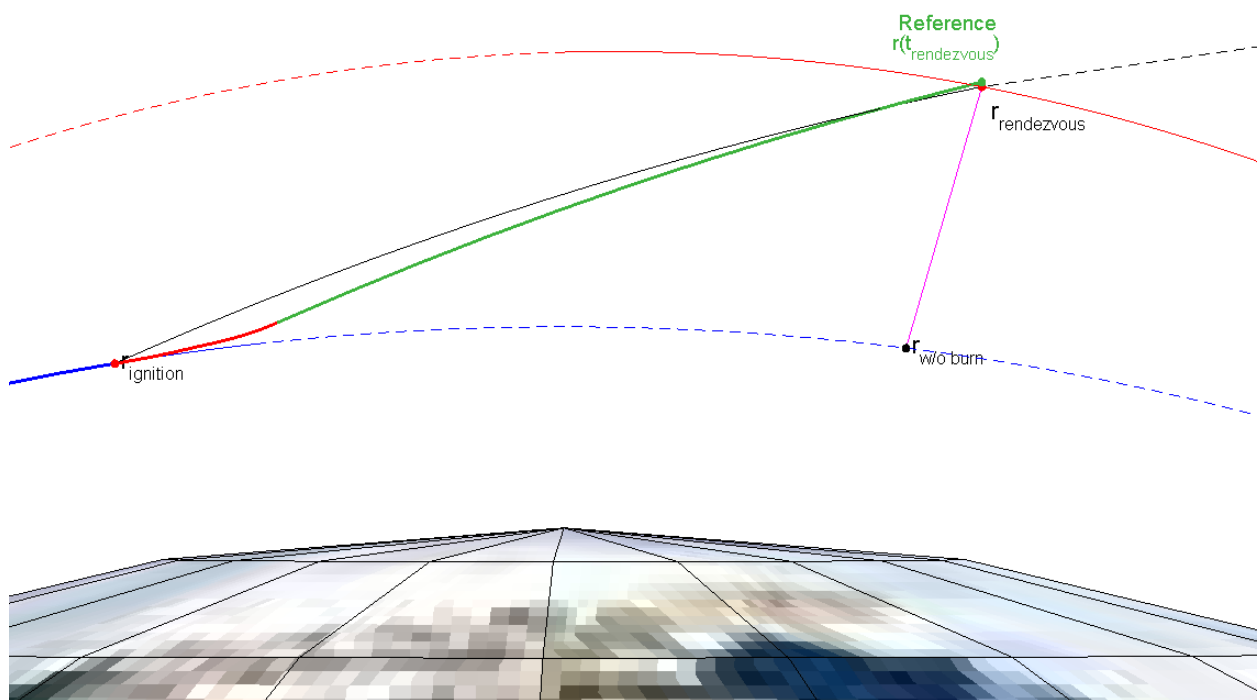


Figure 6-6: Accuracy of the Reference Trajectory, Scenario 1

of gravity is the same along the transfer orbit from $\mathbf{r}_{\text{ignition}}$ to $\mathbf{r}_{\text{rendezvous}}$ as it is along the original parking orbit trajectory from $\mathbf{r}_{\text{ignition}}$ to $\mathbf{r}_{\text{without burn}}$.

As given in Equation 2.2, acceleration due to gravity lies toward the center of the earth and is inversely proportional to the distance from the spacecraft to the center of the earth. This means that if $\mathbf{r}_{\text{rendezvous}}$ is at significantly higher altitude than $\mathbf{r}_{\text{without burn}}$, as in Scenario 1, the reference trajectory will cause the spacecraft to arrive slightly higher than the intended $\mathbf{r}_{\text{rendezvous}}$. This happens because of the net acceleration from gravity is less along the transfer orbit than along the lower-altitude parking orbit. Figure 6-6 clearly illustrates this, with the black trajectory being the transfer returned by TBCS and the green trajectory being the reference trajectory that the spacecraft follows given the attitude profile during the burn defined by $\hat{\mathbf{i}}_{\text{initial}}$ and $\hat{\mathbf{i}}_{\text{final}}$. The expected error resulting from this assumption is 10.695 km for Scenario 1, much of it in the local vertical direction.

Another type of error also caused by differential gravity occurs when there is a significant plane change in the maneuver. This occurs because when there is a large plane change, the net effect of gravity is in a different direction. The assumption will cause the reference guidance solution (through $\hat{\mathbf{i}}_{\text{initial}}$ and $\hat{\mathbf{i}}_{\text{final}}$) to prescribe less of a plane change than is actually required.

Longer transfer times will magnify the error resulting from the “field free” assumption simply because gravity has a longer amount of time to act. This results because the vector \mathbf{d} begins to deviate from the instantaneous Lambert solution while the burn time begins to look very small relative to the total transfer time. Essentially, this is because the net difference in gravity between the actual trajectory and the continued parking orbit greatly increases with a longer transfer time.

6.4 A Modification to \mathbf{d} to Improve Performance

In this section, a modification to the variable \mathbf{d} will be made in order to make significant improvements to the accuracy of the reference guidance solution. This new \mathbf{d} will be used in the algorithm found in Section 6.3.2.

Results	\mathbf{d} based on $\mathbf{r}_{without\ burn}$	\mathbf{d} based on $\Delta\mathbf{v}_{instantaneous}$
Scen. 1 Opt. Trans.	10.695 km	5.580 km
Scen. 2 Opt. Trans.	9.333 km	4.779 km
Scen. 3 Opt. Trans.	65.406 km	29.421 km

Table 6.1: Performance Comparison for the Two Definitions of \mathbf{d}

Recall that \mathbf{d} forms the x-axis of the RPV frame and d is the distance from the origin to $\mathbf{r}_{rendezvous}$ in the RPV frame. Consider a new definition of \mathbf{d} that uses the instantaneous Lambert solution, given in Equation 6.18.

$$\mathbf{d} = \Delta\mathbf{v}_{instantaneous} \cdot \Delta t_{transfer} \quad (6.18)$$

It has been shown that if \mathbf{d} is defined using Equation 6.18, the accuracy is better than if using $\mathbf{r}_{without\ burn}$ to calculate \mathbf{d} . Consider Figure 6-5. Suppose now that the x-axis of the RPV frame was aligned with the new definition of \mathbf{d} and $\mathbf{r}_{rendezvous}$ was distance d from the origin. If the vehicle was capable of an instantaneous change in velocity along the x-axis (corresponding to $\Delta\mathbf{v}_{instantaneous}$), it would arrive to $\mathbf{r}_{rendezvous}$ at time $\Delta t_{transfer}$ and follow the black trajectory in Figure 6-6. Instead, the new definition of \mathbf{d} will be used in finding $\Delta\theta$ from the lookup table and in calculating $\mathbf{T}_{RPV2ECI}$ in Equation 6.17.

For very short transfer times, the two different \mathbf{d} vectors are identical, but accuracy improves with the new formulation as time increases. This happens because the Lambert $\Delta\mathbf{v}_{instantaneous}$ solution already compensates for the differential gravity. Recall that the position error from a given problem results from the net difference in total gravitational acceleration. Refer to Figure 6-6. For the original method of calculating \mathbf{d} , the error arises from the difference between the actual trajectory (in green) and the parking orbit trajectory (in blue). For the new method of calculating \mathbf{d} , the error results from the gravitational difference in between the actual trajectory (in green) and the Lambert instantaneous trajectory (in black). Table 6.1 summarizes the differences between the old and new methods of calculating \mathbf{d} for the three optimized transfers from TBCS.

It is evident from Table 6.1 that Scenario 3 has a larger error than the other two results. It should be noted that this is largely a result from the fact that Scenario 3 has a longer transfer time, which means that the error from differential gravity accumulates

for a longer period of time. It is not caused by the fact the Scenario 3 is the only scenario with an out of plane transfer.

6.5 Justification for the Reference Guidance Solution

While the method to find a reference trajectory is approximate and results in an imperfect solution, its use is justified because the error is relatively small and the closed loop method of linear perturbations is capable of correcting for it. As a result of the inherent flexibility in $\Delta \mathbf{v}$ built in to the TBCS optimization routine, minor modifications can be made to the reference guidance solution \mathbf{c} to drive the expected error down to throughout the burn. The next chapter will describe how the method of linear perturbations on a reference trajectory can be used in this problem.

[This page intentionally left blank.]

Chapter 7

Application of Linear Perturbation Methods

At this point, there is a reference guidance solution defined $\hat{\mathbf{i}}_{initial}$, $\hat{\mathbf{i}}_{final}$, and a few assumptions about the burn (GEM-ARC or GEM-CR, fixed interstage time, etc). By running this reference guidance solution in a nonlinear simulation, the expected position error \mathbf{e} at $t_{rendezvous}$ can be determined. It is assumed that small modifications to the reference guidance solution will enable the spacecraft to reach $\mathbf{r}_{rendezvous}$ and drive the \mathbf{e} toward zero. The purpose of this chapter is to determine what those control input modifications should be.

First, a couple control variables will be introduced that allow the ΔV path to vary from the GEM-CR or GEM-ARC assumptions. With these new control variables, the reference guidance solution will be improved using the method of linear perturbations outlined in Section 3.2. Finally, the closed loop algorithm is outlined.

7.1 Introducing Control Variables on the GEM Maneuver

To employ the method of linear perturbations, it is necessary to define control variables that can be adjusted at each step to refine the solution and minimize the expected error.

While many more control variables are available, this thesis will employ between three and six difference control variables, depending on the phase of flight.

7.1.1 Perturbations on Unit Vector Direction

It is important to exploit all degrees of freedom available in the unit vectors $\hat{\mathbf{i}}_{initial}$ and $\hat{\mathbf{i}}_{final}$. To effectively employ the method of linear perturbations upon a reference trajectory, there must be a method available to perturb a unit vector $\hat{\mathbf{i}}$. Recall from Chapter 2 that unit vectors have two degrees of freedom. Suppose that a plane of maneuver has been defined by a vector normal to it, $\hat{\mathbf{i}}_{normal}$. Then, $\hat{\mathbf{i}}$ can be perturbed by a small angle $\delta\theta$ that lies in that plane of maneuver and by another small angle $\delta\psi$ that is normal to the plane of maneuver.

Equations 7.2 through 7.5 create an algorithm used to perturb a unit vector direction. It was developed using the standard definitions of single-axis rotation matrices. Every time that the method of linear perturbations is used on either $\hat{\mathbf{i}}_{initial}$ or $\hat{\mathbf{i}}_{final}$, it will require a call to a function that basically finds the perturbed vector from $\hat{\mathbf{i}}$, $\hat{\mathbf{i}}_{normal}$, $\delta\theta$, and $\delta\psi$. Note that the plane of maneuver vector $\hat{\mathbf{i}}_{normal}$ can always be found with a cross product of the current (or initial) and final unit vector thrust directions from the guidance solution, as in Equation 7.1.

$$\hat{\mathbf{i}}_{normal} = \hat{\mathbf{i}}_{current} \times \hat{\mathbf{i}}_{final} \quad (7.1)$$

$$\mathbf{T}_a = \begin{bmatrix} \cos(\delta\theta) & \sin(\delta\theta) & 0 \\ -\sin(\delta\theta) & \cos(\delta\theta) & 0 \\ 0 & 0 & 1 \end{bmatrix} \quad (7.2)$$

$$\mathbf{T}_b = \begin{bmatrix} \cos(\delta\psi) & 0 & -\sin(\delta\psi) \\ 0 & 1 & 0 \\ \sin(\delta\psi) & 0 & \cos(\delta\psi) \end{bmatrix} \quad (7.3)$$

$$\mathbf{T}_c = \begin{bmatrix} \frac{\hat{\mathbf{i}}}{\|\hat{\mathbf{i}}\|} & \frac{\hat{\mathbf{i}}_{normal} \times \hat{\mathbf{i}}}{\|\hat{\mathbf{i}}_{normal} \times \hat{\mathbf{i}}\|} & \frac{\hat{\mathbf{i}}_{normal}}{\|\hat{\mathbf{i}}_{normal}\|} \end{bmatrix} \quad (7.4)$$

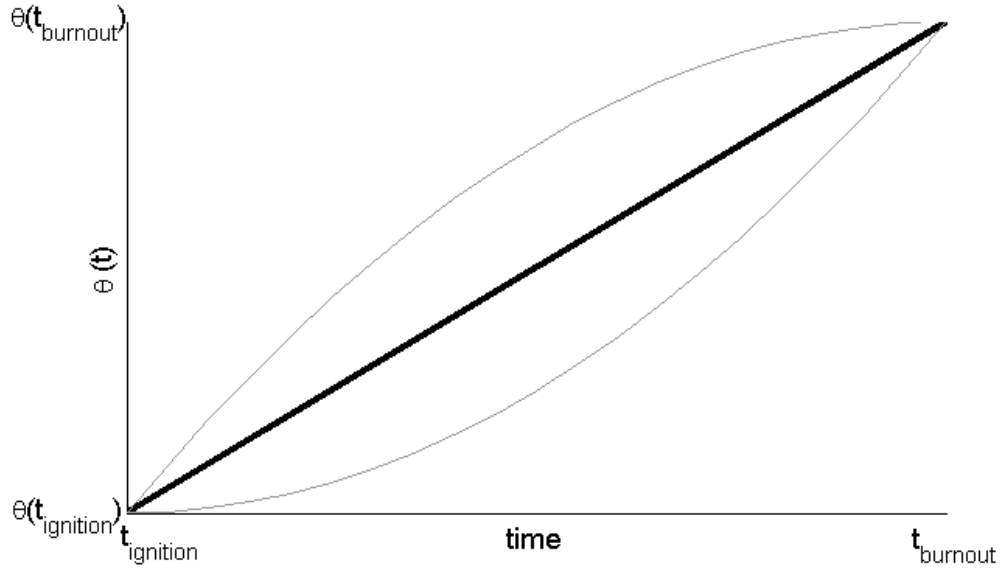


Figure 7-1: Theta in the GEM-CR Reference Maneuver

$$\hat{\mathbf{i}}_{perturbed} = \mathbf{T}_c \cdot \mathbf{T}_b \cdot \mathbf{T}_a \cdot \begin{bmatrix} 1 \\ 0 \\ 0 \end{bmatrix} \quad (7.5)$$

At every step in the guidance algorithm, two perturbations of the vector $\hat{\mathbf{i}}_{final}$ will be run using Equations 7.1, 7.2, 7.3, 7.4, and 7.5.

7.1.2 Perturbation on the GEM Maneuver Assumptions

The objective of this section is to add degrees of freedom to the problem by dropping assumptions that were used to create the reference trajectory. In developing the reference trajectory and using GEM, assumptions were made about the path in the ΔV plane. If $\theta(t)$ corresponds to the change in direction in the plane of maneuver, GEM-CR assumes that it is linearly related to time while GEM-ARC assumes that it is linearly related to the proportional of expended ΔV . These assumed relationships are depicted in Figures 7-1 and 7-2 as the solid black line.

Suppose for an instance that this linearity assumption was dropped. Instead of having a linear relationship, $\theta(t)$ could depend on time (or proportion of ΔV used) by any func-

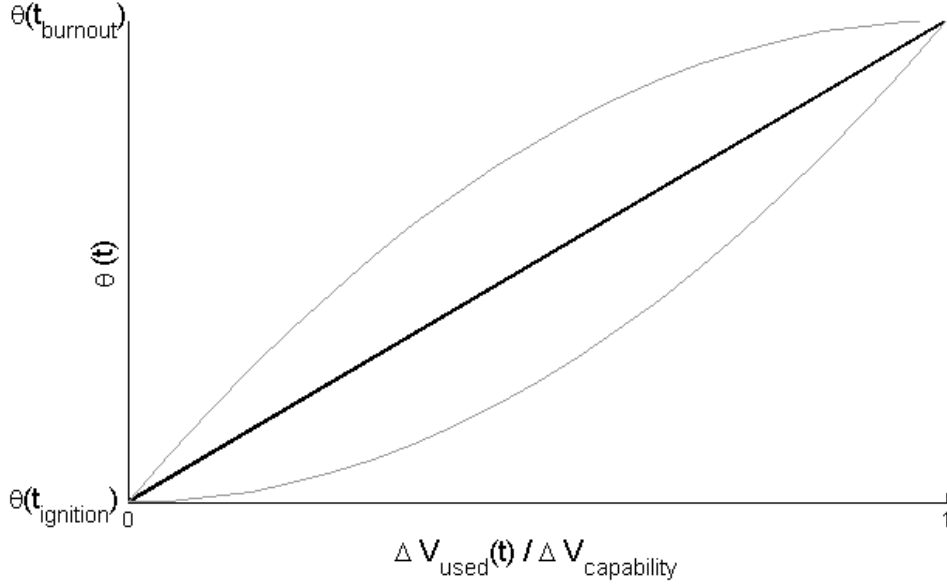


Figure 7-2: Theta in the GEM-ARC Reference Maneuver

tion. For instance, it could follow additional paths denoted by the gray lines in Figures 7-1 and 7-2. Equations 7.6 and 7.7 use a vector \mathbf{k} to define $\theta(t)$ using a Taylor series expansion.

$$\frac{\theta_{GEM-CR}(t)}{\Delta\theta} = k_1 \left(\frac{t}{T} \right) + k_2 \left(\frac{t}{T} \right)^2 + k_3 \left(\frac{t}{T} \right)^3 + \dots \quad (7.6)$$

$$\frac{\theta_{GEM-ARC}(t)}{\Delta\theta} = k_1 \left(\frac{\Delta V_{used}(t)}{\Delta V_{capability}} \right) + k_2 \left(\frac{\Delta V_{used}(t)}{\Delta V_{capability}} \right)^2 + k_3 \left(\frac{\Delta V_{used}(t)}{\Delta V_{capability}} \right)^3 + \dots \quad (7.7)$$

$$\text{where } \mathbf{k} = [k_1 \ k_2 \ k_3 \ \dots]^T \text{ and } \|\mathbf{k}\| = 1$$

While higher order terms could be easily implemented, this thesis will consider only the linear and quadratic term. Since there is a constraint $k_1 + k_2 = 1$, this provides one additional degree of freedom.

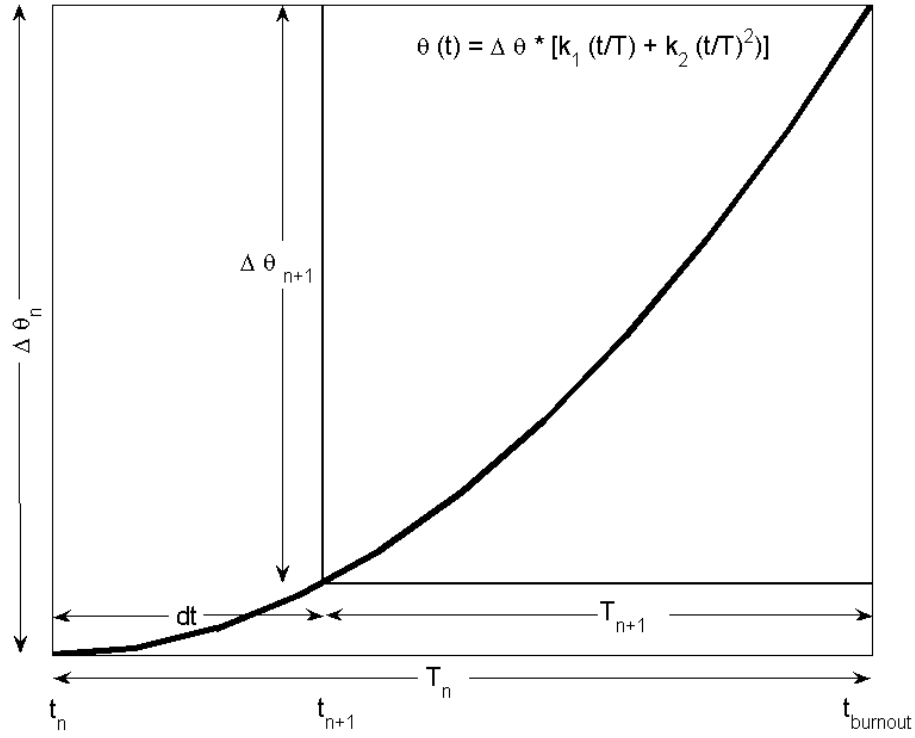


Figure 7-3: Understanding the \mathbf{k} Update Process

7.1.3 Updating the K Vector

It turns out that because of how the \mathbf{k} is defined, it does not stay constant. Suppose a function $\theta(t)$ is defined by a vector \mathbf{k} in the domain from t_{current} to t_{burnout} and has a range from θ_{current} to θ_{final} . A certain amount of time dt passes from guidance step n to the next guidance step $n + 1$. In order to stay on the path defined by \mathbf{k} at guidance step n , the value of \mathbf{k} must be changed. Figure 7-3 should assist in understanding this process.

Looking at Figure 7-3, it is clear that the function defined from t_n to t_{burnout} is different from the function defined from t_{n+1} to t_{burnout} . For instance, the slope at t_n is different than that at t_{n+1} . At each new guidance step, \mathbf{k} must be updated.

$$\delta x_n = 1 - k_1 \left(\frac{dt}{T_n} \right) - k_2 \left(\frac{dt}{T_n} \right)^2 \quad (7.8)$$

$$k_1(t_{n+1}) = \frac{1}{\delta x_n} \left(k_1 \left(\frac{T_n - dt}{T_n} \right) + 2k_2 \left(\frac{T_n - dt}{T_n} \right) \left(\frac{T_n - dt}{T_n} \right) \right) \quad (7.9)$$

$$k_2(t_{n+1}) = \frac{1}{\delta x_n} \left(k_2 \left(\frac{T_n - dt}{T_n} \right)^2 \right) \quad (7.10)$$

$$= 1 - k_1(t_{n+1}) \quad (7.11)$$

Note that δx_n is simply a fraction corresponding to the fraction of θ that has been traveled in dt . Equations 7.8, 7.9, and 7.10 can be used to update the values for k_1 and k_2 . These relations were determined using the method of substitution.

7.1.4 Perturbations on the Time Line

The final control input that is implemented in this thesis is a perturbation on the original time line. Recall in Chapter 6 that a constant interstage time $\Delta t_{interstage} = 10$ sec was assumed. Prior to the actual second stage ignition, that interstage time can be varied if doing so improved the performance. The control variable δt_{S2I} is therefore a perturbation on the t_{S2I} that can be adjusted prior to the actual ignition.

7.2 Updating the Reference Guidance Solution

The reference guidance solution introduced in the previous chapter still resulted in appreciable errors. The first use of the method of linear perturbations will be to update the guidance solution so that the predicted error is driven down to zero. This iterative algorithm will be run prior to first stage ignition to refine the attitude profile during the burn. At the start of this algorithm, $k_2 = 0$ and $\delta t_{S2I} = 0$.

7.2.1 Control Input Vector

When using the method of linear perturbations to update the reference trajectory, every control variable is available since the original reference assumptions have been dropped and the spacecraft can still reach any $\hat{\mathbf{i}}_{initial}$. Equation 7.12 includes all of the perturbations on the reference guidance solution \mathbf{c} .

$$\Delta \mathbf{c} = \begin{bmatrix} \delta\theta_i \\ \delta\psi_i \\ \delta\theta_f \\ \delta\psi_f \\ \delta t_{S2I} \\ \delta k_2 \end{bmatrix} \quad (7.12)$$

Since there are six control variables, that means that the nonlinear simulation will be run seven times for every iteration that the reference trajectory is updated, once for $\Delta \mathbf{c} = 0$ and six times where $\Delta \mathbf{c} = \Delta c_n$ where Δc_n is a small perturbation on each of the six control variables. The result $\mathbf{r}_f(\mathbf{c} + \Delta c_n)$ of each nonlinear simulation is used to estimate $\partial \mathbf{r} / \partial c_n$. Finally, since there are $n = 6$ control variables and $m = 3$ components of error, Equation 3.20 is used to find a combination of control inputs $\Delta \mathbf{c}_{cmd}$ that will drive the expected error down to zero. *The method of linear perturbations is only being used right here to update the reference guidance solution prior to first stage ignition.*

In reality, perturbations in the control variables are only approximately linear so when the nonlinear simulation is run to determine $\Delta \mathbf{c}_{cmd}$, there will still be error after applying the modifications to the control variables. For this reason, the method of linear perturbations should be implemented as an iterative method where the reference guidance solution \mathbf{c}_p improves at each step. With a sufficient number of iterations, the expected error \mathbf{e}_p should converge to zero.

7.2.2 The Reference Update Algorithm

At this point, the series of equations that will be used to update the reference trajectory have already been stated. To ensure clarity, the implementation of the method of linear perturbations to improve the reference trajectory discussed above has been repeated below.

1. Inputs: ignition state ($\mathbf{r}_{ignition}$, $\mathbf{v}_{ignition}$, reference guidance solution $\hat{\mathbf{i}}_{initial}$) and \mathbf{c} ($\hat{\mathbf{i}}_{final}$, $t_{stage\ 2\ ignition} = 0$, $k_2 = 0$).
2. Run nonlinear simulation with $\Delta\mathbf{c} = 0$ to determine final position $\mathbf{r}_f(\mathbf{c}_p)$.
3. Run nonlinear simulation with $\Delta\mathbf{c} = \delta\theta_i$ to determine final position $\mathbf{r}_f(\mathbf{c}_p + \delta\theta_i)$.
4. Run nonlinear simulation with $\Delta\mathbf{c} = \delta\psi_i$ to determine final position $\mathbf{r}_f(\mathbf{c}_p + \delta\psi_i)$.
5. Run nonlinear simulation with $\Delta\mathbf{c} = \delta\theta_f$ to determine final position $\mathbf{r}_f(\mathbf{c}_p + \delta\theta_f)$.
6. Run nonlinear simulation with $\Delta\mathbf{c} = \delta\psi_f$ to determine final position $\mathbf{r}_f(\mathbf{c}_p + \delta\psi_f)$.
7. Run nonlinear simulation with $\Delta\mathbf{c} = \delta k_2$ to determine final position $\mathbf{r}_f(\mathbf{c}_p + \delta k_2)$.
8. Run nonlinear simulation with $\Delta\mathbf{c} = \delta t_{S2I}$ to determine final position $\mathbf{r}_f(\mathbf{c}_p + \delta t_{S2I})$.
9. Find $\mathbf{D}_p = \left[\frac{\mathbf{r}_f(\mathbf{c}_p + \delta\theta_i) - \mathbf{r}_f(\mathbf{c}_p)}{\delta\theta_i} \dots \frac{\mathbf{r}_f(\mathbf{c}_p + \delta t_{S2I}) - \mathbf{r}_f(\mathbf{c}_p)}{\delta t_{S2I}} \right]$
10. Use method of linear perturbations to find the optimal changes to the set of guidance commands $\Delta\mathbf{c}$ (Equation 3.20)
11. Update the planned guidance solution $\mathbf{c} = \mathbf{c} + \Delta\mathbf{c}$.
12. Repeat steps 2 to 12 until $\mathbf{r}_f(\mathbf{c}_p) = \mathbf{r}_{rendezvous}$
13. Outputs: updated guidance solution \mathbf{c} and $\hat{\mathbf{i}}_{initial}$.

7.3 Closed Loop Guidance

At this point, there is a reference guidance solution with very little expected error, based on the model of the vehicle dynamics. During the actual burn, various uncertainties will enter into the problem. The actual state vector will likely begin to deviate from the state vector predicted by the reference trajectory. Therefore, the expected error will begin to grow. Depending on the mission, $\mathbf{r}_{rendezvous}$ may change during the course of the burn. The purpose of the closed loop guidance algorithm is to respond to these uncertainties when there is still adequate time and control authority with which to do so.

7.3.1 Control Input Vector

Since the first stage burn has already started, the $\hat{\mathbf{i}}_{initial}$ is no longer something that can be controlled. During the first stage burn, both k_2 and t_{S2I} can be modified and therefore the perturbation control vector is given by Equation 7.13. During the second stage burn, t_{S2I} has already occurred, so there are only three control variables remaining. The control variable vector is given in Equation 7.14.

$$\Delta \mathbf{c}_{first\ stage} = \begin{bmatrix} \delta\theta_f \\ \delta\psi_f \\ \delta k_2 \\ \delta t_{S2I} \end{bmatrix} \quad (7.13)$$

$$\Delta \mathbf{c}_{second\ stage} = \begin{bmatrix} \delta\theta_f \\ \delta\psi_f \\ \delta k_2 \end{bmatrix} \quad (7.14)$$

7.3.2 Closed Loop Guidance Algorithm

The following algorithm is the complete listing of steps in the guidance routine once the initial pointing direction can no longer be controlled (just prior to ignition) and before

second stage burnout.

1. Inputs: current state $(\mathbf{r}, \mathbf{v}, \hat{\mathbf{i}}, t)$, planned guidance solution \mathbf{c} ($\hat{\mathbf{i}}_{final}$, $t_{stage\ 2\ ignition}$, k_2).
2. Run nonlinear simulation with $\Delta\mathbf{c} = 0$ to determine final position.
3. Run nonlinear simulation with $\Delta\mathbf{c} = \delta\theta_f$ to determine final position $\mathbf{r}_f(\mathbf{c}_p + \delta\theta_f)$.
4. Run nonlinear simulation with $\Delta\mathbf{c} = \delta\psi_f$ to determine final position $\mathbf{r}_f(\mathbf{c}_p + \delta\psi_f)$.
5. Run nonlinear simulation with $\Delta\mathbf{c} = \delta k_2$ to determine final position $\mathbf{r}_f(\mathbf{c}_p + \delta k_2)$.
6. Run nonlinear simulation with $\Delta\mathbf{c} = \delta t_{S2I}$ to determine final position $\mathbf{r}_f(\mathbf{c}_p + \delta t_{S2I})$.
7. Find $\mathbf{D}_p = \left[\frac{\mathbf{r}_f(\mathbf{c}_p + \delta\theta_f) - \mathbf{r}_f(\mathbf{c}_p)}{\delta\theta_f} \dots \frac{\mathbf{r}_f(\mathbf{c}_p + \delta t_{S2I}) - \mathbf{r}_f(\mathbf{c}_p)}{\delta t_{S2I}} \right]$
8. Use method of linear perturbations to find the optimal changes to the set of guidance commands $\Delta\mathbf{c}$ (Equation 3.20)
9. Update the planned guidance solution $\mathbf{c} = \mathbf{c} + \Delta\mathbf{c}$.
10. Outputs: updated guidance solution \mathbf{c} and $\hat{\mathbf{i}}_{initial}$.

This chapter has now spelled out the guidance solution control inputs and the guidance algorithm. The next chapter contains results when these methods are implemented in computer simulation.

Chapter 8

Results

This chapter presents results from a closed loop simulation implementing the methods described in this thesis. These are in addition to the results contained in Chapter 5 that discuss the results of the TBCS optimization in greater depth. This simulation uses the TBCS optimized ignition point and rendezvous point given in Chapter 5. Then a reference guidance solution is calculated using the methods in Chapter 6. Finally, the method of linear perturbations on a reference trajectory from Chapter 7 is implemented. The results include both numerical accuracy and visual analysis of the resulting trajectories. There are three things that these results should and do demonstrate:

- An improvement in the accuracy of the new methods compared to the Closed Loop Lambert GEM, when both assume perfect navigation and control.
- The effectiveness of the new method in causing first stage re-entry.
- A similarity between the final closed-loop trajectories and the optimized TBCS trajectories that assume instantaneous burns. Since TBCS runs optimization on the parameters of hypothetical transfer orbits, it is important to confirm that the close loop trajectories are similar. This will validate TBCS.

Since this is not a full dynamic simulation because navigation and control are assumed to be perfect, the accuracy results contained in this section only indicate the relative performance of guidance algorithms and not the performance of any particular system

Simulation Parameters	Closed Loop Lambert GEM	New Method Reference GEM-CR	New Method Closed Loop GEM-CR
Guidance Update Rate	10 hz	n/a	1 hz
Navigation	perfect	perfect	perfect
Control	rate limited	rate limited	rate limited
Uncertainties	none	none	none

Table 8.1: Comparison of Simulation Parameters

Results	Closed Loop Lambert GEM	New Method Reference GEM-CR	New Method Closed Loop GEM-CR
Scen 1 Opt Trans	33.806 km	5.580 km	0.350 km
Scen 2 Opt Trans	38.786 km	4.779 km	0.623 km
Scen 3 Opt Trans	13.771 km	29.421 km	1.033 km

Table 8.2: Comparison of Accuracy for Various Scenarios

to meet mission requirements. They do not necessarily correspond to the accuracy of an actual system. Rather, the results show improvement over closed-loop Lambert GEM and indicate the potential for the new algorithm to be implemented on a space mission.

8.1 Performance of the Closed Loop Guidance Algorithm

The capability of the algorithm to get the spacecraft to the rendezvous point with a great deal of accuracy is an important consideration. Table 8.1 lists the various parameters for closed loop Lambert GEM, the GEM-CR reference solution, and finally the GEM-CR reference solution with the closed loop method of linear perturbations employed on the GEM-CR reference solution.

Table 8.2 lists the relative performance of the three different scenarios. Recall that in scenario 1 the trajectories were coplanar in opposite directions, in scenario 2 the trajectories were coplanar in the same direction, and in scenario 3 the trajectories were 90° out of plane. The error is defined as the magnitude difference in position between the rendezvous point $\mathbf{r}_{rendezvous}$ and the position of the spacecraft at $t_{rendezvous}$ and not the “closest approach.”

	First Stage Reentry t after $t_{ignition}$	Second Stage Reentry t after $t_{ignition}$
Scen 1 Opt Trans	70 min	236 min
Scen 2 Opt Trans	77 min	249 min
Scen 3 Opt Trans	28 min	90 min

Table 8.3: Comparison of Re-entry Times for Various Scenarios

For Scenario 1, closed loop Lambert-GEM results in 33.806 km of error even with perfect control and navigation and a more frequent guidance update rate. It is clear that even simply following the reference solution (given in the middle column of Figure 8.2) would offer an improvement to closed-loop Lambert GEM. Once the loop is closed using the method of linear perturbations, the accuracy is very high. An error of 0.350 km is small considering the extremely high velocities involved at rendezvous, around 7 km/sec. The errors from the new method, around one kilometer or less, are essentially zero and largely the result of the guidance update rate and numerical accuracies in the simulation.

The next step is to determine if the first stages were put on a path to atmospheric reentry. Table 8.3 lists the amount of time after $t_{ignition}$ before the first and second stages reenter the earth's atmosphere (in all cases, the trajectory intersects the earth's surface). The reference guidance solution accomplishes its objective of first stage reentry in each of the three scenarios. TBCS, which was originally responsible for ensuring second stage reentry after the loop is closed, also accomplishes its objective for the three scenarios.

8.1.1 Scenario 1

At this point, the actual trajectories will be inspected to confirm that they meet expectations. Figure 8-1 shows a global view of the scenario 1 trajectories. As a result of the initial conditions, all of the trajectories lie in the same plane. The Keplerian trajectory is shown in red. The spacecraft's parking orbit is shown in blue. The TBCS solution corresponding to a $\Delta \mathbf{v}_{instantaneous}$ is shown in black. The spacecraft's position during the burn is shown as the thick red line. The spacecraft's position during the coast phase and the continued trajectory after the rendezvous are shown in green. The continued trajectory is shown in light blue.

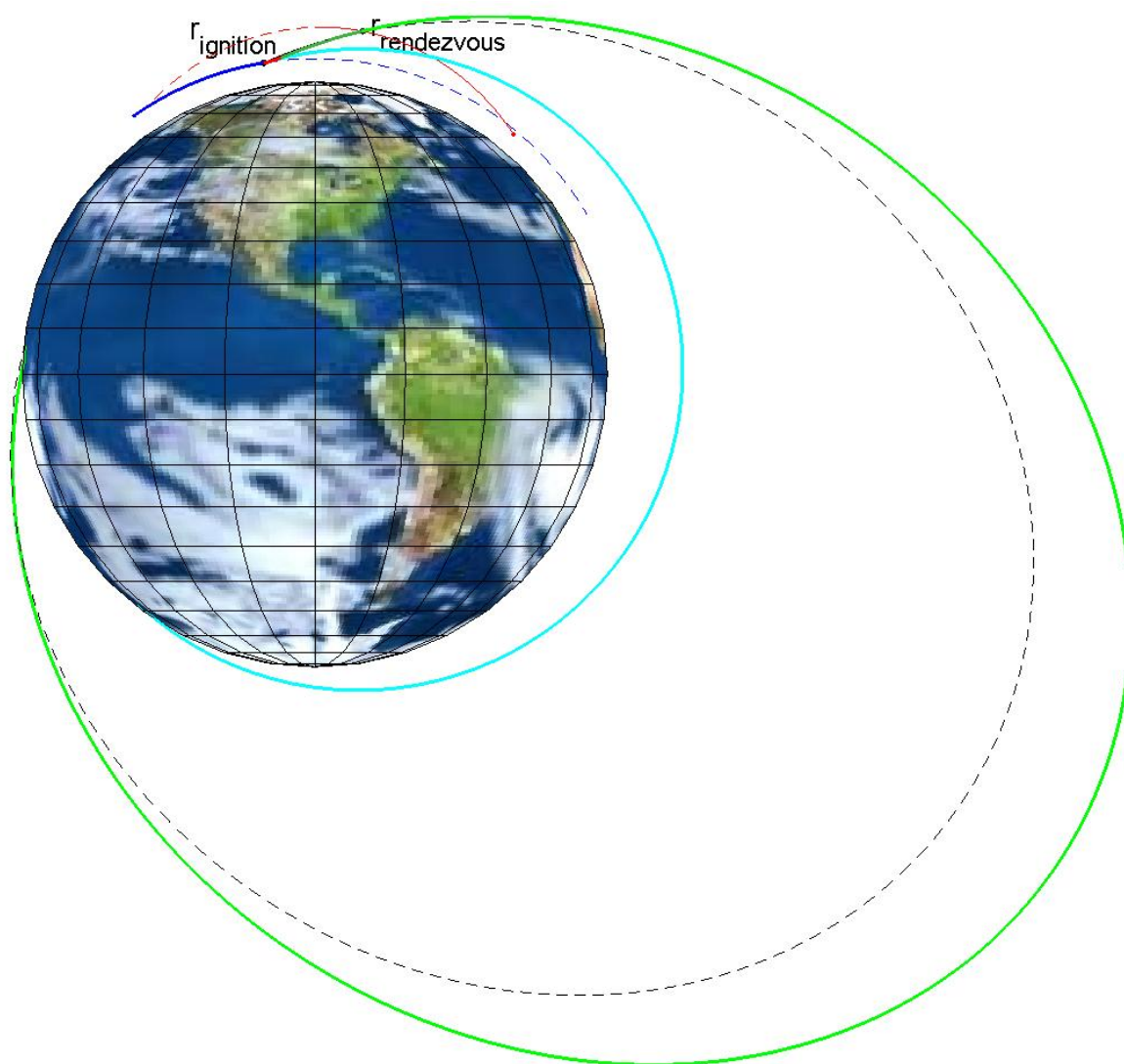


Figure 8-1: Global View of the Closed Loop Simulation Trajectories, Scenario 1

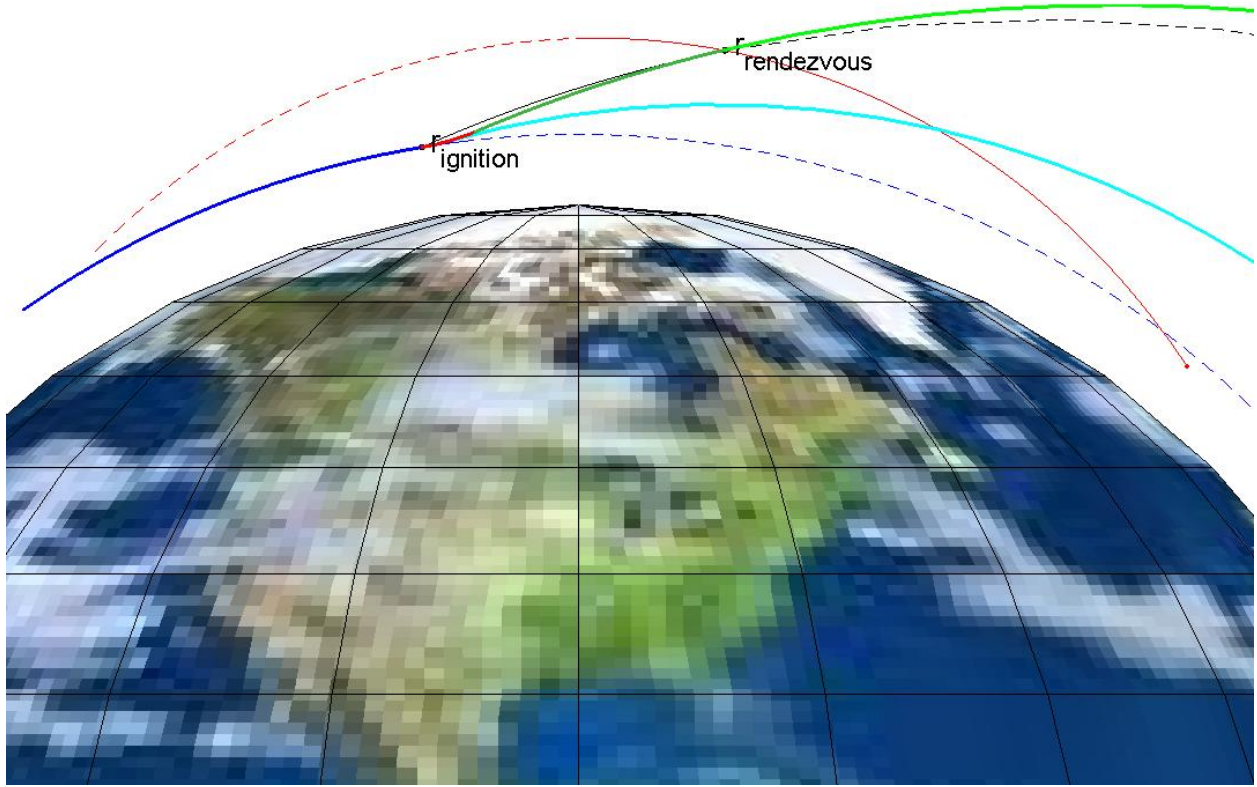


Figure 8-2: View of the Closed Loop Simulation Trajectories, Scenario 1

It is clear that both the second stage/payload and the first stage re-enter the atmosphere. The second stage follows the trajectory planned by the TBCS optimization well, and re-enters the atmosphere near the point it was predicted. The first stage also clearly follows a re-entry trajectory and de-orbits approximately two-thirds of an orbit later. Figure 8-1 demonstrates two things: first, that the closed loop trajectories are very close to those predicted by TBCS, and second, that the method of the gradient of perigee does lead to the de-orbit of the first stage.

Figure 8-2 shows a close-in view of the relative positions of the transfer, the original parking orbit, and the Keplerian trajectory.

Figure 8-3 is a view of only the transfer trajectory. This shows clearly the difference in trajectories between the $\Delta \mathbf{v}_{\text{instantaneous}}$ Lambert solution (in black) and the actual path that the satellite follows. There is a slight delay in acquiring the trajectory but by the

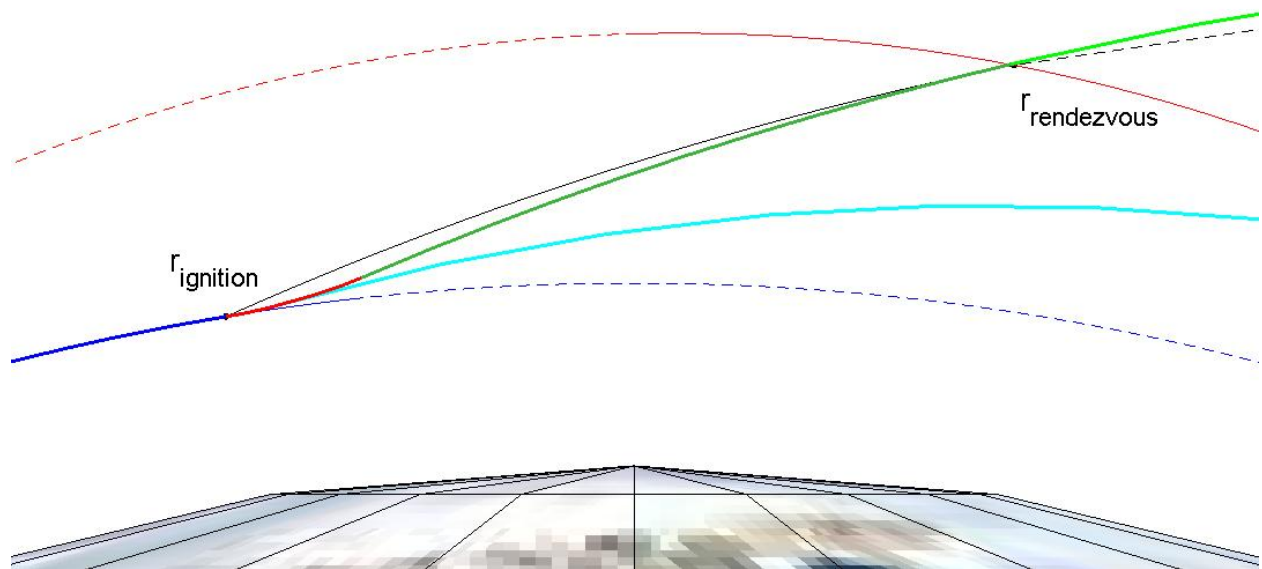


Figure 8-3: Close-In View of the Closed Loop Simulation Transfer, Scenario 1

end of the burn the spacecraft is traveling nearly parallel to the Lambert solution and crosses it when it reaches the rendezvous point.

Chapter 6 explains the technique in which the RPV frame is placed relative to the ECI frame. Recall that the frame is rotated such that first stage separation occurs at a place in three-dimensional ΔV space opposite of the gradient of perigee vector. Suppose that the first stage separation occurred in the direction of the gradient of perigee vector $\nabla r_p(\Delta \mathbf{v}_{MPFSS}^{RTN})$. If the analysis of Chapter 4 and methods of Chapter 6 are correct, the behavior of the first stage after separation would be different since it would have acquired a substantially different velocity by the time of separation. This would, in essence, maximize the perigee. Figure 8-4 depicts a closed-loop maneuver where the y-axis of the RPV plane is defined in the opposite direction of that which would minimize first stage perigee. The accuracy of the new burn is 0.716 km, essentially the same as that shown in Table 8.2 for Scenario 1, but it is clear that the first stage does not de-orbit within one revolution. This demonstrates the effectiveness of the new method of defining the plane of maneuver to cause first stage reentry. *The new method has caused the first stage to reenter with no reduction in accuracy, where another implementation may have resulted in the first stage remaining in orbit.*

8.1.2 Scenario 3

It is also important to validate the algorithm with results for Scenario 3, since the three dimensional trajectories involved make calculating the plane of maneuver a more complex problem. The colors denote the same trajectories as in the previous figures. Figure 8-5 shows a side-view of the transfer trajectory and the continued paths of both the first stage and second stage. It is clear that both the first and second stages eventually lead to reentry.

Figure 8-6 depicts the same closed-loop solution from a polar view, which clearly delineates the relative orientation of the different orbital planes for the trajectories. Figure 8-3 shows the transfer from “behind” the spacecraft starting position. This figure shows the relative altitudes involved with the problem.

Together, Figures 8-5, 8-6, and 8-7 have demonstrated the effectiveness of the new

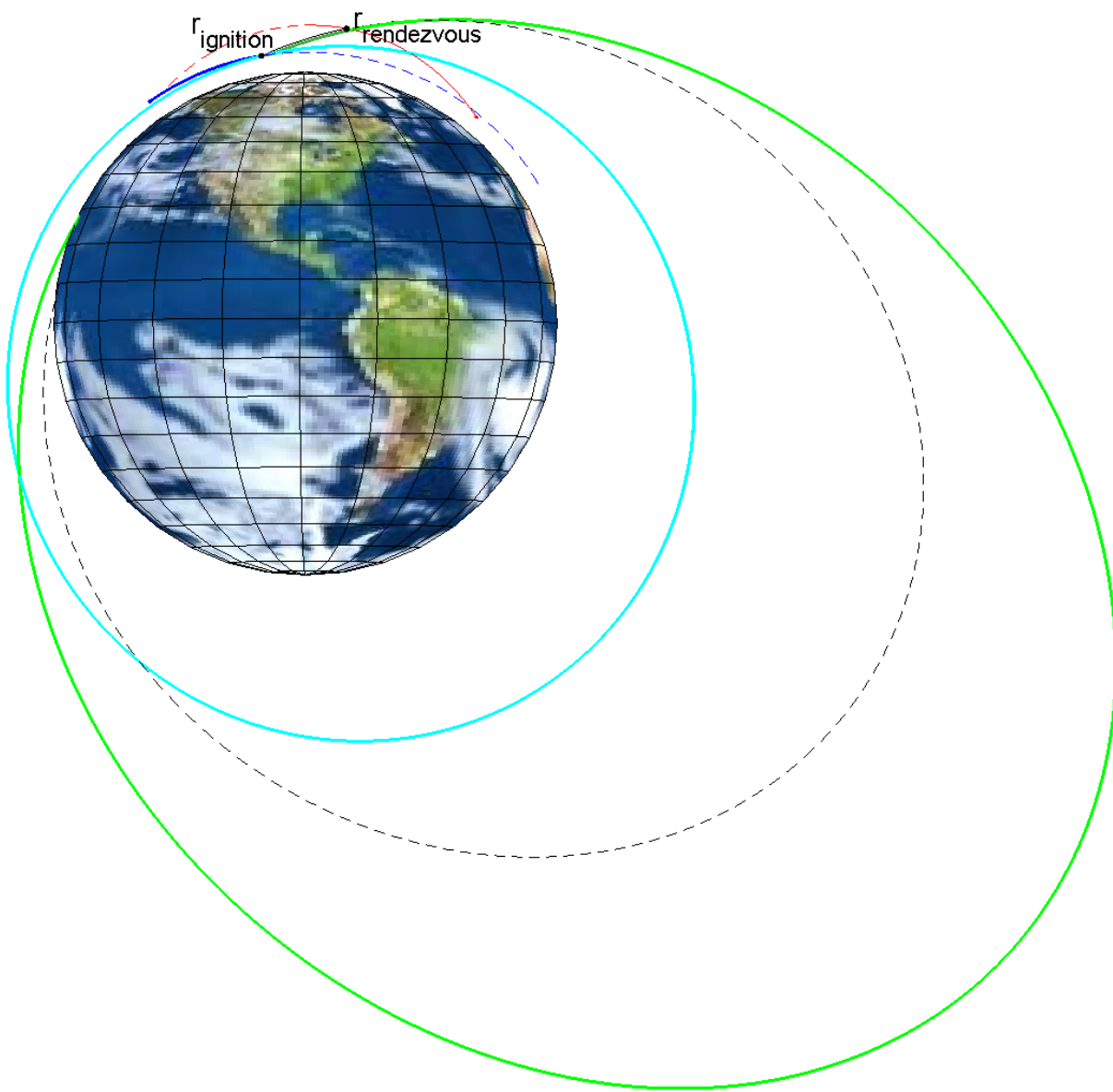


Figure 8-4: Alternate Plane of Maneuver, Scenario 1

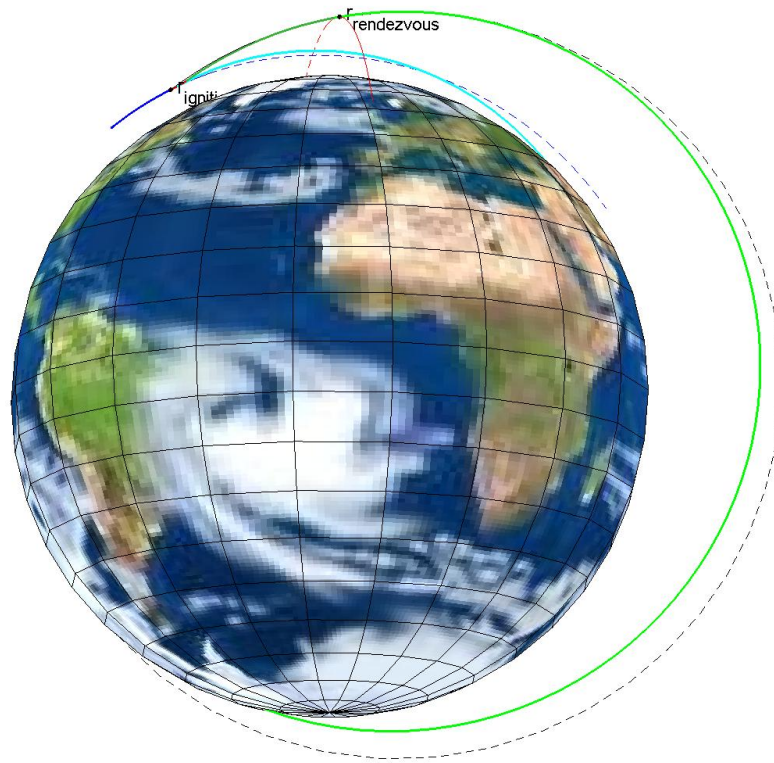


Figure 8-5: View of the Closed Loop Simulation Trajectories, Scenario 3

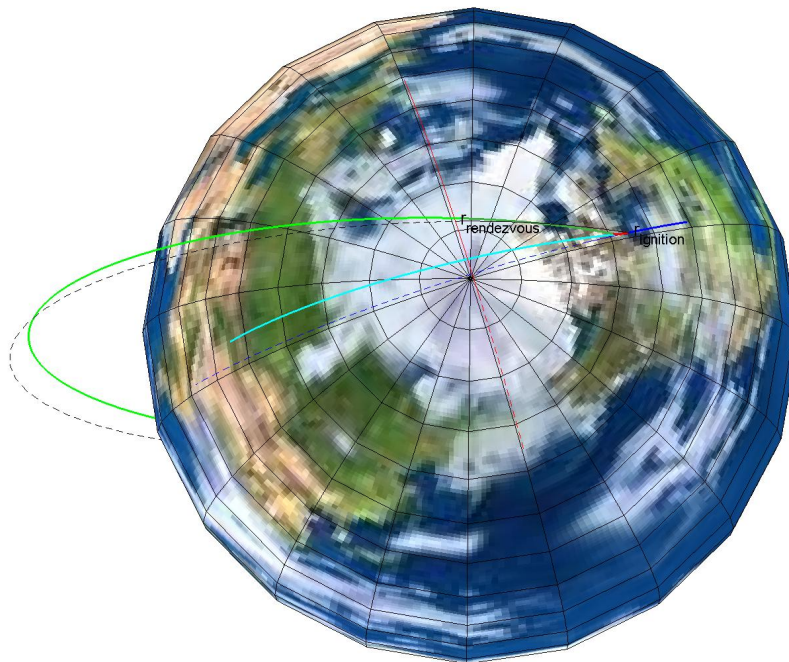


Figure 8-6: View of the Closed Loop Simulation Trajectories, Scenario 3

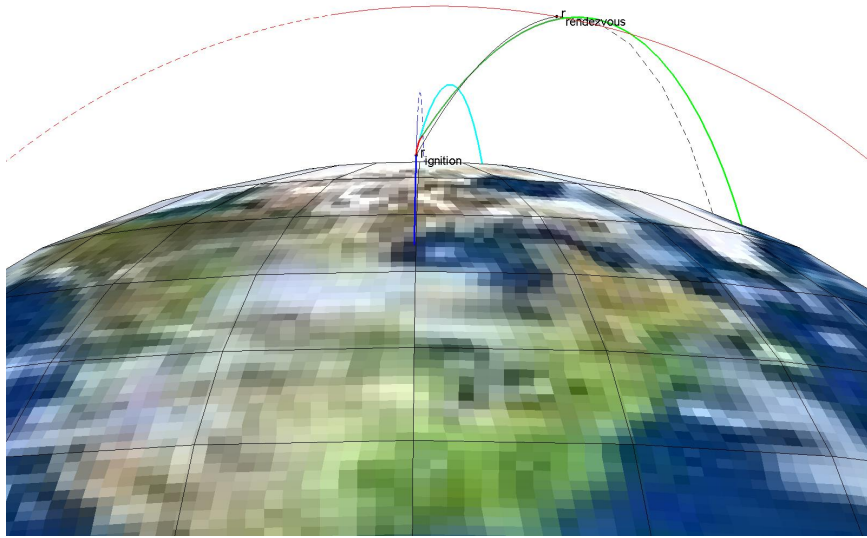


Figure 8-7: View of the Closed Loop Simulation Trajectories, Scenario 3

method in solving a complex three dimensional orbit transfer problem. The series of attitude commands implemented have enabled high accuracy at $t_{rendezvous}$ while ensuring rapid de-orbit of the first stage.

8.2 Recommended Follow-on Analysis

There is a tremendous deal of analysis of the accuracy and behavior of these algorithms that is yet to be accomplished. Because of time constraints, this thesis was unable to answer all the questions about this algorithm that may be asked by GN&C engineers before it is implemented on a spacecraft. The purpose of the thesis is to demonstrate the basic effectiveness of the new method, but answers to questions relating to the precisely quantified robustness to changes in the rendezvous position, large uncertainties introduced in the dynamics, and other factors are left to engineers who would approach the problem with more specific mission requirements and hardware design in mind.

Chapter 9

Conclusion

The objective of this thesis was to present a framework with which to solve a certain class of spacecraft guidance problems. These problems include a mission to rendezvous along a Keplerian trajectory while under the constraints of a fixed ΔV and requirement to rapidly de-orbit. Given the initial conditions for two trajectories, the *Trajectory Boundary Condition Selection* algorithm automatically determines a spacecraft ignition point and rendezvous point. These two points define a favorable transfer orbit with a cost function that captures the preferences of mission managers. Given this transfer orbit, a reference guidance solution including a plane of maneuver is calculated. The reference trajectory arrives near the rendezvous point at rendezvous time and results in rapid de-orbit of both the first and second stages. Finally, the method of linear perturbations is used to close the loop using slight modifications to the guidance solution control inputs for a further improvement in accuracy.

Hypothetical spacecraft characteristics and an example mission were provided as a starting point. For each step along the way, appropriate analysis and results were included. The purpose was not to determine specific accuracy results, but rather demonstrate the general effectiveness of a new guidance strategy. The new guidance method shows an improvement in accuracy of two orders of magnitude over the Closed-Loop Lambert GEM method it was designed to replace.

9.1 Key Developments, Observations and Results

The hope is that the framework developed here could be implemented by tailoring the specific strategies to whatever the mission requirements dictate. The following are the most important new developments, observations, and results detailed in this thesis.

9.1.1 Analysis of Relationship between Perigee and ΔV

Chapter 4 derived and explained a substantial amount about the relationship between perigee and ΔV and developed an understanding of the impact imparting velocity in specific directions and at specific magnitudes had on the reentry characteristics of a transfer orbit. Applied to this mission, it creates an awareness of “restricted areas” in velocity-space which cause the spacecraft to remain in orbit. In particular, the algorithm for finding gradient of perigee and its application to automatic first stage reentry in Chapter 6 is a entirely new and promising approach.

9.1.2 Impact of Initial Conditions on Possible Transfers

Chapter 5 uses three different scenarios to illustrate how initial conditions impact the possible transfers and their different orbit parameters. It concluded that certain parameters were largely dependent on the initial conditions while a trajectory selection and guidance algorithm could control other parameters. Specifically, it was discovered that the re-entry characteristics could be determined by trajectory selection, since a given set of initial conditions typically had a wide range of perigee and apogee altitudes. On the contrary, the relative velocity at rendezvous was not something that a great deal of control could be exercised over but rather it is dictated by the relative orientation of the initial conditions for the spacecraft and Keplerian trajectory. Rendezvous time depended both on the initial conditions and the transfer orbit selected.

9.1.3 Framework for Selecting an Optimal Transfer

Chapter 5 introduced Trajectory Boundary Condition Optimization. This is a framework that can be used to choose one particular transfer orbit solution from an infinite number of different possibilities. A sample cost function was used to show how engineers might capture the preferences of human decision makers over a number of parameters that relate to re-entry properties and likelihood of mission success.

9.1.4 A New Reference Guidance Solution Technique

Chapter 6 introduces a new technique that involves calculating a “plane of maneuver” in which the ΔV is imparted. Using two alternate baseline definitions of general energy management (GEM) maneuvers, a straightforward algorithm was developed that found a GEM solution based on the transfer orbit geometry by using lookup tables. The GEM solution is then rotated into the earth-centered inertial frame using relationships derived in Chapter 4. This GEM plane of maneuver defines an attitude profile during a burn such that the first stage perigee is automatically minimized, making first stage re-entry highly likely at no cost to flexibility or accuracy. Scenario results from Chapter 8 demonstrate that this new gradient of perigee technique was successful in causing rapid atmospheric reentry for the first stage.

9.1.5 Substantial Improvements in Baseline Accuracy

By using the reference solution with the method of linear perturbations, results indicate a one to two order of magnitude reduction in error from the original Closed-Loop Lambert GEM technique. While the accuracy needs to be re-evaluated with a full navigation and attitude control system responding to dynamic uncertainties, these results indicate that the new method is clearly superior to closed-loop Lambert GEM.

9.2 Recommendations for Future Work

Since many areas closely related to this work remain unexplored, there are ample opportunities to further investigate several of the topics contained in this thesis. The following areas are a few of the best choices for continued research.

9.2.1 Examining the Effects of Uncertainties on Accuracy

The next step in this research would be to model a theoretical navigation and control system so that monte carlo style sensitivity analysis can be done. More specifics about the hardware would need to be assumed. The new guidance method developed in this thesis should be tested against uncertainties. Theoretically, GEM employed with the method of linear perturbations should have strong robustness to uncertainties in dynamics and changes in the rendezvous point, particularly early on during the burn. This should be verified with continued use of six degree of freedom simulations. The problem also posed unique challenges. A fixed ΔV (typically solid rocket) propulsion system with no engine cut-off mechanism can introduce a great deal of error if the actual thrust impulse is not accurately known. This is just one major source of accuracy errors and exactly how significant the error is should be a focus of future research.

9.2.2 Relating ΔV to Re-entry Time

Chapter 4 develops the analytic relationships between perigee and $\Delta \mathbf{v}$. The results can be used to carefully control perigee altitude during the maneuver. However, if a real mission had a reentry requirement that was a matter of years instead of a matter of hours it might be better to relate time until reentry directly to $\Delta \mathbf{v}$. One promising avenue would be an attempt to develop a function that would basically take perigee altitude, apogee altitude, and ballistic coefficient and return the mean and variance for expected reentry time. This might be accomplished by using the calculus of variations and perturbation methods upon the orbital elements of e and a .

9.2.3 Refining the TBCS Optimization Technique

As currently employed, Trajectory Boundary Condition Selection is able to calculate a relatively “favorable” transfer trajectory. While it may suit the purposes of this mission, it is not necessarily “optimal,” and the technique itself is not very elegant. While the current implementation looks to be sufficient, there are probably better methods. A related problem would be to do a more thorough job of defining a cost function, which is very important because this defines which trajectories are “better” than others.

[This page intentionally left blank.]

Appendix A

Properties of the Example Spacecraft

In order to give the reader an intuitive feel for the problem, a hypothetical baseline vehicle has been assumed. A two-stage vehicle capable of a 3.0 km/sec ΔV would have a mass as small as 100 kg. Using nothing but the ideal rocket equation, Table A.1 lists the applicable values for mass, specific impulse, and ΔV .

Figure A-1 shows plots of mass, thrust, and acceleration versus time for the hypothetical vehicle. Figure A-1 shows a constant interstage time of 10 sec, but this may be varied according to the methods shown in Chapter 7.

Resulting from the how the burn was simulated, the figures shown in this paper are directly transferable to a vehicle with one or more stages, any particular burn, as long as ΔV capability is similar. Parking orbit altitude here is assumed to be 500 km.

	Stage 1	Stage 2	Payload
Perigee Wet Mass (kg)	40	40	20
Dry Mass (kg)	10	10	n/a
I_{sp} (sec)	300	300	n/a
ΔV (km/sec)	1.0	2.0	n/a

Table A.1: Example Spacecraft Characteristics

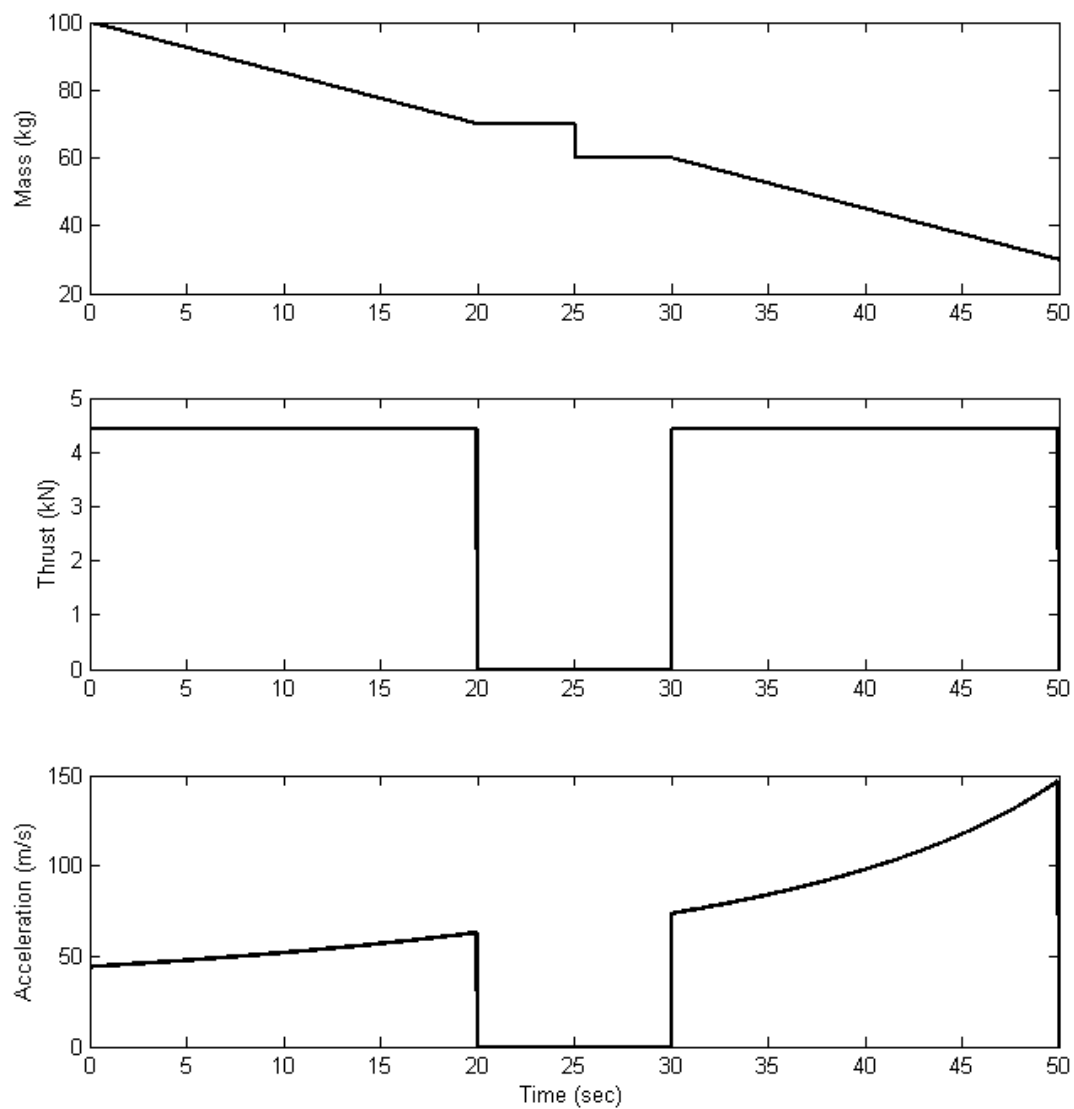


Figure A-1: Mass, Thrust, and Acceleration for Example Spacecraft

Appendix B

Details of the Numerical Examples

B.1 TBCS

This section includes the initial conditions and other important information for the Trajectory Boundary Condition Selection scenarios evaluated in Chapter 5.

B.1.1 TBCS Initial Conditions

All Vectors are given in the ECI Frame. The initial conditions for the Keplerian trajectory are identical in all three scenarios. The maximum time allowed for rendezvous from the start of the epoch is 28 minutes (1680 seconds).

$$\begin{aligned} \text{Keplerian } \mathbf{r}_0 &= \begin{bmatrix} -4329505.5 \\ 0.0 \\ 5229774.6 \end{bmatrix} \text{ m} \\ \text{Keplerian } \mathbf{v}_0 &= \begin{bmatrix} 3720.5 \\ 0.0 \\ 5646.0 \end{bmatrix} \text{ m/sec} \end{aligned}$$

TBCS Scenario 1

$$\begin{aligned} \text{Spacecraft } \mathbf{r}_0 &= \begin{bmatrix} 3945137.3 \\ -1.0 \\ 5634240.0 \end{bmatrix} \text{ m} \\ \text{Spacecraft } \mathbf{v}_0 &= \begin{bmatrix} -6235.9 \\ 0.0 \\ 4366.4 \end{bmatrix} \text{ m/sec} \end{aligned}$$

TBCS Scenario 2

$$\begin{aligned} \text{Spacecraft } \mathbf{r}_0 &= \begin{bmatrix} -5268958.6 \\ 1.0 \\ 4421181.2 \end{bmatrix} \text{ m} \\ \text{Spacecraft } \mathbf{v}_0 &= \begin{bmatrix} 4893.3 \\ -0.0 \\ 5831.6 \end{bmatrix} \text{ m/sec} \end{aligned}$$

TBCS Scenario 3

$$\begin{aligned} \text{Spacecraft } \mathbf{r}_0 &= \begin{bmatrix} 1.0 \\ 4421181.2 \\ 5268958.6 \end{bmatrix} \text{ m} \\ \text{Spacecraft } \mathbf{v}_0 &= \begin{bmatrix} -0.0 \\ -5831.6 \\ 4893.3 \end{bmatrix} \text{ m/sec} \end{aligned}$$

B.1.2 TBCS Cost Function

This cost function is simply a linear combination of three penalties applied to the transfer orbit properties h_p , ΔV , and $t_{rendezvous}$. The penalty for perigee altitude is a quadratic

penalty beginning at 200 km below the earth's surface. The penalty for the the magnitude of ΔV is a quadratic penalty centered around 2.5 km/sec. The penalty for $t_{rendezvous}$ is a linear function that penalizes later rendezvous times.

$$h_p = \text{altitude of perigee (m)}$$

$$\Delta V = \|\Delta \mathbf{v}\| \text{ (m/sec)}$$

$$t_{rendezvous} = \text{rendezvous time (sec)}$$

$$C_{perigee} = \text{cost penalty for perigee}$$

$$C_{mag} = \text{cost penalty for magnitude of } \Delta V$$

$$C_{time} = \text{cost penalty for } t_{rendezvous}$$

$$C = \text{total cost for determining fitness of trajectory for mission}$$

$$C_{perigee} = \begin{cases} 0 & \text{if } h_p \leq k_2 \\ k_1 (h_p - k_2)^2 & \text{if } h_p > k_2 \end{cases} \quad (\text{B.1})$$

$$C_{mag} = k_3 (\Delta V - k_4)^2 \quad (\text{B.2})$$

$$C_{time} = k_5 \cdot t_{rendezvous} \quad (\text{B.3})$$

$$C = C_{perigee} + C_{mag} + C_{time} \quad (\text{B.4})$$

$$k_1 = 0.0001 \quad (\text{cost penalty for perigee})$$

$$k_2 = -200\,000 \text{ m} \quad (\text{altitude at which to begin penalizing perigee})$$

$$k_3 = 0.5 \quad (\text{cost penalty for GEM } \Delta V \text{ objective})$$

$$k_4 = 2.5 \text{ km/sec} \quad (\text{objective } \Delta V \text{ for the GEM maneuver})$$

$$k_5 = 1000 \quad (\text{cost penalty for rendezvous time})$$

B.1.3 Intermediate Numbers for TBCS Scenario 1

The following intermediate calculations can be used to reach the optimized transfer properties given in Table 5.2 from the above initial conditions.

The following vectors are simply the above initial conditions propagated forward using Kepler's method of propagating the two-body equation of motion discussed in Section 2.1.4. Note that for the Scenario 1 optimized transfer, $t_{\text{ignition}} = 405$ sec, $t_{\text{rendezvous}} = 665$ sec, and the transfer time is 260 sec.

$$\text{Spacecraft } \mathbf{r}(t_{\text{ignition}}) = \begin{bmatrix} 1117833.3 \\ -0.9 \\ 6786694.1 \end{bmatrix} \text{ m}$$

$$\text{Spacecraft } \mathbf{v}(t_{\text{ignition}}) = \begin{bmatrix} -7511.4 \\ 0.0 \\ 1237.2 \end{bmatrix} \text{ m/sec}$$

$$\text{Keplerian } \mathbf{r}(t_{\text{rendezvous}}) = \begin{bmatrix} -1040406.8 \\ -0.0 \\ 7474975.9 \end{bmatrix} \text{ m}$$

$$\text{Keplerian } \mathbf{v}(t_{\text{rendezvous}}) = \begin{bmatrix} 5719.6 \\ -0.0 \\ 1103.1 \end{bmatrix} \text{ m/sec}$$

The following velocity boundary conditions for the transfer orbit are the solution to the lambert problem.

$$\begin{aligned} \text{Transfer Orbit } \mathbf{v}(t_{\text{ignition}}) &= \begin{bmatrix} -8237.2 \\ 0.0 \\ 3674.9 \end{bmatrix} \text{ m/sec} \\ \text{Transfer Orbit } \mathbf{v}(t_{\text{rendezvous}}) &= \begin{bmatrix} -8262.1 \\ 0.0 \\ 1679.8 \end{bmatrix} \text{ m/sec} \end{aligned}$$

$$\begin{aligned} \Delta \mathbf{v}^{ECI}(t_{\text{ignition}}) &= \begin{bmatrix} -725.8 \\ 0.0 \\ 2437.7 \end{bmatrix} \text{ m/sec} \\ \Delta \mathbf{v}^{RTN}(t_{\text{ignition}}) &= \begin{bmatrix} 2287.3 \\ 1112.4 \\ -0.0 \end{bmatrix} \text{ m/sec} \end{aligned}$$

$$\mathbf{T}_{ECI2RTN}(t_{\text{ignition}}) = \begin{bmatrix} 0.162520 & -0.000000 & 0.986705 \\ -0.986705 & 0.000000 & 0.162520 \\ -0.000000 & -1.000000 & -0.000000 \end{bmatrix}$$

Using Table 5.2 and Equation B.1, the optimized cost is found to be 6.6594e+005.

B.2 Reference Guidance Solution

This section includes intermediate numbers used to determine the reference guidance solution. Note that $\mathbf{T}_{RPV2ECI}$ is calculated with the \mathbf{d} from the Lambert instantaneous velocity. For all reference guidance solutions, $k_2 = 0$ and $\delta t_{S2I} = 0$.

B.2.1 Scenario 1 Intermediate Numbers

$$\text{Spacecraft } \mathbf{r}(t_{\text{ignition}}) = \begin{bmatrix} 1117833.3 \\ -0.9 \\ 6786694.1 \end{bmatrix} \text{ m}$$

$$\text{Spacecraft } \mathbf{v}(t_{\text{ignition}}) = \begin{bmatrix} -7511.4 \\ 0.0 \\ 1237.2 \end{bmatrix} \text{ m/sec}$$

$$\text{Parking Orbit } \mathbf{r}_{\text{without burn}} = \begin{bmatrix} -851510.5 \\ -0.7 \\ 6825225.2 \end{bmatrix} \text{ m}$$

$$(\text{Using } \mathbf{r}_{\text{without burn}}) \mathbf{d} = \begin{bmatrix} -188896.3 \\ 0.7 \\ 649750.7 \end{bmatrix} \text{ m}$$

$$(\text{Using Lambert}) \mathbf{d} = \begin{bmatrix} -188716.5 \\ 0.8 \\ 633800.9 \end{bmatrix} \text{ m}$$

$$\Delta \mathbf{v}_{MPFSS}^{RTN} = \begin{bmatrix} 754.8 \\ 367.1 \\ -0.0 \end{bmatrix} \text{ m/sec}$$

$$\nabla_{r_p}^{RTN}(\Delta \mathbf{v}_{MPFSS}^{RTN}) = \begin{bmatrix} 50.426 \\ -200.634 \\ -0.000 \end{bmatrix}$$

$$\text{Reference } \mathbf{T}_{RPV2ECI} = \begin{bmatrix} -0.285372 & -0.958417 & -0.000000 \\ 0.000001 & -0.000000 & -1.000000 \\ 0.958417 & -0.285372 & 0.000001 \end{bmatrix}$$

$$\text{Reference } \hat{\mathbf{i}}_{initial}^{RPV} = \begin{bmatrix} 0.770458 \\ 0.637491 \\ 0.000000 \end{bmatrix}$$

$$\text{Reference } \hat{\mathbf{i}}_{final}^{RPV} = \begin{bmatrix} 0.893470 \\ -0.449123 \\ 0.000000 \end{bmatrix}$$

$$\text{Reference } \hat{\mathbf{i}}_{initial}^{ECI} = \begin{bmatrix} -0.830849 \\ 0.000001 \\ 0.556498 \end{bmatrix}$$

$$\text{Reference } \hat{\mathbf{i}}_{final}^{ECI} = \begin{bmatrix} 0.175475 \\ 0.000001 \\ 0.984484 \end{bmatrix}$$

B.2.2 Scenario 2 Intermediate Numbers

$$\text{Spacecraft } \mathbf{r}(t_{ignition}) = \begin{bmatrix} -3110430.7 \\ 0.9 \\ 6134654.8 \end{bmatrix} \text{ m}$$

$$\text{Spacecraft } \mathbf{v}(t_{ignition}) = \begin{bmatrix} 6789.7 \\ -0.0 \\ 3442.6 \end{bmatrix} \text{ m/sec}$$

$$\text{Parking Orbit } \mathbf{r}_{\text{without burn}} = \begin{bmatrix} -1318871.6 \\ 0.8 \\ 6750507.1 \end{bmatrix} \text{ m}$$

$$(\text{Using } \mathbf{r}_{\text{without burn}}) \mathbf{d} = \begin{bmatrix} -5025.7 \\ -0.8 \\ 660891.0 \end{bmatrix} \text{ m}$$

$$(\text{Using Lambert}) \mathbf{d} = \begin{bmatrix} -336.8 \\ -0.8 \\ 647429.3 \end{bmatrix} \text{ m}$$

$$\Delta \mathbf{v}_{MPFSS}^{RTN} = \begin{bmatrix} 762.4 \\ 386.1 \\ -0.0 \end{bmatrix} \text{ m/sec}$$

$$\nabla_{r_p}^{RTN}(\Delta \mathbf{v}_{MPFSS}^{RTN}) = \begin{bmatrix} 54.415 \\ -208.059 \\ -0.000 \end{bmatrix}$$

$$\text{Reference } \mathbf{T}_{RPV2ECI} = \begin{bmatrix} -0.000520 & 1.000000 & -0.000000 \\ -0.000001 & 0.000000 & 1.000000 \\ 1.000000 & 0.000520 & 0.000001 \end{bmatrix}$$

$$\text{Reference } \hat{\mathbf{i}}_{initial}^{RPV} = \begin{bmatrix} 0.847775 \\ 0.530357 \\ 0.000000 \end{bmatrix}$$

$$\text{Reference } \hat{\mathbf{i}}_{final}^{RPV} = \begin{bmatrix} 0.928643 \\ -0.370974 \\ 0.000000 \end{bmatrix}$$

$$\text{Reference } \hat{\mathbf{i}}_{initial}^{ECI} = \begin{bmatrix} 0.529916 \\ -0.000001 \\ 0.848050 \end{bmatrix}$$

$$\text{Reference } \hat{\mathbf{i}}_{final}^{ECI} = \begin{bmatrix} -0.371457 \\ -0.000001 \\ 0.928450 \end{bmatrix}$$

B.2.3 Scenario 3 Intermediate Numbers

$$\text{Spacecraft } \mathbf{r}(t_{ignition}) = \begin{bmatrix} 1.0 \\ 3225714.4 \\ 6074828.0 \end{bmatrix} \text{ m}$$

$$\text{Spacecraft } \mathbf{v}(t_{ignition}) = \begin{bmatrix} -0.0 \\ -6723.5 \\ 3570.2 \end{bmatrix} \text{ m/sec}$$

$$\text{Parking Orbit } \mathbf{r}_{without \ burn} = \begin{bmatrix} 0.7 \\ -329363.9 \\ 6870246.6 \end{bmatrix} \text{ m}$$

$$\text{(Using } \mathbf{r}_{\text{without burn}}) \quad \mathbf{d} = \begin{bmatrix} -983400.7 \\ 329363.9 \\ 615379.0 \end{bmatrix} \quad \text{m}$$

$$\text{(Using Lambert)} \quad \mathbf{d} = \begin{bmatrix} -1025755.5 \\ 329063.5 \\ 555102.6 \end{bmatrix} \quad \text{m}$$

$$\Delta \mathbf{v}_{MPFSS}^{RTN} = \begin{bmatrix} 438.6 \\ -20.6 \\ -697.9 \end{bmatrix} \quad \text{m/sec}$$

$$\nabla r_p^{RTN}(\Delta \mathbf{v}_{MPFSS}^{RTN}) = \begin{bmatrix} 0.435 \\ 19.268 \\ -0.038 \end{bmatrix}$$

$$\text{Reference } \mathbf{T}_{RPV2ECI} = \begin{bmatrix} -0.846433 & 0.011559 & -0.532369 \\ 0.271537 & 0.869381 & -0.412850 \\ 0.458060 & -0.494008 & -0.739011 \end{bmatrix}$$

$$\text{Reference } \hat{\mathbf{i}}_{initial}^{RPV} = \begin{bmatrix} 0.507245 \\ 0.861802 \\ 0.000000 \end{bmatrix}$$

$$\text{Reference } \hat{\mathbf{i}}_{final}^{RPV} = \begin{bmatrix} 0.792164 \\ -0.610309 \\ 0.000000 \end{bmatrix}$$

$$\text{Reference } \hat{\mathbf{i}}_{initial}^{ECI} = \begin{bmatrix} -0.419387 \\ 0.886970 \\ -0.193389 \end{bmatrix}$$

$$\text{Reference } \hat{\mathbf{i}}_{final}^{ECI} = \begin{bmatrix} -0.677568 \\ -0.315489 \\ 0.664355 \end{bmatrix}$$

[This page intentionally left blank.]

Bibliography

- [1] Battin, Richard H. Astrodynamics Course Notes, Massachusetts Institute of Technology, Fall 2004.
- [2] Battin, Richard H. “An Introduction to the Mathematics and Methods of Astrodynamics,” New York, New York: American Institute of Aeronautics and Astronautics, 1987.
- [3] Freund, Robert M. Nonlinear Programming Course Notes, Massachusetts Institute of Technology, Spring 2004. Available at <http://ocw.mit.edu/OcwWeb/Sloan-School-of-Management/15-084JSpring2004/CourseHome/index.htm>
- [4] Sellers, J.J. “Understanding Space: An Introduction to Astronautics,” New York: McGraw-Hill, Inc., 1994.
- [5] Strang, Gilbert. “Introduction to Applied Mathematics,” Wellesley, MA: Wellesley-Cambridge Press, 1986.
- [6] Vallado, David A., Fundamentals of Astrodynamics and Applications, New York: McGraw-Hill, Inc., 1997.
- [7] Van Beusekom, Craig J., Piero Miotto, and Stanley Shepperd. “Guidance and Control for Highly Constrained Rendezvous”, *Proceedings of 15th American Astronautical Society/American Institute of Aeronautics and Astronautics Space Flight Mechanics Conference*, Copper Mountain, CO, January 2005.
- [8] Wertz, James R. and Wiley J. Larson. *Space Mission Analysis and Design*, El Segundo, CA: Microcosm Press, 1999.

- [9] Wertz, James R. *Spacecraft Attitude Determination and Control*, New York: Kluwer Academic Publishers, 1978.
- [10] Zarchan, Paul. *Tactical and Strategic Missile Guidance*, 3rd Edition, Vol. 176, Progress in Astronautics and Aeronautics, AIAA, 1997.